To the Graduate Council:

I am submitting herewith a dissertation written by Richard Andrew Lillie entitled "A Linear Triangle Finite Element Formulation for Multigroup Neutron Transport Analysis with Anisotropic Scattering." I recommend that it be accepted in partial fulfillment of the requirements for the degree of Doctor of Philosophy, with a major in Nuclear Engineering.

James C. Robinson

James C. Robinson, Major Professor

We have read this dissertation
and recommend its acceptance:

George Flanagan

O. L. Smith

J. E. Akin

Paul N Stevens

J. F. Vasquez

Accepted for the Council:

Hilton A. Smith

Vice Chancellor
Graduate Studies and Research

E

LD
T5
L943
Cop. 2

A LINEAR TRIANGLE FINITE ELEMENT FORMULATION FOR MULTIGROUP NEUTRON TRANSPORT ANALYSIS WITH ANISOTROPIC SCATTERING

A Dissertation

Presented for the

Doctor of Philosophy

Degree

The University of Tennessee

Richard Andrew Lillie

December 1975

1269149

ACKNOWLEDGMENTS

This work was performed in the Neutron Physics Division of Oak Ridge National Laboratory which is operated by Union Carbide Corporation for the Energy Research and Development Administration. Financial support was provided by an AEC Traineeship in Nuclear Engineering and a research assistantship from The University of Tennessee through Oak Ridge National Laboratory.

The author wishes to express his deep appreciation to the individuals who contributed to various phases of this work.

Dr. J. C. Robinson, who served as advisor and provided invaluable guidance throughout the study.

Dr. J. E. Akin of The University of Tennessee and W. C. T. Stoddard of Oak Ridge National Laboratory provided encouragement through many stimulating discussions with the author.

Mrs. Nita Rye, who typed the rough draft.

Finally, the author would like to thank his wife, Elizabeth, for her encouragement and patience during the course of this work. This dissertation is dedicated entirely to her.

ABSTRACT

The discrete ordinates method is the most powerful and generally used deterministic method to obtain approximate solutions of the Boltzmann transport equation. However, as presently formulated, it is both restricted to orthogonal geometries and susceptible to producing ray effects.

In this work, a finite element formulation, utilizing a canonical form of the transport equation, is developed to obtain both integral and pointwise solutions to neutron transport problems. To facilitate its application to nonorthogonal planar geometries, the formulation is based on the use of linear triangles. A general treatment of anisotropic scattering is included in the formulation by employing discrete ordinates like approximations. In addition, multigroup source outer iteration techniques are employed to perform group dependent calculations.

The ability of the formulation to substantially reduce ray effects and its ability to perform streaming calculations are demonstrated by analyzing a series of test problems. The anisotropic scattering and multigroup treatments used in the development of the formulation are verified by a number of one-dimensional comparisons. These comparisons also demonstrate the relative accuracy of the formulation in predicting integral parameters.

The applicability of the formulation to nonorthogonal planar geometries is demonstrated by analyzing a hexagonal type lattice. A

small high leakage reactor model is analyzed to investigate the effects of varying both the spatial mesh and order of angular quadrature. This analysis reveals that these effects are more pronounced in the present formulation than in other conventional formulations. However, the insignificance of these effects is demonstrated by analyzing a realistic reactor configuration. In addition, this final analysis illustrates the importance of incorporating anisotropic scattering into the finite element formulation.

TABLE OF CONTENTS

CHAPTER		PAGE
I.	INTRODUCTION	1
	Background	1
	Literature Review	5
	Objectives and Scope	8
II.	FORMALISM	10
	Multigroup Transport Equations	10
	Even-Odd Parity Transformation	12
	Discrete Angle Approximation	18
	Construction of Reduced Functional	26
	Finite Element Approximation	33
	Multigroup Source Approximation	39
III.	SOLUTION TECHNIQUES	43
	The System Equations	43
	Application of Boundary Constraints	52
	Modified Cholesky Algorithm	57
	Outer Iteration Scheme	62
	Numerical Implementation	68
IV.	NUMERICAL RESULTS	70
	Ray Effect Problems	70
	Streaming Problem	75
	One-Dimensional Eigenvalue Problem	80
	Two-Dimensional Eigenvalue Problems	86

CHAPTER PAGE

Nonorthogonal geometry model 87

High leakage test model 93

Representative reactor model 108

V. SUMMARY, CONCLUSIONS AND RECOMMENDATIONS 125

LIST OF REFERENCES 130

APPENDICES 135

A. THE ADJOINT EVEN-ODD PARITY EQUATIONS 136

B. VERIFICATION OF REDUCED FUNCTIONAL 140

VITA 144

LIST OF TABLES

TABLE		PAGE
I.	Comparison of Eigenvalues with Anisotropic Scattering . . .	83
II.	Comparison of Eigenvalues Using Auxillary Relationships . .	85
III.	Comparison of Two-Dimensional Eigenvalues for Hexagonal Model	91
IV.	Comparison of Two-Dimensional Eigenvalues for Modified Hexagonal Model	94
V.	Comparison of Two-Dimensional Eigenvalues with All Vacuum Boundaries	99
VI.	Comparison of Two-Dimensional Eigenvalues Assuming Quarter Core Symmetry	103
VII.	Comparison of Two-Dimensional Eigenvalues Using Different Triangle Arrangements	107
VIII.	Comparison of Eigenvalues for Two-Dimensional Modified ZPPR-4 Model	113
IX.	Comparison of Modified ZPPR-4 Model Eigenvalues Using Different Triangle Arrangements	123

LIST OF FIGURES

FIGURE		PAGE
1.	Coordinate System for Particle Scattering in Rectangular Geometry	19
2.	Representation of Vacuum Boundary Surface for a Typical Triangle	44
3.	Representation of Local and Global Node Numbering Schemes for a Typical Triangle	50
4.	Representation of Discrete Angle Ordering Schemes	58
5.	Flow Diagram for Even Parity Flux Calculation and Multigroup Scheme	65
6.	Flow Diagram for Odd Parity Flux Calculation and Outer Iteration Convergence Check	66
7.	Comparison of Right Edge (X=1.875) Scalar Flux in a Weak Scattering Material Using DOT and DAFE	72
8.	Comparison of Right Edge (X=2.875) Scalar Flux in Both a Weak and Strong Scattering Material Using DOT and DAFE	74
9.	Comparison of Right Edge (X=1.875) Scalar Flux in the Presence of a Void Using DOT and DAFE	76
10.	Comparison of Right Edge (X=1.875) Scalar Flux in the Presence of a Void Using Modified Angular Quadratures in DOT and DAFE	78
11.	Half Core Mockup of FTR-3 Loading in ZPR-9	81
12.	Triangular Mesh Description for Hexagonal Model Eigenvalue Comparison Using TRIPLET and DAFE (Test Case 1)	88

FIGURE PAGE

13. Mesh Description for Modified Hexagonal Model Eigenvalue Comparison. Rectangles Denote DOT Mesh; Triangles Denote TRIPLET and DAFE Mesh (Test Case 2) 89

14. Vacuum Boundary Refined Triangular Mesh Description for Hexagonal Model Eigenvalue Comparison Using TRIPLET and DAFE (Test Case 3) 92

15. Typical Regular Triangle Arrangement (50 Triangles) for Two-Dimensional Eigenvalue Comparison 95

16. Typical Crossed Triangle Arrangement (60 Triangles) for Two-Dimensional Eigenvalue Comparison 97

17. Comparison of Group Scalar Fluxes Near Center (Y=5.76 cm) of Eight Zone Two-Dimensional Model Using TRIPLET and DAFE with the 200 Regular Triangle Arrangement 101

18. Illustration of Changes in Unknown Coupling Due to Different Triangle Orientations 105

19. Typical Reversed Triangle Arrangement (50 Triangles) for Two-Dimensional Eigenvalue Comparison 106

20. Comparison of Group Scalar Fluxes Near Center (Y=5.76 cm) of Eight Zone Two-Dimensional Model Generated Using DAFE with Both the 200 Regular and Reversed Triangle Arrangements 109

21. Quarter Core Model of Modified Two-Dimensional X-Y Geometry Mockup of ZPPR-9 110

FIGURE PAGE

22. Three-Dimensional Plot of U-235 Reaction Rate Obtained from DOT S_4P_1 Calculation with Control Rods In 114

23. Three-Dimensional Plot of U-235 Reaction Rate Obtained from DAFE E_2P_1 (Reversed Triangles) Calculation with Control Rods Out 115

24. Three-Dimensional Plot of U-238 Reaction Rate Obtained from DAFE E_2P_1 (Regular Triangles) Calculation with Control Rods In 116

25. Three-Dimensional Plot of U-238 Reaction Rate Obtained from DOT S_2P_1 Calculation with Control Rods Out 117

26. Three-Dimensional Plot of U-238 Reaction Rate Differences Between DAFE E_2P_1 (Regular Triangles) and DOT S_2P_1 Calculations with Control Rods In 119

27. Three-Dimensional Plot of U-238 Reaction Rate Differences Between DAFE E_2P_1 (Reversed Triangles) and DOT S_2P_1 Calculations with Control Rods In 120

28. Three-Dimensional Plot of U-235 Reaction Rate Differences Between DAFE E_2P_1 (Regular Triangles) and DOT S_4P_1 Calculations with Control Rods Out 121

29. Three-Dimensional Plot of U-238 Reaction Rate Differences Between DAFE E_2P_1 (Reversed Triangles) and DAFE E_2P_1 (Regular Triangles) Calculations with Control Rods In . . 124

CHAPTER I

INTRODUCTION

Background

During the past three decades, the reactor physicist or nuclear designer has relied primarily on numerical methods employing finite difference techniques to solve neutron transport problems. Of these methods, the most powerful and generally used to obtain approximate solutions to the Boltzmann transport equation has been the discrete ordinates method. Its development and numerical implementation to solve a broad class of problems encountered in reactor core design and radiation shielding is well documented.[1,2] However, as presently formulated, the discrete ordinates method does possess at least two undesirable characteristics: it is restricted to regular (rectangular, cylindrical, or spherical) orthogonal mesh grids, and it is susceptible to producing flux distortions called "ray effects."

The orthogonal geometry restriction is most easily circumvented by sacrificing descriptive detail in calculated models. For example, although present fast reactor designs are based on hexagonal fuel, control, and blanket subassemblies, their analysis is performed utilizing R-θ cylindrical or X-Y rectangular mesh grids. These orthogonal representations are accomplished through the use of various spatial homogenizing or property averaging procedures.

Many remedies have been formulated to mitigate ray effects. Foremost among these remedies are the alteration of the discrete

ordinate equations to make them similar to the spherical harmonic equations by Lathrop,[3,4] and the analytic first collision source technique employed by Mynatt et al.[2] for certain shielding problems. However, in core physics analysis, the easiest to implement and consequently most used approach is to simply include a greater number of discrete directions. Unfortunately, this latter approach also proportionately increases the calculational cost since the increased number of directions is used over the entire solution domain, not simply those spatial regions where ray effects occurred.

In recent years, the finite element method has been demonstrated to provide a versatile alternative to traditional methods in both neutron diffusion and neutron transport computations.[5,6,7,8,9] The finite element method was originally developed for use in the area of structural analysis, and today has almost completely replaced the use of finite difference techniques.[10] Its versatility and consequently wide acceptance can be primarily attributed to its ability to handle almost any geometry, no matter how complex, and to its ability to utilize high order approximation procedures. Partly due to these advantages, Ohnishi[11] has suggested the use of several methods which divide the direction cosine spherical domain of the transport equation into curvilinear elements to eliminate ray effects. In addition, Miller et al.[9,12] have already circumvented these flux distortions by using the finite element method to directly discretize the spatial and angular variables.

The essence of the finite element method is to divide the boundary and interior of the continuum (solution domain) into a finite number of contiguous subdomains or "finite elements." Within each element the unknown function and/or its derivatives are approximated by piecewise continuous polynomials in each independent variable. The coefficients in the interpolating polynomials are determined by evaluating the unknown function and/or its derivatives at various points called "nodes" located on the boundary and throughout the interior of each element. The necessary coupling between elements is in most problems effected by requiring the nodal values to be single-valued, thus ensuring continuity across inter-element boundaries. One immediate feature of this procedure is that it eliminates the difficulty associated with needing some a priori knowledge of the solution, as in synthesis methods where the polynomials or trial functions are defined over a much greater portion of the solution domain.

Two basic formulations are used to obtain the set of linear algebraic equations which couple the unknown nodal values. The first formulation, normally referred to as the weighted residual method, consists of substituting the interpolating polynomials directly into the governing differential equation. This procedure yields a residual since the interpolating polynomials only approximate the dependent variables. Next, N linearly independent weight functions (where N represents the number of unknown nodal values) are chosen to weight the residual. Requiring the integral of the product of each weight function and the residual to be zero yields the necessary set of algebraic

equations. Among the various weight functions, the three most commonly used are the Dirac delta functions, the interpolating functions defining the approximation, and the functions obtained by differentiating the residual with respect to each of the nodal values. These three choices are generally classified as the collocation, Galerkin, and least squares approaches, respectively.[10]

The second and most widely used formulation is the variational formulation. In fact, the finite element method is considered as the Ritz method of approximating the solution of an extremum (variational) problem.[10,13] The Ritz method consists of approximating the unknown function and its derivatives in a functional "equivalent" to the governing differential equation. The set of coupling algebraic equations is obtained by requiring the first variation of the functional with respect to each nodal value to be zero.

The variational formulation and the least squares formulation guarantee that the coefficient matrix will be symmetric. Thus, in numerical computations where computer storage restrictions must be met, both formulations share this important feature. However, if an "equivalent" functional does exist for a given problem, the variational formulation is preferred since it requires a lesser degree of continuity. Because of this, the variational formulation permits a greater choice of trial functions. In addition, it automatically imposes certain boundary conditions.

Literature Review

Although the finite element method has been used extensively for several years in the area of structural analysis, it has only recently been considered an alternate method in the area of nuclear analysis. Kang and Hansen[5] have applied the finite element method to neutron slowing-down problems, static neutron diffusion problems, point reactor kinetics problems, and time-dependent neutron diffusion problems. Their two-dimensional analysis consisted of using Hermite interpolation with rectangular elements. Since the Hermite polynomials are generated by function and derivative values along the element boundaries, they have the desirable property that both function and derivative continuity can be imposed. Deppe and Hansen[14] extended the above work by allowing elements to span more than one material region. The material discontinuities resulting from this extension were directly accounted for in the element integrations.

While the procedures described in the previous two papers employed Hermite polynomials, the Lagrange polynomials have also been used as interpolating functions. These polynomials are generated using only unknown function values both along the boundary and within each element, thus they do not allow for imposition of derivative continuity conditions. However, they do lend themselves more readily to interpolation with triangular elements. Semenza et al.,[6] using linear Lagrange polynomials with triangular elements and similar bilinear polynomials with rectangular elements, have obtained approximate solutions to the "weak" or variational form of the multigroup diffusion

equations. Their results for an X-Y configuration containing a planar control rod demonstrate the ease with which many elements may be efficiently clustered near the control rod, i.e., where steep flux gradients would be expected. Multigroup diffusion calculations have also been performed by Kaper et al.[7,15] using higher order (through fifth order) Lagrange polynomials with triangular elements. In their investigation, it was found that higher order approximation could lead to substantial savings of computation time when compared with low order finite difference approximations.

To obtain solutions to the transport equation both the spatial and angular variation of the flux must be determined. Thus several approaches are available depending on whether the spatial, the angular, or both the spatial and angular domains are approximated using finite elements. The weighted residual formulation using the Galerkin approach has been proposed by Ohnishi[16] to solve the discrete ordinates form of the transport equation. In another paper, Ohnishi[11] has suggested several different techniques in which finite elements are used to approximate the angular dependence of the flux.

Miller et al.[9,12] have applied the finite element method to obtain solutions to the second order form of the transport equation through the use of a minimum variational principle.[17] They employed both rectangular and triangular elements to approximate the spatial domain and rectangular elements to approximate the angular domain. Their results illustrated the absence of ray effects and the ability to treat nonorthogonal boundaries. Whereas they considered only monoenergetic

problems, Pitkaranta and Silvennoinen[18] using similar space-angle phase space elements,[19] have performed multigroup eignevalue calculations in one-dimensional spherical geometry. Although linear anisotropic scattering was considered in the one-dimensional work of Miller et al.,[19] it was neglected in two dimensions due to the difficulties encountered in constructing the one-dimensional functional.

More recently, Kaper et al.[20] have investigated the use of several finite element approximation procedures to obtain solutions of a multigroup form of the canonical even-odd parity flux equations. In this investigation, they utilized Lagrange polynomials to interpolate on a triangular mesh. However, unlike Miller et al.,[9,12] they did not restrict their investigation to only linear polynomials. In addition, they investigated the use of piecewise continuous polynomials, bicubic spline functions, spherical harmonics and a cubature procedure similar to discrete ordinates to approximate the angular domain. Of these approximations, they concluded that the cubature procedure, coupled to finite elements in space, provided the most promising alternative to traditional finite difference methods. However, as in other even-odd parity two-dimensional formulations, they did not consider anisotropic scattering.

To date, the code TRIPLET[21] represents the only production oriented application of the finite element method in the area of neutron transport. This code, developed by Reed et al.,[21] solves the multigroup discrete ordinates form of the transport equation using a triangular mesh. Within each triangle, the discrete angular fluxes are

approximated by Lagrange polynomials, which although normally continuous, are allowed to be discontinuous to reduce the possibility of calculating negative fluxes. A weighted residual formulation is used to obtain the necessary algebraic equations. Unlike previous applications of the finite element method,[9,12,18,19] an iterative rather than direct solution algorithm is employed. The iterative scheme, though efficient, does impose the use of a regular triangular mesh which could prove undesirable for geometrically complex problems. Finally, since this formulation is based on the discrete ordinates equations, anisotropic scattering was easily incorporated.

Objectives and Scope

The objective of this study was to develop and implement a method, similar to the cubature approach of Kaper et al.,[20] which includes a general treatment of anisotropic scattering to obtain approximate solutions to the multigroup two-dimensional transport equations. To accomplish this objective, each group equation of the multigroup transport equations was transformed into two equivalent group canonical even-odd parity flux equations[17] due to the angular symmetry properties of these equations. The angular domain was then approximated using discrete ordinates techniques similar to those employed by Mynatt[2] to facilitate the inclusion of anisotropic scattering. After combining these discretized equations, a reduced functional was constructed using the Galerkin approach and the self-adjoint properties of these equations. For simplicity and also to keep at a minimum the number of unknowns, linear Lagrange polynomials were chosen to represent the

spatial dependence of the even and odd parity fluxes using a general triangular mesh grid.

In the following chapter, a finite element formulation, not restricted to orthogonal geometrics, is developed to solve multigroup transport problems with anisotropic scattering. The numerical techniques employed in the implementation of this formulation are described in detail in Chapter III. In Chapter IV, results are presented for a series of calculations which were performed to evaluate the validity, usefulness, and limitations of the formulation. In Chapter V, conclusions resulting from this investigation and a number of recommendations to extend the formulation are presented. The similarities between the forward and adjoint canonical equations are illustrated in Appendix A. Finally, in Appendix B, a verification of the functionals used in this work is presented.

CHAPTER II

FORMALISM

In this chapter, a finite element formulation is developed to obtain approximate solutions to the multigroup two-dimensional transport equations. Primary emphasis is directed toward the use of a variational principle, the treatment of anisotropic scattering and the application to nonorthogonal geometries. Because of these latter two considerations, discrete angles and triangular elements are employed to approximate the angular and spatial domains, respectively.

Multigroup Transport Equations

The two-dimensional planar geometry, multigroup transport equations for G groups are[23]

$$\vec{\Omega}\cdot\vec{\nabla}\,\phi_g(x,y,\vec{\Omega}) + \Sigma_g(x,y)\,\phi_g(x,y,\vec{\Omega})$$

$$- \int_{\vec{\Omega}'} \Sigma_{sg\to g}(x,y;\,\vec{\Omega}'\cdot\vec{\Omega})\,\phi_g(x,y,\vec{\Omega}')\,d\vec{\Omega}'$$

$$= S_g(x,y,\vec{\Omega}) \text{ for } g = 1, \ldots, G. \qquad (2.1)$$

The multigroup source, $S_g(x,y,\vec{\Omega})$ is composed of downscatter, fission and extraneous sources; and is given by

$$S_g(x,y,\vec{\Omega}) = \sum_{g'=1}^{g-1} \int_{\vec{\Omega}'} \Sigma_{sg'\to g}(x,y,\vec{\Omega}'\cdot\vec{\Omega})\ \phi_{g'}(x,y,\vec{\Omega}')d\vec{\Omega}'$$

$$+ \frac{\chi_g(x,y)}{4\pi} \sum_{g'=1}^{G} \nu\Sigma_{fg'}(x,y) \int_{\vec{\Omega}'} \phi_{g'}(x,y,\vec{\Omega}')\ d\vec{\Omega}'$$

$$+ Q_g(x,y,\vec{\Omega}) \text{ for } g = 1, \ldots, G. \qquad (2.2)$$

The symbols in Equations (2.1) and (2.2) are defined as follows:

$\phi_g(x,y,\vec{\Omega})$ = the angular flux distribution as a function of the spatial coordinates x, y, and angular direction $\vec{\Omega}$ for group g

$\Sigma_g(x,y)$ = the macroscopic total cross section for group g

$\Sigma_{sg'\to g}(x,y;\ \vec{\Omega}'\cdot\vec{\Omega})$ = the macroscopic scattering cross section for scattering from group g', angular direction $\vec{\Omega}'$ to group g, angular direction $\vec{\Omega}$

$\chi_g(x,y)$ = the fraction of fission neutrons born in group g

$\nu\Sigma_{fg'}(x,y)$ = the number of neutrons produced due to fissions in group g'

$Q_g(x,y,\vec{\Omega})$ = the angular extraneous source distribution in group g.

Equation (2.1) describes the transport of neutrons in group g, and is defined on a two-dimensional convex region $\vec{r}$ and boundary surface $\vec{s}$. The two boundary conditions normally associated with Equation (2.1) are

the vacuum or nonreentrant condition and the spectral reflection or symmetry condition. These two conditions may be written

$$\phi_g(x,y,\Omega)\Big|_{\vec{s}} = 0 \qquad \text{for } \vec{\Omega} \cdot \vec{n} < 0, \text{ and all } g \tag{2.3}$$

and

$$\phi_g(x,y,\vec{\Omega})\Big|_{\vec{s}} = \phi_g(x,y,\vec{\Omega}^*)\Big|_{\vec{s}} \qquad \text{for all } g. \tag{2.4}$$

The symbol $\vec{n}$ represents the outward directed normal of $\vec{s}$, and the angular direction $\vec{\Omega}^*$ is defined by $\vec{\Omega}^* \cdot \vec{n} = -\vec{\Omega} \cdot \vec{n}$ and $(\vec{\Omega}^* \times \vec{\Omega}) \cdot \vec{n} = 0$.

Due to the first-order differential operator in Equation (2.1), the one-group transport equation is not self-adjoint. In order to find a self-adjoint variational principle, it is necessary to remove this nonself-adjointness. Thus, rather than proceed directly with a discrete angle approximation, it is first necessary to transform Equation (2.1) to accomplish the objective of obtaining a variational principle. This transformation is presented in the next section.

Even-Odd Parity Transformation

To simplify the notation, Equation (2.1) is rewritten as

$$\vec{\Omega}\cdot\vec{\nabla}\,\phi(\vec{\Omega}) + \Sigma\phi(\vec{\Omega})$$

$$- \int_{\vec{\Omega}'} \Sigma_s(\vec{\Omega}'\cdot\vec{\Omega})\,\phi(\Omega')\,d\vec{\Omega}' = S(\vec{\Omega}), \tag{2.5}$$

where the group index g and spatial coordinates x and y have been dropped. Since Equation (2.5) is equally valid for neutrons traveling in the opposite direction of $\vec{\Omega}$, it may also be written

$$- \vec{\Omega}\cdot\vec{\nabla}\,\phi(-\vec{\Omega}) + \Sigma\,\phi(-\vec{\Omega})$$

$$- \int_{\vec{\Omega}'} \Sigma_s(\vec{\Omega}'\cdot-\vec{\Omega})\,\phi(\vec{\Omega}')\,d\vec{\Omega}' = S(-\vec{\Omega}). \qquad (2.6)$$

To proceed, it is necessary to decompose the angular flux $\phi(\vec{\Omega})$ into even and odd parity angular fluxes as

$$\phi(\vec{\Omega}) = \psi^e(\vec{\Omega}) + \psi^o(\vec{\Omega}) \qquad (2.7)$$

where the even parity angular flux is defined by

$$\psi^e(\vec{\Omega}) = [\phi(\vec{\Omega}) + \phi(-\vec{\Omega})]/2 \qquad (2.8)$$

and the odd parity angular flux is defined by

$$\psi^o(\vec{\Omega}) = [\phi(\vec{\Omega}) - \phi(-\vec{\Omega})]/2. \qquad (2.9)$$

In addition, even and odd parity scattering cross sections are defined by

$$\Sigma_s^e(\vec{\Omega}'\cdot\vec{\Omega}) = [\Sigma_s(\vec{\Omega}'\cdot\vec{\Omega}) + \Sigma_s(\vec{\Omega}'\cdot-\vec{\Omega})]/2,$$

$$\Sigma_s^o(\vec{\Omega}'\cdot\vec{\Omega}) = [\Sigma_s(\vec{\Omega}'\cdot\vec{\Omega}) - \Sigma_s(\vec{\Omega}'\cdot-\vec{\Omega})]/2 \qquad (2.10)$$

and even and odd parity angular sources are defined by

$$S^e(\vec{\Omega}) = [S(\vec{\Omega}) + S(-\vec{\Omega})]/2,$$

$$S^o(\vec{\Omega}) = [S(\vec{\Omega}) - S(-\vec{\Omega})]/2. \qquad (2.11)$$

Adding Equation (2.6) to Equation (2.5) yields

$$\vec{\Omega}\cdot\vec{\nabla}\psi^{o}(\vec{\Omega}) + \Sigma\ \psi^{e}(\vec{\Omega})$$

$$- \int_{\vec{\Omega}'} \Sigma_s^{e}(\vec{\Omega}'\cdot\vec{\Omega})\ \phi(\vec{\Omega}')\ d\vec{\Omega} = S^{e}(\vec{\Omega})$$

and subtracting Equation (2.6) from Equation (2.5) yields

$$\vec{\Omega}\cdot\vec{\nabla}\psi^{e}(\vec{\Omega}) + \Sigma\ \psi^{o}(\vec{\Omega})$$

$$- \int_{\vec{\Omega}'} \Sigma_s^{o}(\vec{\Omega}'\cdot\vec{\Omega})\ \phi(\vec{\Omega}')d\vec{\Omega}' = S^{o}(\vec{\Omega}).$$

The transformation is completed by decomposing $\phi(\vec{\Omega}')$ in the scattering integrals and noting

$$\int_{\vec{\Omega}'} \Sigma_s^{e}(\vec{\Omega}'\cdot\vec{\Omega})\ \psi^{o}(\vec{\Omega}')\ d\vec{\Omega}'$$

$$= \int_{\vec{\Omega}'} \Sigma_s^{o}(\vec{\Omega}'\cdot\vec{\Omega})\ \psi^{e}(\vec{\Omega}')\ d\vec{\Omega}' = 0. \qquad (2.12)$$

This final step yields

$$\vec{\Omega}\cdot\vec{\nabla}\psi^{o}(\vec{\Omega}) + \Sigma\ \psi^{e}(\vec{\Omega})$$

$$- \int_{\vec{\Omega}'} \Sigma_s^{e}(\vec{\Omega}'\cdot\vec{\Omega})\psi^{e}(\vec{\Omega}')\ d\vec{\Omega}' = S^{e}(\vec{\Omega}), \qquad (2.13)$$

and

$$\vec{\Omega}\cdot\vec{\nabla}\psi^{e}(\vec{\Omega}) + \Sigma\ \psi^{o}(\vec{\Omega})$$

$$- \int_{\vec{\Omega}'} \Sigma_s^{o}(\vec{\Omega}'\cdot\vec{\Omega})\ \psi^{o}(\vec{\Omega}')\ d\vec{\Omega}' = S^{o}(\vec{\Omega}). \qquad (2.14)$$

Equations (2.13) and (2.14) are a pair of coupled first-order differential integral equations. Together they represent the canonical

form of the transport equation.[17] The boundary conditions corresponding to Equation (2.3) and (2.4) are respectively

$$\left[\psi^e(\vec{\Omega}) + \psi^o(\vec{\Omega})\right]\Big|_{\vec{s}} = 0 \quad \text{for } \vec{\Omega} \cdot \vec{n} < 0;$$

$$\left[\psi^e(\vec{\Omega}) - \psi^o(\vec{\Omega})\right]\Big|_{\vec{s}} = 0 \quad \text{for } \vec{\Omega} \cdot \vec{n} > 0 \tag{2.15}$$

and

$$\psi^e(\vec{\Omega})\Big|_{\vec{s}} = \psi^e(\vec{\Omega}^*)\Big|_{\vec{s}} \quad ;$$

$$\psi^o(\vec{\Omega})\Big|_{\vec{s}} = \psi^o(\vec{\Omega}^*)\Big|_{\vec{s}} \tag{2.16}$$

where $\vec{\Omega}^*$ is as previously defined. In Appendix A, the similarities between Equations (2.13), (2.14), and (2.15) and their adjoint forms are illustrated.

Variational principles whose Euler equations are Equations (2.13) and (2.14) have been constructed and employed with certain synthesis schemes.[24] However, in these principles, the even and odd parity fluxes are coupled directly in the calculational scheme. This coupling would unnecessarily complicate the formulation developed in this work by doubling the number of unknowns. Therefore, to circumvent this problem, Equations (2.13) and (2.14) are solved for $\psi^e(\vec{\Omega})$ and $\psi^o(\vec{\Omega})$, respectively.

To accomplish this last objective, Equation (2.13) is rewritten

$$- \vec{\Omega}\cdot\vec{\nabla}\psi^{o}(\vec{\Omega}) + S^{e}(\vec{\Omega})$$

$$= \Sigma\ \psi^{e}(\vec{\Omega}) - \int_{\vec{\Omega}'} \Sigma_{s}^{e}(\vec{\Omega}'\cdot\vec{\Omega})\ \psi^{e}(\vec{\Omega}')\ d\vec{\Omega}'. \qquad (2.17)$$

Since the scattering cross section is a function of the angle between the initial and final directions, i.e., $\vec{\Omega}'\cdot\vec{\Omega}$, it may be expanded in Legendre polynomials to obtain

$$\Sigma_{s}(\vec{\Omega}'\cdot\vec{\Omega}) = \sum_{\ell=0}^{\infty} \frac{(2\ell+1)}{4\pi}\ \Sigma_{s\ell}\ P_{\ell}(\vec{\Omega}'\cdot\vec{\Omega})$$

where the scattering coefficients $\Sigma_{s\ell}$ are generated from

$$\Sigma_{s\ell} = 2\pi \int_{-1}^{1} \Sigma_{s}(\vec{\Omega}'\cdot\vec{\Omega})\ P_{\ell}(\vec{\Omega}'\cdot\vec{\Omega})\ d(\vec{\Omega}'\cdot\vec{\Omega}).$$

Noting that $P_{\ell}(\vec{\Omega}'\cdot\vec{\Omega}) = - P_{\ell}(\vec{\Omega}'\cdot\vec{\Omega})$ for ℓ odd, and the definition of $\Sigma_{s}^{e}(\vec{\Omega}'\cdot\vec{\Omega})$, Equation (2.10) yields

$$\Sigma_{s}^{e}(\vec{\Omega}'\cdot\vec{\Omega}) = \sum_{\ell\ \text{even}} \frac{(2\ell+1)}{4\pi}\ \Sigma_{s\ell}\ P_{\ell}(\vec{\Omega}'\cdot\vec{\Omega}). \qquad (2.18)$$

The Legendre polynomials may be expanded in spherical harmonics through the addition theorem,[25] i.e.,

$$P_{\ell}(\vec{\Omega}'\cdot\vec{\Omega}') = \frac{4\pi}{2\ell+1} \sum_{m=-\ell}^{\ell} Y_{\ell m}(\vec{\Omega})\ \bar{Y}_{\ell m}(\vec{\Omega}') \qquad (2.19)$$

where the $Y_{\ell m}(\vec{\Omega})$ are the orthonormal surface harmonics and the superscript bar denotes complex conjugate. Substitution of Equation (2.19) into (2.18) and this result into Equation (2.17) yields

$$f(\vec{\Omega}) = \Sigma\ \psi^e(\vec{\Omega})$$

$$- \sum_{\ell\ \text{even}} \Sigma_{s\ell} \sum_{m=-\ell}^{\ell} Y_{\ell m}(\vec{\Omega}) \int_{\vec{\Omega}'} \bar{Y}_{\ell m}(\vec{\Omega}')\ \psi^e(\vec{\Omega}')\ d\vec{\Omega}' \qquad (2.20)$$

where $f(\vec{\Omega}) = -\ \vec{\Omega}\cdot\vec{\nabla}\psi^o(\vec{\Omega}) + S^e(\vec{\Omega})$. Multiplying Equation (2.20) by $\bar{Y}_{\ell' m'}(\vec{\Omega})$ and integrating over all $\vec{\Omega}$ yields after some rearrangement

$$\int_{\vec{\Omega}'} \bar{Y}_{\ell m}(\vec{\Omega}')\ \psi^e(\vec{\Omega}')\ d\vec{\Omega}'$$

$$= [\Sigma - \Sigma_{s\ell}]^{-1} \int_{\vec{\Omega}'} \bar{Y}_{\ell m}(\vec{\Omega}')\ f(\vec{\Omega}')\ d\vec{\Omega}'$$

which when substituted into Equation (2.20) along with the definition of $f(\vec{\Omega})$ yields

$$\psi^e(\vec{\Omega}) = \{S^e(\vec{\Omega}) - \vec{\Omega}\cdot\vec{\nabla}\psi^o(\vec{\Omega})$$

$$+ \sum_{\ell\ \text{even}} \frac{\Sigma_{s\ell}}{[\Sigma - \Sigma_{s\ell}]} \sum_{m=-\ell}^{\ell} Y_{\ell m}(\vec{\Omega})$$

$$\times \int_{\vec{\Omega}'} \bar{Y}_{\ell m}(\vec{\Omega}')\ [S^e(\vec{\Omega}') - \vec{\Omega}'\cdot\vec{\nabla}\psi^o(\vec{\Omega}')]\ d\vec{\Omega}'\}/\Sigma. \qquad (2.21)$$

By similarly expanding the odd parity cross section as

$$\Sigma_s^o(\vec{\Omega}'\cdot\vec{\Omega}) = \sum_{\ell\ \text{odd}} \frac{(2\ell+1)}{4\pi} \Sigma_{s\ell}\ P_\ell(\vec{\Omega}'\cdot\vec{\Omega}) \qquad (2.22)$$

and performing the same operations with regard to Equation (2.14) there results

$$\psi^{o}(\vec{\Omega}) = \{S^{o}(\vec{\Omega}) - \vec{\Omega}\cdot\vec{\nabla}\psi^{e}(\vec{\Omega})$$

$$+ \sum_{\ell \text{ odd}} \frac{\Sigma_{s\ell}}{[\Sigma-\Sigma_{s\ell}]} \sum_{m=-\ell}^{\infty} Y_{\ell m}(\vec{\Omega})$$

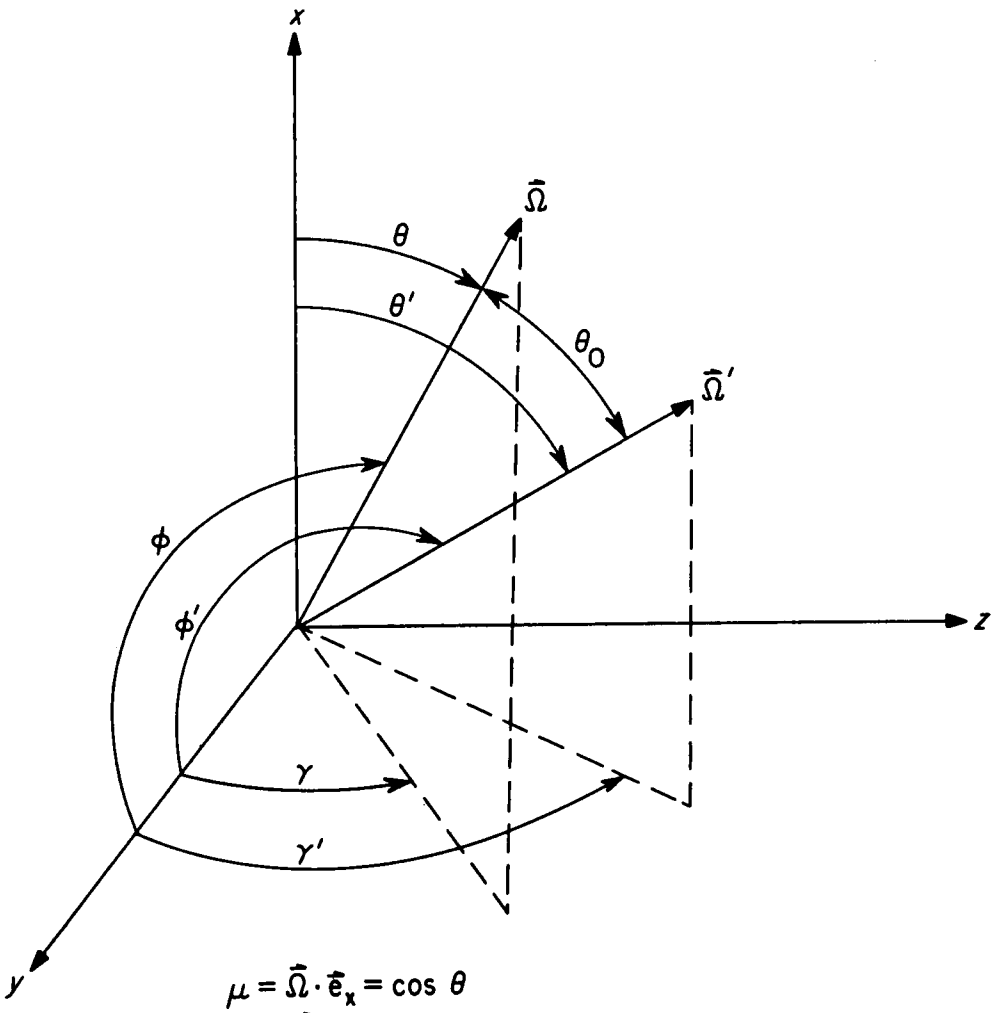
$$\times \int_{\vec{\Omega}'} \bar{Y}_{\ell m}(\vec{\Omega}') \; [S^{o}(\vec{\Omega}') - \vec{\Omega}'\cdot\vec{\nabla}\psi^{e}(\vec{\Omega}')] \; d\vec{\Omega}'\}/\Sigma. \qquad (2.23)$$

It is evident that the substitution of Equation (2.23) into (2.13) yields a second-order differential equation in $\psi^{e}(\vec{\Omega})$. Likewise, substitution of Equation (2.21) into (2.14) produces the same result for $\psi^{o}(\vec{\Omega})$. Thus, the nonself-adjointness of the first order differential operator in Equation (2.1) has been removed by obtaining second order equations. However, rather than perform these substitutions, it is more convenient to first discretize the angular domain.

Discrete Angle Approximation

In this section, a discrete angle approximation will be applied to Equations (2.13), (2.14), (2.21), and (2.23) to obtain discrete ordinates "like" even-odd parity second-order equations. For the sake of brevity, the development will be limited to Equations (2.13) and (2.23) since a similar approach yields the same result with regard to Equations (2.14) and (2.21). To begin, Figure 1 is introduced to aid in the development of these equations.

ORNL-DWG 75-12093



$$\mu = \vec{\Omega} \cdot \vec{e}_x = \cos\theta$$
$$\mu' = \vec{\Omega}' \cdot \vec{e}_x = \cos\theta'$$
$$\eta = \vec{\Omega} \cdot \vec{e}_y = \sin\theta \cos\gamma$$
$$\eta' = \vec{\Omega}' \cdot \vec{e}_y = \sin\theta' \cos\gamma'$$
$$\vec{\Omega}' \cdot \vec{\Omega} = \cos\theta_0$$

Figure 1. Coordinate system for particle scattering in rectangular geometry.

In order to have Equations (2.13) and (2.23) in a form amenable to angular discretization, an alternate form of the Legendre addition theorem[25] is introduced

$$P_\ell(\vec{\Omega}'\cdot\vec{\Omega}) = P_\ell(\mu)\ P_\ell(\mu') +$$

$$2 \sum_{m=1}^{\ell} \frac{(\ell-m)!}{(\ell+m)!} P_\ell^m(\mu)\ P_\ell^m(\mu')$$

$$\times [\cos m\gamma \cos m\gamma' + \sin m\gamma \sin m\gamma'] \qquad (2.24)$$

where μ, μ', γ and γ' are defined in Figure 1. Using Equations (2.18), (2.19) and (2.24) allows the integral terms in Equations (2.13) and (2.23) to be written

$$\sum_{\ell \text{ even}} \frac{(2\ell+1)}{4\pi} \Sigma_{s\ell} \int_{\vec{\Omega}'} [P_\ell(\mu)\ P_\ell(\mu') +$$

$$2 \sum_{m=1}^{\ell} \frac{(\ell-m)!}{(\ell+m)!} P_\ell^m(\mu)\ P_\ell^m(\mu')$$

$$\times (\cos m\gamma \cos m\gamma' + \sin m\gamma \sin m\gamma')]\ \psi^e(\vec{\Omega}')\ d\vec{\Omega}'$$

and

$$\frac{1}{\Sigma} \sum_{\ell \text{ odd}} \frac{(2\ell+1)}{4\pi} \frac{\Sigma_{s\ell}}{[\Sigma-\Sigma_{s\ell}]} \int_{\vec{\Omega}'} [P_\ell(\mu)\ P_\ell(\mu') +$$

$$2 \sum_{m=1}^{\ell} \frac{(\ell-m)!}{(\ell+m)!} P_\ell^m(\mu)\ P_\ell^m(\mu')$$

$$\times (\cos m\gamma \cos m\gamma' + \sin m\gamma \sin m\gamma')]$$

$$\times [S^o(\vec{\Omega}') - \vec{\Omega}'\cdot\vec{\nabla}\psi^e(\vec{\Omega}')]\, d\vec{\Omega}'.$$

Due to symmetry in the Z direction $\psi^e(\vec{\Omega}')$, $S^o(\vec{\Omega}')$ and $\vec{\Omega}'\cdot\vec{\nabla}\psi^e(\vec{\Omega}')$ are all even functions of γ', thus all terms involving sin $m\gamma'$ drop out of the integrals. Equations (2.13) and (2.23) may now be rewritten

$$\vec{\Omega}\cdot\vec{\nabla}\psi^o(\vec{\Omega}) + \Sigma\, \psi^e(\vec{\Omega}) -$$

$$\sum_{\ell \text{ even}} \frac{(2\ell+1)}{4\pi} \Sigma_{s\ell} \sum_{m=0}^{\ell} R_\ell^m(\mu,\gamma) \int_{\vec{\Omega}'} R_\ell^m(\mu',\gamma')\, \psi^e(\vec{\Omega}')\, d\vec{\Omega}'$$

$$= S^e(\vec{\Omega}) \qquad (2.25)$$

and

$$\psi^o(\vec{\Omega}) = \{S^o(\vec{\Omega}) - \vec{\Omega}\cdot\vec{\nabla}\psi^e(\vec{\Omega}) +$$

$$\sum_{\ell \text{ odd}} \frac{(2\ell+1)}{4\pi} \frac{\Sigma_{s\ell}}{[\Sigma-\Sigma_{s\ell}]} \sum_{m=0}^{\ell} R_\ell^m(\mu,\gamma)$$

$$\times \int_{\vec{\Omega}'} R_\ell^m(\mu',\gamma')\, [S^o(\vec{\Omega}') - \vec{\Omega}'\cdot\vec{\nabla}\psi^e(\vec{\Omega}')]\, d\vec{\Omega}'\}/\Sigma \qquad (2.26)$$

where the functions $R_\ell^m(\mu,\gamma)$ are defined by

$$R_\ell^m(\mu,\gamma) = P_\ell(\mu) \quad \text{for } m = 0$$

$$R_\ell^m(\mu,\gamma) = \left[\frac{2(\ell-m)!}{(\ell+m)!}\right]^{1/2} P_\ell^m(\mu) \cos m\gamma \quad \text{for } m \neq 0.$$

To obtain the discrete ordinates "like" form of Equations (2.25) and (2.26), the following equations are written

$$\int_{\Delta\vec{\Omega}_d} f(\vec{\Omega})\, d\vec{\Omega} \cong f_d w_d \tag{2.27}$$

where

$$f_d = 4\pi f(\bar{\vec{\Omega}}_d)$$

and

$$\int_{\Delta\vec{\Omega}_d} d\vec{\Omega} = 4\pi w_d .$$

The superscript bar over $\vec{\Omega}_d$ is introduced to denote that the $\vec{\Omega}_d$'s are chosen such that the integrals over solid angle may be suitably approximated by a single summation over D discrete points and weights, i.e.

$$\int_{\vec{\Omega}'} f(\vec{\Omega}')\, d\vec{\Omega}' \cong \sum_{d'=1}^{D} f_{d'} w_{d'} . \tag{2.28}$$

Application of the approximations given by Equations (2.27) and (2.28) to Equations (2.25) and (2.26) yield

$$\bar{\vec{\Omega}}_d \cdot \vec{\nabla}\psi^o_d\, w_d + \Sigma\psi^e_d\, w_d -$$

$$\sum_{\ell \text{ even}} (2\ell+1)\, \Sigma_{s\ell} \sum_{m=0}^{\ell} w_d\, R^m_{\ell,d} \sum_{d'=1}^{D} R^m_{\ell',d'} w_{d'}\, \psi^e_{d'}$$

$$= S^e_d w_d$$

$$\text{for } d = 1, \ldots, D \tag{2.29}$$

and

$$\psi_d^o w_d = \{[S_d^o - \bar{\vec{\Omega}}_d \cdot \vec{\nabla}\psi_d^e]\, w_d +$$

$$\sum_{\ell \text{ odd}} \frac{(2\ell+1)\,\Sigma_{s\ell}}{[\Sigma-\Sigma_{s\ell}]} \sum_{m=0}^{\ell} w_d R_{\ell,d}^m \sum_{d'=1}^{D} R_{\ell,d'}^m w_{d'} [S_{d'}^o - \bar{\vec{\Omega}}_{d'} \cdot \vec{\nabla}\psi_{d'}^e]\}/\Sigma$$

$$\text{for } d = 1, \ldots, D \qquad (2.30)$$

where

$$R_{\ell,d}^m = P_\ell(\bar{\mu}_d) \qquad \text{for } m = 0$$

$$R_{\ell,d}^m = \left[\frac{2(\ell-m)!}{(\ell+m)!}\right]^{1/2} P_\ell^m(\bar{\mu}_d) \cos m\bar{\gamma}_d \qquad \text{for } m \neq 0.$$

By defining the following matrices

$$\underline{\underline{\vec{\Omega}}} \equiv \begin{pmatrix} \bar{\vec{\Omega}}_1 & & 0 \\ & \ddots & \\ 0 & & \bar{\vec{\Omega}}_D \end{pmatrix}, \quad \underline{\underline{w}} \equiv \begin{pmatrix} w_1 & & 0 \\ & \ddots & \\ 0 & & w_D \end{pmatrix},$$

$$\underline{\underline{H}}^{\ell m} \equiv \begin{pmatrix} w_1 R_{\ell,1}^m & R_{\ell,1}^m w_1 & \cdots & w_1 R_{\ell,1}^m & R_{\ell,D}^m w_D \\ & & & & \\ w_D R_{\ell,D}^m & R_{\ell,1}^m w_1 & \cdots & w_D R_{\ell,D}^m & R_{\ell,D}^m w_D \end{pmatrix},$$

and vectors

$$\underline{\psi}^{e} \equiv \begin{pmatrix} \psi_1^e \\ \cdot \\ \cdot \\ \psi_D^e \end{pmatrix}, \quad \underline{\psi}^{o} \equiv \begin{pmatrix} \psi_1^o \\ \cdot \\ \cdot \\ \psi_D^o \end{pmatrix}, \quad \underline{S}^{e} \equiv \begin{pmatrix} S_1^e \\ \cdot \\ \cdot \\ S_D^e \end{pmatrix}$$

and

$$\underline{S}^{o} \equiv \begin{pmatrix} S_1^o \\ \cdot \\ \cdot \\ S_D^o \end{pmatrix}; \tag{2.31}$$

Equations (2.29) and (2.30) may be written in compact form as

$$\underline{\underline{\vec{\Omega}}}\cdot\vec{\nabla}\ \underline{\underline{w}}\ \underline{\psi}^{o} + \Sigma\ \underline{\underline{w}}\ \underline{\psi}^{e} - \underline{\underline{H}}^{e}\underline{\psi}^{e} = \underline{\underline{w}}\ \underline{S}^{e} \tag{2.32}$$

and

$$\underline{\underline{w}}\ \underline{\psi}^{o} = \{\underline{\underline{w}}\ \underline{S}^{o} - \underline{\underline{\vec{\Omega}}}\cdot\vec{\nabla}\ \underline{\underline{w}}\ \underline{\psi}^{e} +$$

$$\underline{\underline{G}}^{o}[\underline{S}^{o} - \underline{\underline{\vec{\Omega}}}\cdot\vec{\nabla}\ \underline{\psi}^{e}]\}/\Sigma \tag{2.33}$$

where

$$\underline{\underline{H}}^{e} = \sum_{\ell\ \text{even}} (2\ell+1)\ \Sigma_{s\ell} \sum_{m=0}^{\ell} \underline{\underline{H}}^{\ell m};$$

$$\underline{\underline{G}}^{o} = \sum_{\ell\ \text{odd}} \frac{(2\ell+1)\ \Sigma_{s\ell}}{[\Sigma-\Sigma_{s\ell}]} \sum_{m=0}^{\ell} \underline{\underline{H}}^{\ell m}. \tag{2.34}$$

By applying an equivalent procedure to Equations (2.14) and (2.21), there results

$$\vec{\underline{\Omega}}\cdot\vec{\nabla}\,\underline{\underline{w}}\,\underline{\psi}^{e} + \Sigma\,\underline{\underline{w}}\,\underline{\psi}^{o} - \underline{\underline{H}}^{o}\underline{\psi}^{o} = \underline{\underline{w}}\,\underline{S}^{o} \tag{2.35}$$

and

$$\underline{\underline{w}}\,\underline{\psi}^{e} = \{\underline{\underline{w}}\,\underline{S}^{e} - \vec{\underline{\Omega}}\cdot\vec{\nabla}\,\underline{\underline{w}}\,\underline{\psi}^{o} + \underline{\underline{G}}^{e}[\underline{S}^{e} - \vec{\underline{\Omega}}\cdot\vec{\nabla}\,\underline{\psi}^{o}]\}/\Sigma \tag{2.36}$$

where

$$\underline{\underline{H}}^{o} = \sum_{\ell\ \text{odd}} (2\ell+1)\,\Sigma_{s\ell} \sum_{m=0}^{\ell} \underline{\underline{H}}^{\ell m}\ ;$$

$$\underline{\underline{G}}^{e} = \sum_{\ell\ \text{even}} \frac{(2\ell+1)\,\Sigma_{s\ell}}{[\Sigma-\Sigma_{s\ell}]} \sum_{m=0}^{\ell} \underline{\underline{H}}^{\ell m}. \tag{2.37}$$

The final result is obtained by substituting Equation (2.33) into (2.32),

$$\begin{aligned} &- \vec{\underline{\Omega}}\cdot\vec{\nabla}(\vec{\underline{\Omega}}\cdot\vec{\nabla}\,\underline{\underline{w}}\,\underline{\psi}^{e}/\Sigma) + \vec{\underline{\Omega}}\cdot\vec{\nabla}(\underline{\underline{w}}\,\underline{S}^{o}/\Sigma) \\ &+ \vec{\underline{\Omega}}\cdot\vec{\nabla}(\underline{\underline{G}}^{o}\,\underline{S}^{o}/\Sigma) - \vec{\underline{\Omega}}\cdot\vec{\nabla}(\underline{\underline{G}}^{o}\,\vec{\underline{\Omega}}\cdot\vec{\nabla}\psi^{e}/\Sigma) \\ &+ \Sigma\,\underline{\underline{w}}\,\underline{\psi}^{e} - \underline{\underline{H}}^{e}\underline{\psi}^{e} - \underline{\underline{w}}\,\underline{S}^{e} = \underline{0} \end{aligned} \tag{2.38}$$

and by substituting Equation (2.36) into (2.35),

$$\begin{aligned} &- \vec{\underline{\Omega}}\cdot\vec{\nabla}(\vec{\underline{\Omega}}\cdot\vec{\nabla}\,\underline{\underline{w}}\,\underline{\psi}^{o}/\Sigma) + \vec{\underline{\Omega}}\cdot\vec{\nabla}(\underline{\underline{w}}\,\underline{S}^{e}/\Sigma) \\ &+ \vec{\underline{\Omega}}\cdot\vec{\nabla}(\underline{\underline{G}}^{e}\,\underline{S}^{e}/\Sigma) - \vec{\underline{\Omega}}\cdot\vec{\nabla}(\underline{\underline{G}}^{e}\,\vec{\underline{\Omega}}\cdot\vec{\nabla}\,\underline{\psi}^{o}/\Sigma) \\ &+ \Sigma\,\underline{\underline{w}}\,\underline{\psi}^{o} - \underline{\underline{H}}^{o}\psi^{o} - \underline{\underline{w}}\,\underline{S}^{o} = \underline{0}. \end{aligned} \tag{2.39}$$

To complete this section, Equation (2.27) is applied to Equations (2.15) and (2.16) to obtain the boundary conditions in discrete-ordinate form, i.e.

$$\left[\psi_d^e + \psi_d^o\right]\Big|_{\vec{s}} = 0 \qquad \text{for } \vec{\Omega}_d \cdot \vec{n} < 0;$$

$$\left[\psi_d^e - \psi_d^o\right]\Big|_{\vec{s}} = 0 \qquad \text{for } \vec{\Omega}_d \cdot \vec{n} > 0 \tag{2.40}$$

and

$$\psi_d^e\Big|_{\vec{s}} = \psi_{d*}^e\Big|_{\vec{s}} \quad ;$$

$$\psi_d^o\Big|_{\vec{s}} = \psi_{d*}^o\Big|_{\vec{s}} \quad . \tag{2.41}$$

In obtaining Equation (2.41), it was assumed that $w_d = w_d{}^*$.

Construction of Reduced Functional

The objective of this section is to formulate variational principles "equivalent" to Equations (2.38) and (2.39). To accomplish this objective, reduced functionals (reduced implies that the angular domain is not to be considered part of the functional domain) will be constructed using a Galerkin approach.[10] Again, for the sake of brevity, only the functional whose first variation with respect to $\underline{\psi}^e$ yields Equation (2.38) as an Euler equation will be constructed in detail.

To begin, the left side of Equation (2.38) is multiplied by $\delta(\underline{\psi}^e)^T$ and integrated over $\vec{r}$, i.e., the x-y plane, to give

$$\int_{\vec{r}} d\vec{r}\{-\delta(\underline{\psi}^e)^T\,\underline{\underline{\vec{\Omega}}}\cdot\vec{\nabla}(\underline{\underline{\vec{\Omega}}}\cdot\vec{\nabla}\,\underline{\underline{w}}\,\underline{\psi}^e/\Sigma) + \delta(\underline{\psi}^e)^T\,\underline{\underline{\vec{\Omega}}}\cdot\vec{\nabla}(\underline{\underline{w}}\,\underline{S}^o/\Sigma)$$

$$+ \delta(\underline{\psi}^e)^T\,\underline{\underline{\vec{\Omega}}}\cdot\vec{\nabla}(\underline{\underline{G}}^o\underline{S}^o/\Sigma) - \delta(\underline{\psi}^e)^T\,\underline{\underline{\vec{\Omega}}}\cdot\vec{\nabla}(\underline{\underline{G}}^o\,\underline{\underline{\vec{\Omega}}}\cdot\vec{\nabla}\,\underline{\psi}^e/\Sigma)$$

$$+\delta(\underline{\psi}^e)^T\,\Sigma\,\underline{\underline{w}}\,\underline{\psi}^e - \delta(\underline{\psi}^e)^T\,\underline{\underline{H}}^e\underline{\psi}^e - \delta(\underline{\psi}^e)^T\,\underline{\underline{w}}\,\underline{S}^e\} \qquad (2.42)$$

where δ represents the variation derivative, i.e., δa implies the variation of a, and the superscript T denotes matrix transpose. From the definitions of $\underline{\underline{\vec{\Omega}}}$, $\underline{\underline{w}}$, $\underline{\underline{H}}^e$, and $\underline{\underline{G}}^o$, it is obvious that each of these matrices is symmetric, i.e., $(\underline{\underline{\vec{\Omega}}})^T = \underline{\underline{\vec{\Omega}}}$ etc. Using this fact and the vector identity[26]

$$\vec{\nabla}\cdot(a\vec{b}) = a\vec{\nabla}\cdot\vec{b} + (\vec{\nabla}a)\cdot\vec{b}$$

allows the following equation to be written

$$\underline{\underline{\vec{\Omega}}}\cdot\vec{\nabla}\underline{f} = \vec{\nabla}\cdot\underline{\underline{\vec{\Omega}}}\underline{f} \qquad (2.43)$$

since

$$\nabla\cdot\underline{\underline{\vec{\Omega}}} = 0.$$

In addition, from Equation (2.43)

$$[\underline{\underline{\vec{\Omega}}}\cdot\vec{\nabla}\underline{f}]^T = \vec{\nabla}\cdot\,(\underline{f})^T\,\underline{\underline{\vec{\Omega}}}. \qquad (2.44)$$

Utilizing Equations (2.43) and (2.44) and the vector identity thus allows

$$(\underline{a})^T\,\underline{\underline{\vec{\Omega}}}\cdot\vec{\nabla}\underline{f} = \vec{\nabla}\cdot[(\underline{a})^T\,\underline{\underline{\vec{\Omega}}}\underline{f}] - [\underline{\underline{\vec{\Omega}}}\cdot\vec{\nabla}\underline{a}]^T\,\underline{f} \qquad (2.45)$$

to be written. Applying Equation (2.45) to expression (2.42) yields after much rearrangement

$$\int_{\vec{r}} d\vec{r}\{[\vec{\underline{\underline{\Omega}}}\cdot\vec{\nabla}\ \delta\ \underline{\psi}^e]^T\ \underline{\underline{w}}[\vec{\underline{\underline{\Omega}}}\cdot\vec{\nabla}\ \underline{\psi}^e]/\Sigma + \delta(\underline{\psi}^e)^T\ \Sigma\ \underline{\underline{w}}\ \underline{\psi}^e$$

$$+ [\vec{\underline{\underline{\Omega}}}\cdot\vec{\nabla}\ \delta\ \underline{\psi}^e]^T\ \underline{\underline{G}}^o[\vec{\underline{\underline{\Omega}}}\cdot\vec{\nabla}\ \underline{\psi}^e]/\Sigma - \delta(\underline{\psi}^e)^T\ \underline{\underline{H}}^e\underline{\psi}^e$$

$$- [\vec{\underline{\underline{\Omega}}}\cdot\vec{\nabla}\ \delta\ \underline{\psi}^e]^T\ \underline{\underline{G}}^o\ \underline{S}^o/\Sigma - [\vec{\underline{\underline{\Omega}}}\cdot\vec{\nabla}\ \delta\ \underline{\psi}^e]^T\ \underline{\underline{w}}\ \underline{S}^o/\Sigma$$

$$- \delta(\underline{\psi}^e)^T\ \underline{\underline{w}}\ \underline{S}^e\} +$$

$$\int_{\vec{r}} d\vec{r}\ \vec{\nabla}\cdot\{\delta(\underline{\psi}^e)^T\ \vec{\underline{\underline{\Omega}}}\{\underline{\underline{w}}\ \underline{S}^o - \vec{\underline{\underline{\Omega}}}\cdot\vec{\nabla}\ \underline{\underline{w}}\ \underline{\psi}^e +$$

$$\underline{\underline{G}}^o[\underline{S}^o - \vec{\underline{\underline{\Omega}}}\cdot\vec{\nabla}\ \psi^e]\}/\Sigma\}. \qquad (2.46)$$

From Equation (2.33), the second integral in expression (2.46) may be written

$$\int_{\vec{r}} d\vec{r}\ \vec{\nabla}\cdot\{\delta(\underline{\psi}^e)^T\ \vec{\underline{\underline{\Omega}}}\ \underline{\underline{w}}\ \underline{\psi}^o\}. \qquad (2.47)$$

If the discrete angular flux ϕ_d is to be spatially continuous, then ψ_d^e and ψ_d^o must be continuous. Imposing this physical restriction and using the divergence theorem[27] allows expression (2.47) to be written

$$\int_{\vec{s}} d\vec{s}\{\delta(\underline{\psi}^e)^T\ \vec{n}\cdot\vec{\underline{\underline{\Omega}}}\ \underline{\underline{w}}\ \underline{\psi}^o\}. \qquad (2.48)$$

The desired form of expression (2.48) may be obtained by decomposing $\underline{\psi}^e$ and $\underline{\psi}^o$ as

$$\underline{\psi}^e = \underline{\psi}_1^e + \underline{\psi}_2^e ,$$

$$\underline{\psi}^o = \underline{\psi}_1^o + \underline{\psi}_2^o \tag{2.49}$$

where the d^{th} components are defined by

$$\psi_{1d}^e = \psi_d^e ,$$

$$\psi_{1d}^o = \psi_d^o \qquad \text{for } \vec{\Omega}_d \cdot \vec{n} < 0 \tag{2.50}$$

and

$$\psi_{2d}^e = \psi_d^e ,$$

$$\psi_{2d}^o = \psi_d^o \qquad \text{for } \vec{\Omega}_d \cdot \vec{n} > 0, \tag{2.51}$$

otherwise

$$\psi_{1d}^e = \psi_{1d}^o = \psi_{2d}^e = \psi_{2d}^o = 0. \tag{2.52}$$

Substitution of Equations (2.40), (2.50) through (2.52) into expression (2.48) yields

$$\int_{\vec{s}} d\vec{s}\{\delta(\underline{\psi}^e)^T|\vec{n}\cdot\vec{\Omega}|\underline{\underline{w}}\,\underline{\psi}^e\}$$

for vacuum boundary surfaces. To obtain the desired form of expression (2.48) for reflected surfaces $\underline{\psi}^o$ is again decomposed

$$\underline{\psi}^o = \underline{\psi}_3^o + \underline{\psi}_4^o$$

where the d^{th} components are defined by

$$\psi^o_{3d} = \psi^o_d \qquad \text{for } d = d \text{ ,}$$

$$\psi^o_{4d} = \psi^o_d \qquad \text{for } d = d^*, \tag{2.53}$$

otherwise

$$\psi^o_{3d} = \psi^o_{4d} = 0. \tag{2.54}$$

Due to symmetry in the Z direction and the symmetric and antisymmetric angular properties of $\underline{\psi}^e$ and $\underline{\psi}^o$ respectively, the angular domain may be restricted such that

$$0 \leq \mu_d \leq 1; \; 0 \leq \gamma_d \leq \pi. \tag{2.55}$$

In view of restriction (2.55) the reflective boundary condition for the discrete odd parity flux becomes for surfaces parallel to the X axis

$$\psi^o_d\Big|_{\vec{s}} = \psi^o_{d^*}\Big|_{\vec{s}} \quad \text{for } \vec{n}\cdot\vec{\Omega}_d = -\vec{n}\cdot\vec{\Omega}^*_d \text{ ,} \tag{2.56}$$

for surfaces parallel to the Y axis

$$\psi^o_d\Big|_{\vec{s}} = -\psi^o_{d^*}\Big|_{\vec{s}} \quad \text{for } \vec{n}\cdot\vec{\Omega}_d = \vec{n}\cdot\vec{\Omega}^*_d \tag{2.57}$$

and for corner points between two adjacent reflected sides

$$\psi^o_d = 0 \qquad \text{for all d.} \tag{2.58}$$

Substitution of Equations (2.53) and (2.54) into expression (2.48) followed by application of the boundary conditions given by Equations (2.56) through (2.58) yields

$$\int_{\vec{s}} ds\{\delta(\underline{\psi}^e)^T \vec{n}\cdot\vec{\underline{\underline{\Omega}}}\ \underline{\underline{w}}\ \underline{\psi}^o\} = 0$$

for reflected surfaces. Thus expression (2.46) may be written

$$\int_{\vec{r}} d\vec{r}\{[\vec{\underline{\underline{\Omega}}}\cdot\vec{\nabla}\ \delta\ \underline{\psi}^e]^T\ \underline{\underline{w}}[\vec{\underline{\underline{\Omega}}}\cdot\vec{\nabla}\ \underline{\psi}^e]/\Sigma +$$

$$\delta(\underline{\psi}^e)^T\ \Sigma\ \underline{\underline{w}}\ \underline{\psi}^e + [\vec{\underline{\underline{\Omega}}}\cdot\vec{\nabla}\ \delta\ \underline{\psi}^e]^T\ \underline{\underline{G}}^o[\vec{\underline{\underline{\Omega}}}\cdot\vec{\nabla}\ \underline{\psi}^e]/\Sigma$$

$$- \delta(\underline{\psi}^e)^T\ \underline{\underline{H}}^e\underline{\psi}^e - [\vec{\underline{\underline{\Omega}}}\cdot\vec{\nabla}\ \delta\ \underline{\psi}^e]^T\ \underline{\underline{G}}^o\ \underline{S}^o/\Sigma$$

$$- [\vec{\underline{\underline{\Omega}}}\cdot\vec{\nabla}\ \delta\ \underline{\psi}^e]^T\ \underline{\underline{w}}\ \underline{S}^o/\Sigma - \delta(\underline{\psi}^e)^T\ \underline{\underline{w}}\ \underline{S}^e\}$$

$$+ \Lambda \int_{\vec{s}} d\vec{s}\{\delta(\underline{\psi}^e)^T|\vec{n}\cdot\vec{\underline{\underline{\Omega}}}|\underline{\underline{w}}\ \underline{\psi}^e\} \qquad (2.59)$$

where $\Lambda = 1$ if $\vec{s}$ corresponds to a vacuum surface, $\Lambda = 0$ if $\vec{s}$ corresponds to a reflected surface.

The definition of the first variation of a functional $F(\underline{\psi})$ is[28]

$$\delta F(\underline{\psi}) \equiv \lim_{\varepsilon\to o} \frac{\partial}{\partial\varepsilon} F(\underline{\psi} + \varepsilon\delta\underline{\psi}). \qquad (2.60)$$

By using this definition together with the symmetry of $\vec{\underline{\underline{\Omega}}}$, $\underline{\underline{w}}$, $\underline{\underline{H}}^e$ and $\underline{\underline{G}}^o$ and expression (2.59), an acceptable reduced functional for $\underline{\psi}^e$ (see Appendix B) may be written

$$F(\underline{\psi}^e) = \frac{1}{2}\int_{\vec{r}} d\vec{r}\{[\underline{\underline{\vec{\Omega}}}\cdot\vec{\nabla}\ \underline{\psi}^e]^T\ \underline{\underline{w}}[\underline{\underline{\vec{\Omega}}}\cdot\vec{\nabla}\ \underline{\psi}^e]/\Sigma$$

$$+ (\underline{\psi}^e)^T\ \Sigma\ \underline{\underline{w}}\ \underline{\psi}^e + [\underline{\underline{\vec{\Omega}}}\cdot\vec{\nabla}\ \underline{\psi}^e]^T\ \underline{\underline{G}}^o[\underline{\underline{\vec{\Omega}}}\cdot\vec{\nabla}\ \underline{\psi}^e]/\Sigma$$

$$- (\underline{\psi}^e)^T\ \underline{\underline{H}}^e\underline{\psi}^e - 2[\underline{\underline{\vec{\Omega}}}\cdot\vec{\nabla}\ \underline{\psi}^e]^T\ \underline{\underline{G}}^o\underline{S}^o/\Sigma$$

$$- 2[\underline{\underline{\vec{\Omega}}}\cdot\vec{\nabla}\ \underline{\psi}^e]^T\ \underline{\underline{w}}\ \underline{S}^o/\Sigma - 2(\psi^e)^T\ \underline{\underline{w}}\ \underline{S}^e\}$$

$$+ \frac{\Lambda}{2}\int_{\vec{s}} d\vec{s}\{(\underline{\psi}^e)^T|\vec{n}\cdot\underline{\underline{\vec{\Omega}}}|\underline{\underline{w}}\ \underline{\psi}^e\}. \qquad (2.61)$$

If Equation (2.39) is multiplied by $\delta(\underline{\psi}^o)^T$ and integrated over $\vec{r}$ and the boundary condition

$$\psi^e_d\Big|_{\vec{s}} = \psi^e_{d^*}\Big|_{\vec{s}} \qquad \text{for all reflected surfaces} \qquad (2.62)$$

is used in place of Equations (2.56) through (2.58), the reduced functional for $\underline{\psi}^o$ is found to be

$$F(\underline{\psi}^o) = \frac{1}{2}\int_{\vec{r}} d\vec{r}\{[\underline{\underline{\vec{\Omega}}}\cdot\vec{\nabla}\ \underline{\psi}^o]^T\ \underline{\underline{w}}[\underline{\underline{\vec{\Omega}}}\cdot\vec{\nabla}\ \underline{\psi}^o]/\Sigma$$

$$+ (\underline{\psi}^o)^T\ \Sigma\ \underline{\underline{w}}\ \underline{\psi}^o + [\underline{\underline{\vec{\Omega}}}\cdot\vec{\nabla}\ \underline{\psi}^o]^T\ \underline{\underline{G}}^e[\underline{\underline{\vec{\Omega}}}\cdot\vec{\nabla}\ \underline{\psi}^o]/\Sigma$$

$$- (\underline{\psi}^o)^T\ \underline{\underline{H}}^o\underline{\psi}^o - 2[\underline{\underline{\vec{\Omega}}}\cdot\vec{\nabla}\ \underline{\psi}^o]^T\ \underline{\underline{G}}^o\ \underline{S}^o/\Sigma$$

$$- 2[\underline{\underline{\vec{\Omega}}}\cdot\vec{\nabla}\ \underline{\psi}^o]^T\ \underline{\underline{w}}\ \underline{S}^e/\Sigma - 2(\underline{\psi}^o)^T\ \underline{\underline{w}}\ \underline{S}^o$$

$$+ \frac{\Lambda}{2}\int_{\vec{s}} d\vec{s}\{(\underline{\psi}^o)^T|\vec{n}\cdot\vec{\Omega}|\underline{\underline{w}}\ \underline{\psi}^o\}. \qquad (2.63)$$

To conclude this section, it is noted that since Equations (2.50) through (2.52) and (2.56) through (2.58) were used to construct the reduced functional $F(\underline{\psi}^e)$, the boundary conditions represented by these equations are natural, whereas the boundary condition represented by Equation (2.62) is essential. Similarly, Equations (2.50) through (2.52) and (2.62) represent natural boundary conditions and Equations (2.56) through (2.58) represent essential boundary conditions of $F(\underline{\psi}^o)$. The natural conditions are automatically imposed on $\underline{\psi}^e$ and $\underline{\psi}^o$ as stationary conditions. In Chapter III, a procedure for imposing the essential conditions will be described.

Finite Element Approximation

To apply the finite element method, the spatial domain of $\underline{\psi}^e$ and $\underline{\psi}^o$, within the even and odd parity functionals, is divided into P contiguous subdomains or elements $\vec{r}_p$. Since the present objective is to treat nonorthogonal geometries, the elements will be chosen to be triangles. Only $F(\underline{\psi}^e)$ will be considered as $F(\underline{\psi}^o)$ is treated in an identical manner. Thus

$$F(\underline{\psi}^e) = \sum_{p=1}^{P} F_p(\underline{\psi}^e) \tag{2.64}$$

where

$$F_p(\underline{\psi}^e) = \frac{1}{2} \int_{\vec{r}_p} d\vec{r} \{ [\underline{\vec{\Omega}} \cdot \vec{\nabla} \, \underline{\psi}^e]^T \, \underline{\underline{w}} [\underline{\vec{\Omega}} \cdot \vec{\nabla} \, \underline{\psi}^e] / \Sigma_p$$

$$+ (\underline{\psi}^e)^T \, \Sigma_p \, \underline{\underline{w}} \, \underline{\psi}^e + [\underline{\vec{\Omega}} \cdot \vec{\nabla} \, \underline{\psi}^e]^T \, \underline{\underline{G}}_p^o \, [\underline{\vec{\Omega}} \cdot \vec{\nabla} \, \underline{\psi}^e] / \Sigma_p$$

$$- (\underline{\psi}^e)^T \underline{\underline{H}}^e_p \underline{\psi}^e - 2[\vec{\underline{\underline{\Omega}}}\cdot\vec{\nabla} \underline{\psi}^e]^T \underline{\underline{G}}^o_p \underline{S}^o/\Sigma_p$$

$$- 2[\vec{\underline{\underline{\Omega}}}\cdot\vec{\nabla} \underline{\psi}^e]^T \underline{\underline{w}} \underline{S}^o/\Sigma_p - 2(\underline{\psi}^e)^T \underline{\underline{w}} \underline{S}^e\}$$

$$+ \frac{\Lambda}{2} \int_{\vec{s}_p} d\vec{s}\{(\underline{\psi}^e)^T|\vec{n}\cdot\vec{\underline{\underline{\Omega}}}|\underline{\underline{w}} \underline{\psi}^e\}. \qquad (2.65)$$

The subscript p on Σ, $\underline{\underline{H}}^e$ and $\underline{\underline{G}}^o$ is used to denote that these quantities are continuous and constant within the p^{th} element. However, they may vary from element to element. In Equation (2.65), $\vec{s}_p$ represents the external surface of the p^{th} element.

Within the p^{th} element, each angular component of $\underline{\psi}^e$ is approximated by a piecewise linear interpolating polynomial of the form

$$\psi^e_d(x,y) = \alpha_1 + \alpha_2 x + \alpha_3 y$$

which may be written

$$\psi^e_d(x,y) = \underline{f}^T(x,y)\ \underline{\alpha} \qquad (2.66)$$

where

$$\underline{f}^T(x,y) = [1\ x\ y] \text{ and } \underline{\alpha} = [\alpha_1\ \alpha_2\ \alpha_3]^T.$$

The arbitrary constants α_i, i = 1, 2, 3, may be obtained by requiring that the interpolating polynomial be satisfied at the three vertices of the p^{th} triangular element. Thus letting

$$\underline{\psi}_d^e = [\psi_d^e(x_1,y_1) \quad \psi_d^e(x_2,y_2) \quad \psi_d^e(x_3,y_3)]^T$$

where the coordinates, (x_i,y_i) i = 1, 2, 3, represent the coordinates of the three vertices of the p^{th} triangular element, allows Equation (2.66) to be written

$$\psi_d^e(x,y) = \underline{L}^T(x,y)\ \underline{\psi}_d^e \ . \tag{2.67}$$

The three components of $\underline{L}^T(x,y)$ are first order or linear Lagrange polynomials defined by

$$L_i(x,y) = (a_i + b_i x + c_i y)/\Delta$$

for i = 1, 2, 3,

where

$$a_1 = x_2y_3 - x_3y_2$$

$$b_1 = y_2 - y_3$$

$$c_1 = x_3 - x_2$$

and $$\Delta = \sum_{i=1}^{3} x_i b_i . \tag{2.68}$$

The other coefficients a_i, b_i, c_i for i = 2, 3 are found by permutting the subscripts on x and y, i.e., 1→2 implies 2→3 and 3→1 etc.

To approximate $\underline{\psi}^e$ in Equation (2.65) it is necessary to introduce a discretized element vector $\underline{\theta}_p$. The q^{th} component of $\underline{\theta}_p$ is simply the component of $\underline{\psi}_d^e$ evaluated at the k^{th} node, i.e.,

$$(\underline{\theta}_p)_q = (\underline{\psi}_d^e)_k$$

where $q = D(k-1)+d$. To obtain a relationship between the vectors $\underline{\psi}^e$ and $\underline{\theta}_p$, the matrix, $\underline{\underline{A}}^p(x,y)$, is defined by

$$(\underline{\underline{A}}^p(x,y))_{k,q} = \sum_{q'=1}^{3} \delta_q^{D(q'-1)+k} \; L_{q'}(x,y)$$

for $k = 1, \ldots, D$; $q = 1, \ldots, 3D$,

where $\delta_i^j = 1$; $i = j$, $\delta_i^j = 0$ otherwise.

Thus

$$\underline{\psi}^e(x,y) = \underline{\underline{A}}^p(x,y)\ \underline{\theta}_p. \tag{2.69}$$

Substitution of Equation (2.69) into (2.65) yields

$$F_p(\psi^e) = \underline{\theta}_p^T\ \underline{\underline{B}}_p^e\ \underline{\theta}_p/2 - \underline{\theta}_p^T\ \underline{C}_p^e \tag{2.70}$$

where

$$\underline{\underline{B}}_p^e = \int_{\vec{r}_p} d\vec{r}\{[\vec{\underline{\underline{\Omega}}}\cdot\vec{\nabla}\ \underline{\underline{A}}^p]^T\ \underline{\underline{w}}[\vec{\underline{\underline{\Omega}}}\cdot\vec{\nabla}\ \underline{\underline{A}}^p]/\Sigma_p$$

$$+ \Sigma_p\ (\underline{\underline{A}}^p)^T\ \underline{\underline{w}}\ \underline{\underline{A}}^p - (\underline{\underline{A}}^p)^T\ \underline{\underline{H}}_p^e\ \underline{\underline{A}}^p +$$

$$[\vec{\underline{\underline{\Omega}}}\cdot\vec{\nabla}\ \underline{\underline{A}}^p]^T\ \underline{\underline{G}}_p^o[\vec{\underline{\underline{\Omega}}}\cdot\vec{\nabla}\ \underline{\underline{A}}^p]/\Sigma_p\} +$$

$$\Lambda \int_{\vec{s}_p} d\vec{s}\{(\underline{\underline{A}}^p)^T|\vec{n}\cdot\vec{\underline{\underline{\Omega}}}|\underline{\underline{w}}\ \underline{\underline{A}}^p\} \tag{2.71}$$

and

$$\underline{C}_p^e = \int_{\vec{r}_p} d\vec{r}\{[\vec{\underline{\Omega}}\cdot\vec{\nabla}\ \underline{\underline{A}}^p]^T\ \underline{\underline{G}}_p^o\ \underline{S}^o/\Sigma_p +$$

$$[\vec{\underline{\Omega}}\cdot\vec{\nabla}\ \underline{\underline{A}}^p]^T\ \underline{\underline{w}}\ \underline{S}^o/\Sigma_p + (\underline{\underline{A}}^p)^T\ \underline{\underline{w}}\ \underline{S}^e\}. \tag{2.72}$$

To ensure spatial continuity of the discrete angular fluxes, the nodal values must be single valued. This requirement is met by using Boolean transformations to express the p^{th} element flux vector $\underline{\theta}_p$ in terms of a single global flux vector $\underline{X}^e$, where the components of $\underline{X}^e$ represent all the global unknowns, i.e., the M×D unknowns where M is the total number of nodes. To obtain the Boolean matrix $\underline{\underline{J}}^p$, it is necessary to introduce the vector $\underline{\beta}^p$ whose q^{th} component is the global number of the q^{th} node of the p^{th} triangle. $\underline{\underline{J}}^p$ may be written

$$(\underline{\underline{J}}^p)_{k,q} = \sum_{k'=1}^{D} \sum_{q'=1}^{3} \delta_k^{D(q'-1)+k'}\ \delta_q^{D(\alpha-1)+k'}$$

for k = 1, ..., 3D; q = 1, ..., M×D

where $\alpha = (\underline{\beta}^p)_{q'}$. Thus

$$\underline{\theta}_p = \underline{\underline{J}}^p\ \underline{X}^e. \tag{2.73}$$

Combining Equations (2.73), (2.70), and (2.64) yields

$$F(\underline{\psi}^e) = (\underline{X}^e)^T \{\sum_{p=1}^{P} (\underline{\underline{J}}^p)^T\ \underline{\underline{B}}_p^e\ \underline{\underline{J}}^p\}\ \underline{X}^e/2$$

$$- (\underline{X}^e)^T \sum_{p=1}^{P} (\underline{\underline{J}}^p)\ \underline{C}_p^e\ .$$

The stationary point of the reduced functional $F(\underline{\psi}^e)$ may now be found by setting its partial derivatives with respect to each component of $\underline{X}^e$ equal to zero. The result is

$$B^e \, X^e = C^e \tag{2.74}$$

where

$$\underline{\underline{B}}^e = \sum_{p=1}^{P} (\underline{\underline{J}}^p)^T \, \underline{\underline{B}}_p^e \, \underline{\underline{J}}^p$$

$$\underline{C}^e = \sum_{p=1}^{P} (\underline{\underline{J}}^p)^T \, \underline{C}_p^e \, . \tag{2.75}$$

In a similar manner, the stationary point of $F(\underline{\psi}^o)$ yields

$$\underline{\underline{B}}^o \, \underline{X}^o = \underline{C}^o \tag{2.76}$$

where $\underline{\underline{B}}^o$ and $\underline{C}^o$ are found from Equation (2.75) by changing the superscript e to o, and where

$$\underline{\underline{B}}_p^o \int_{\vec{r}_p} d\vec{r} \{ [\vec{\underline{\underline{\Omega}}} \cdot \vec{\nabla} \, \underline{\underline{A}}^p]^T \, \underline{\underline{w}} [\vec{\underline{\underline{\Omega}}} \cdot \vec{\nabla} \, \underline{\underline{A}}^p] / \Sigma_p$$

$$+ \Sigma_p \, (\underline{\underline{A}}^p)^T \, \underline{\underline{w}} \, \underline{\underline{A}}^p - (\underline{\underline{A}}^p)^T \, \underline{\underline{H}}_p^o \, \underline{\underline{A}}^p +$$

$$[\vec{\underline{\underline{\Omega}}} \cdot \vec{\nabla} \, \underline{\underline{A}}^p]^T \, \underline{\underline{G}}_p^e [\vec{\underline{\underline{\Omega}}} \cdot \vec{\nabla} \, \underline{\underline{A}}^p] / \Sigma_p \} +$$

$$\Lambda \int_{\vec{s}_p} d\vec{s} \{ (\underline{\underline{A}}^p)^T |\vec{n} \cdot \vec{\underline{\underline{\Omega}}}| \underline{\underline{w}} \, \underline{\underline{A}}^p \} \tag{2.77}$$

and

$$\underline{C}_p^o = \int_{\vec{r}_p} d\vec{r}\{[\vec{\Omega}\cdot\vec{\nabla}\ \underline{\underline{A}}^p]\ \underline{\underline{G}}_p^e\ \underline{S}^e/\Sigma_p +$$

$$[\vec{\Omega}\cdot\vec{\nabla}\ \underline{\underline{A}}^p]^T\ \underline{\underline{w}}\ \underline{S}^e/\Sigma_p + (\underline{\underline{A}}^p)^T\ \underline{\underline{w}}\ \underline{S}^o.$$

If any of the components of $\underline{X}^e$ or $\underline{X}^o$ are specified as essential boundary conditions, these conditions must be imposed on Equations (2.74) and (2.76) as described in Chapter III.

Multigroup Source Approximation

Equations (2.74) and (2.76) represent the necessary coupling algebraic equations for each group discretized even and odd parity fluxes. To obtain multigroup solutions $\underline{C}^e$ and $\underline{C}^o$ must be found since these vectors are coupled to other groups through $\underline{S}^e$ and $\underline{S}^o$. Thus to define the g^{th} group even and odd parity sources, Equation (2.2) is rewritten

$$S_g(\vec{\Omega}) = \sum_{g'=1}^{g-1} \int_{\vec{\Omega}'} \Sigma_{s,g'\to g}(\vec{\Omega}'\cdot\vec{\Omega})\ \phi_{g'}(\vec{\Omega}')\ d\vec{\Omega}'$$

$$+ \frac{\chi_g}{4\pi} \sum_{g'=1}^{G} \nu\Sigma_{fg'} \int_{\vec{\Omega}'} \phi_{g'}(\vec{\Omega}')\ d\vec{\Omega}'$$

$$+ Q_g(\vec{\Omega}).$$

Application of Equation (2.11) yields

$$S_g^e(\vec{\Omega}) = \sum_{g'=1}^{g-1} \int_{\vec{\Omega}'} [\Sigma_{s,g'\to g}(\vec{\Omega}'\cdot\vec{\Omega}) + \Sigma_{s,g'\to g}(\vec{\Omega}'\cdot-\vec{\Omega}]/2$$

$$\times \phi_{g'}(\vec{\Omega}') \, d\vec{\Omega}' +$$

$$\frac{\chi_g}{4\pi} \sum_{g'=1}^{G} \nu\Sigma_{fg'} \int_{\vec{\Omega}'} \psi^e_{g'}(\vec{\Omega}') \, d\vec{\Omega}' +$$

$$[Q_g(\vec{\Omega}) + Q_g(-\vec{\Omega})]/2 \tag{2.78}$$

and

$$S^o_g(\vec{\Omega}) = \sum_{g'=1}^{g-1} \int_{\vec{\Omega}'} [\Sigma_{s,g'\to g}(\vec{\Omega}'\cdot\vec{\Omega}) - \Sigma_{s,g'\to g}(\vec{\Omega}'\cdot-\vec{\Omega})]/2$$

$$\times \phi_{g'}(\vec{\Omega}') \, d\vec{\Omega}' +$$

$$[Q_g(\vec{\Omega}) - Q_g(-\vec{\Omega})]/2. \tag{2.79}$$

Defining even and odd parity extraneous sources as

$$Q^e_g(\vec{\Omega}) = [Q_g(\vec{\Omega}) + Q_g(-\vec{\Omega})]/2,$$

$$Q^o_g(\vec{\Omega}) = [Q_g(\vec{\Omega}) - Q_g(-\vec{\Omega})]/2 \tag{2.80}$$

and utilizing the definition of the even and odd parity cross sections with Equation (2.12), Equations (2.78) and (2.79) may be written

$$S^e_g(\vec{\Omega}) = \sum_{g'=1}^{g-1} \int_{\vec{\Omega}'} \Sigma^e_{s,g'\to g}(\vec{\Omega}'\cdot\vec{\Omega}) \, \psi^e_{g'}(\Omega') \, d\vec{\Omega}'$$

$$+ \frac{\chi_g}{4\pi} \sum_{g'=1}^{G} \nu\Sigma_{fg'} \int_{\vec{\Omega}'} \psi^e_{g'}(\vec{\Omega}') \, d\vec{\Omega}'$$

$$+ Q^e_g(\vec{\Omega}) \tag{2.81}$$

and

$$S_g^o(\vec{\Omega}) = \sum_{g'=1}^{g-1} \int_{\vec{\Omega}'} \Sigma^o_{s,g'\to g}(\vec{\Omega}'\cdot\vec{\Omega})\ \psi^o_{g'}(\vec{\Omega}')\ d\vec{\Omega}'$$

$$+ Q_g^o(\vec{\Omega}). \tag{2.82}$$

The angular discretization of $S_g^e(\vec{\Omega})$ and $S_g^o(\vec{\Omega})$ is accomplished by substituting Equation (2.18) into (2.81) and Equation (2.22) into (2.82) followed by application of the discrete angle approximation procedure described earlier. Thus

$$S^e_{g,d}\ w_d = \sum_{g'=1}^{g-1} \sum_{\ell\ \text{even}} (2\ell+1)\ \Sigma_{s\ell,g'\to g} \sum_{m=0}^{\ell} w_d\ R^m_{\ell,d}$$

$$\times \sum_{d'=1}^{D} R^m_{\ell,d'}\ \psi^e_{g'd'}\ w_{d'} +$$

$$\chi_g \sum_{g'=1}^{G} \nu\Sigma_{fg'}\ w_d \sum_{d'=1}^{D} \psi^e_{g',d'}\ w_{d'} + Q^e_{g,d}\ w_d \tag{2.83}$$

and

$$S^o_{g,d}\ w_d = \sum_{g'=1}^{g-1} \sum_{\ell\ \text{odd}} (2\ell+1)\ \Sigma_{s\ell,g'\to g} \sum_{m=0}^{\ell} w_d\ R^m_{\ell,d}$$

$$\times \sum_{d'=1}^{D} R^m_{\ell,d'}\ \psi^o_{g'd'}\ w_{d'} + Q^o_{g,d}\ w_d. \tag{2.84}$$

By defining the following matrix

$$\underline{\underline{E}} \equiv \begin{pmatrix} w_1 w_1 & \cdots & w_1 w_D \\ & & \\ w_D w_1 & \cdots & w_D w_D \end{pmatrix}$$

and vectors

$$\underline{Q}_g^e \equiv \begin{pmatrix} Q_{g,1}^e \\ \vdots \\ Q_{g,d}^e \end{pmatrix} ; \qquad \underline{Q}_g^o \equiv \begin{pmatrix} Q_{g,1}^o \\ \vdots \\ Q_{g,D}^o \end{pmatrix}$$

Equations (2.83) and (2.84) may be written in matrix form as

$$\underline{\underline{w}}\, \underline{S}_g^e = \sum_{g'=1}^{g-1} \underline{\underline{H}}_{g' \to g}^e \, \underline{\psi}_{g'}^e$$

$$+ \chi_g \sum_{g'=1}^{G} \nu\Sigma_{fg'} \, \underline{\underline{E}} \, \underline{\psi}_{g'}^e + \underline{\underline{w}}\, \underline{Q}_g^e \qquad (2.85)$$

and

$$\underline{\underline{w}}\, \underline{S}_g^o = \sum_{g'=1}^{g-1} \underline{\underline{H}}_{g' \to g}^o \, \underline{\psi}_{g'}^o + \underline{\underline{w}}\, \underline{Q}_g^o \, . \qquad (2.86)$$

The matrices $\underline{\underline{H}}_{g' \to g}^e$ and $\underline{\underline{H}}_{g' \to g}^o$ are obtained by replacing $\Sigma_{s\ell}$ by $\Sigma_{s\ell, g' \to g}$ in the definitions of $\underline{\underline{H}}^e$ and $\underline{\underline{H}}^o$, respectively. It is assumed that $\underline{\psi}_{g'}^e$ and $\underline{\psi}_{g'}^o$ are known from a previous calculation. Thus Equations (2.85) and (2.86) may be used to obtain $\underline{S}^e$ and $\underline{S}^o$ which in turn allow the element vectors $\underline{C}_p^e$ and $\underline{C}_p^o$ to be constructed.

CHAPTER III

SOLUTION TECHNIQUES

In the previous chapter, a discrete angle approximation and a finite element approximation were employed to transform Equation (2.1) into two sets of algebraic equations, i.e., Equations (2.74) and (2.76). To obtain a compatible form, the multigroup source, $S_g(x,y,\vec{\Omega})$, was transformed and similarly discretized in angle. The purpose of this chapter is to describe in detail the solution techniques required to numerically solve these equations.

The System Equations

To construct the system equations, i.e., Equations (2.74) and (2.76), it is first necessary to evaluate the element matrices $\underline{\underline{B}}_p^e$ and $\underline{\underline{B}}_p^o$ and element vectors $\underline{C}_p^e$ and $\underline{C}_p^o$. The surface integral in Equations (2.71) and (2.77) may be evaluated by introducing Figure 2 (also see Figure 1 on page 19) and the addition theorem[25]

$$|\cos \varepsilon| = |\cos \theta_d \cos \theta' + \sin \theta_d \sin \theta' \cos (\gamma_d - \gamma')| \qquad (3.1)$$

where ε is the angle between $\vec{n}$ and $\vec{\Omega}_d$, i.e., $\cos \varepsilon = \vec{n} \cdot \vec{\Omega}_d$. Since the triangle lies in the x-y plane, the outward normal $\vec{n}$ of the vacuum boundary surface also lies in the x-y plane. Thus $\gamma' = 0$ and Equation (3.1) reduces to

$$|\cos \varepsilon| = |\cos \theta_d \cos \theta' + \sin \theta_d \sin \theta' \cos \gamma_d|. \qquad (3.2)$$

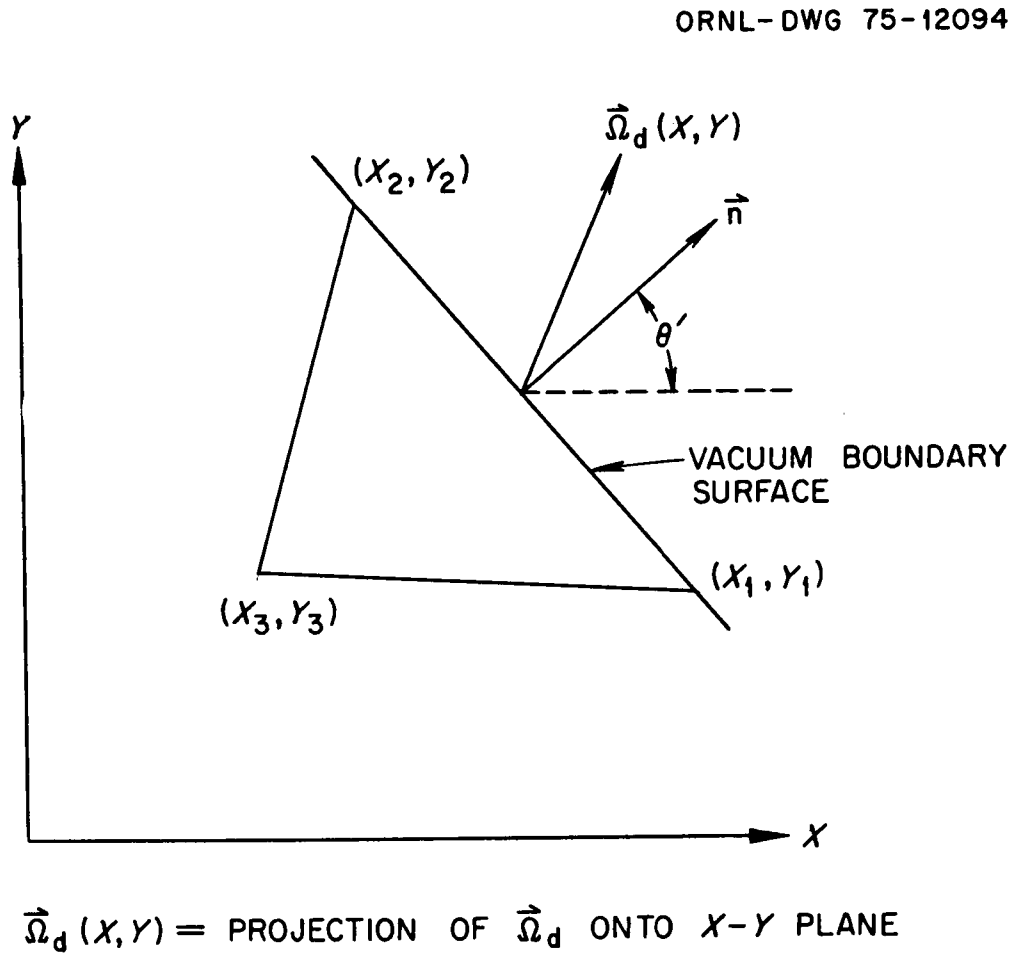


Figure 2. Representation of vacuum boundary surface for a typical triangle.

Utilizing the definitions of μ and η (see Figure 1 on page 19) yields

$$|\vec{n}\cdot\vec{\Omega}_d| = |\mu_d \cos\theta' + \eta_d \sin\theta'|. \tag{3.3}$$

If L represents the length of the surface, i.e.

$$L = [(x_2 - x_1)^2 + (y_2 - y_1)^2]^{1/2}$$

Equation (3.3) becomes

$$|\vec{n}\cdot\vec{\Omega}_d| = |(y_1 - y_2)\,\mu_d + (x_2 - x_1)\,\eta_d|/L.$$

Consider next that y along the surface is given by

$$y = (x - x_1)\,(y_2 - y_1)/(x_2 - x_1) + y_1$$

which when substituted into Equation (2.68) yields

$$L_1(x,y) = (x_2 - x)/(x_2 - x_1)$$

$$L_2(x,y) = (x - x_1)/(x_2 - x_1)$$

$$L_3(x,y) = 0. \tag{3.4}$$

Substitution of Equations (2.68) and (3.4) into (2.71) allows the kq^{th} term of $\underline{\underline{B}}^e_p$ to be written

$$(\underline{\underline{B}}^e_p)_{kq} = \{[(\mu_d b_i + \eta_d c_i)\,(\underline{\underline{w}})_{dd'}\,(\mu_d\, b_j + \eta_d\, c_j)/\Sigma_p$$

$$+ \Sigma_p\,(\underline{\underline{w}})_{dd'} N_i^j]\delta_d^{d'} - N_i^j(\underline{\underline{H}}^e_p)_{dd'} +$$

$$(\mu_d b_i + \eta_d c_i)\ (\underline{\underline{G}}^{o}_{p})_{dd'}\ (\mu_{d'} b_j + \eta_{d'} c_j)/\Sigma_p\}/2\Delta$$

$$+ \Lambda|\mu_d(y_1 - y_2) + \eta_d(x_2 - x_1)|$$

$$\times\ (\underline{\underline{w}})_{dd'}\ \delta_d^{d'}(1 - \delta_3^i)\ (1 - \delta_3^j)\ (1 + \delta_i^j)/6$$

where $k = D(i - 1) + d$ for $i = 1, 2, 3$; $d = 1, \ldots, D$

and $q = D(j - 1) + d'$ for $j = 1, 2, 3$; $d' = 1, \ldots, D$. (3.5)

The term N_i^j is defined by

$$N_i^j = a_i a_j + (a_i b_j + a_j b_i)\ \bar{x} +$$

$$(a_i c_j + a_j c_i)\ \bar{y} + b_i b_j(\bar{a} + \bar{x}^2) +$$

$$(b_i c_j + b_j c_i)\ (\bar{c} + \bar{x}\bar{y}) + c_i c_j(\bar{b} + \bar{y}^2)$$

where

$$\bar{x} = (x_1 + x_2 + x_3)/3,\ \bar{y} = (y_1 + y_2 + y_3)/3,$$

$$\bar{a} = \sum_{i=1}^{3} (x_i - \bar{x})^2/12,$$

$$\bar{b} = \sum_{i=1}^{3} (y_i - \bar{y})^2/12$$

and

$$\bar{c} = \sum_{i=1}^{3} (x_i - \bar{x})\ (y_i - \bar{y}). \qquad (3.6)$$

In obtaining Equation (3.5), it was assumed that the first and second nodes of a triangle define the ends of the vacuum surface side. If this is not the case, then the final term in Equation (3.5) is changed accordingly. In a similar manner $\underline{\underline{B}}_p^o$ may be evaluated to give

$$(\underline{\underline{B}}_p^o)_{kg} = \{[(\mu_d b_i + \eta_d c_i)\ (\underline{\underline{w}})_{dd'}\ (\mu_{d'} b_j + \eta_{d'} c_j)/\Sigma_p$$

$$+ \Sigma_p\ (\underline{\underline{w}})_{dd'}\ N_i^j]\ \delta_d^{d'} - N_i^j (\underline{\underline{H}}_p^o)_{dd'} +$$

$$(\mu_d b_i + \eta_d c_i)\ (\underline{\underline{G}}_p^e)_{dd'}\ (\mu_{d'} b_j + \eta_{d'} c_j)/\Sigma_p\}/2\Delta$$

$$+ \Lambda|\mu_d(y_1 - y_2) + \eta_d(x_2 - x_1)|$$

$$\times\ (\underline{\underline{w}})_{dd'}\ \delta_d^{d'}\ (1 - \delta_3^i)\ (1 - \delta_3^j)\ (1 + \delta_i^j)/6$$

where $k = D(i - 1) + d$ for $i = 1, 2, 3$; $d = 1, \ldots, D$

and $q = D(j - 1) + d'$ for $j = 1, 2, 3$; $d' = 1, \ldots, D$. (3.7)

To evaluate the element vectors $\underline{C}_p^e$ and $\underline{C}_p^o$, it is necessary to determine a procedure capable of approximating the spatial dependence of $\psi_{g'}^e$ and $\psi_{g'}^o$. The most common procedure is to use Equation (2.69) for each g' group. However, this approach requires the generation of a large number of matrices which are equal in size to the system matrices $\underline{\underline{B}}^e$ and $\underline{\underline{B}}^o$. Although alternate procedures have been employed in diffusion calculations,[6] the easiest and most straightforward to implement is obtained by utilizing element averaged fluxes. These fluxes are found by integrating Equation (2.67) over each triangle and dividing by the triangle area. Thus

$$\bar{\psi}_d^e \cong (2 \int_{\vec{r}_p} \underline{L}^T(x,y)\ \underline{\psi}_d^e\ d\vec{r})/\Delta,$$

or

$$\bar{\psi}_{d,g',p}^e \cong \sum_{i=1}^{3} \psi_{d,g',i}^e/3,$$

and

$$\bar{\psi}_{d,g',p}^o \cong \sum_{i=1}^{3} \psi_{d,g',i}^o/3$$

for all g' and d. (3.8)

Substitution of Equations (3.8) for each component of $\underline{\psi}_{g'}^e$ and $\underline{\psi}_{g'}^o$ in Equations (2.85) and (2.86) yields spatially averaged even and odd parity source vectors which are constant within each triangle. Replacing $\underline{S}^e$ and $\underline{S}^o$ in Equation (2.72) by $\underline{S}_p^e$ and $\underline{S}_p^o$ yields

$$(\underline{C}_p^e)_k = \frac{1}{2} \{ \sum_{d'=1}^{D} (\mu_d b_i + \eta_d c_i)\ (\underline{\underline{G}}_p^o)_{dd'}\ (\underline{S}_p^o)_{d'}/\Sigma_p$$

$$+ (\mu_d b_i + \eta_d c_i)\ (\underline{\underline{W}})_{dd}\ (\underline{S}_p^e)_d/\Sigma_p \}$$

$$+ (\underline{\underline{W}})_{dd}\ (\underline{S}_p^o)_d\ \Delta/6$$

where $k = D(i - 1) + d$ for $i = 1, 2, 3$; $d = 1, \ldots, D$. (3.9)

Similarly,

$$(\underline{C}_p^o)_k = \frac{1}{2} \{ \sum_{d'=1}^{D} (\mu_d b_i + \eta_d b_i)(\underline{\underline{G}}_p^e)_{dd'}\ (\underline{S}_p^e)_{d'}/\Sigma_p$$

$$+ (\mu_d b_i + \eta_d c_i)\ (\underline{\underline{w}})_{dd}\ (\underline{S}_p^e)_d/\Sigma_p\}$$

$$+ (\underline{\underline{w}})_{dd}\ (\underline{S}_p^o)_d\ \Delta/6$$

Where $k = D(i - 1) + d$ for $i = 1, 2, 3$; $d = 1, \ldots, D$. (3.10)

The construction of the system matrices, $\underline{\underline{B}}^e$ and $\underline{\underline{B}}^o$ can now be accomplished by substituting Equations (3.5) and (3.7) into Equation (2.75). However, to utilize Equation (2.75), the Boolean transformation matrices which are very large would have to be calculated. Since these matrices only contain zeros and ones the product $(\underline{\underline{J}}^p)^T\ \underline{\underline{B}}_p^e\ \underline{\underline{J}}^p$ simply adds entries of $\underline{\underline{B}}_p^e$ into the proper locations in $\underline{\underline{B}}^e$. An alternate and numerically much more efficient approach is to calculate directly[29] the proper locations in $\underline{\underline{B}}^e$. This can be easily accomplished by replacing i and j in the subscript definitions of Equation (3.5) by $(\underline{\beta}^p)_i$ and $(\underline{\beta}^p)_j$ respectively where $\underline{\beta}^p$ was introduced in the previous chapter. That is, the kq^{th} entry of $\underline{\underline{B}}_p^e$ adds to the $k'q'^{th}$ location in $\underline{\underline{B}}^e$ where

$$k' = D[(\underline{\beta}^p)_i - 1] + d,$$

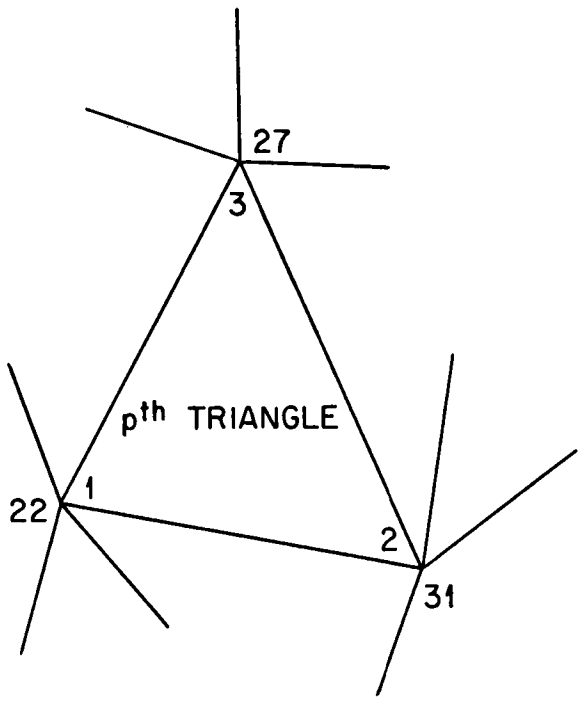
$$q' = D[(\underline{\beta}^p)_j - 1] + d' \quad (3.11)$$

when $k = D(i - 1) + d$; $q = D(j - 1) + d'$. (3.12)

To illustrate this procedure, consider Figure 3. For the triangle shown $\underline{\beta}^p$ is given by

$$\underline{\beta}^p = [22\ 31\ 27]^T. \quad (3.13)$$

ORNL-DWG 75-12095



1, 2, AND 3 SIGNIFY THE THREE NODES OF THE p^{th} TRIANGLE

22, 31, AND 27 REPRESENT THE CORRESPONDING GLOBAL NODE NUMBERS

Figure 3. Representation of local and global node numbering schemes for a typical triangle.

Suppose for a given problem, the number of discrete angles is six, i.e., D = 6. If i = 1, j = 3, d = 2, and d′ = 5, Equation (3.12) yields k = 2 and q = 17. Thus these values of i, j, d, and d′ generate the term in the second row and seventeenth column of the even parity element matrix $\underline{\underline{B}}_p^e$. Substitution of these values of i, j, d, and d′ into Equation (3.11) and using Equation (3.13) yields k′ = 128 and q′ = 161. Consequently, for the triangle shown in Figure 3, the term in the second row and seventeenth column of its element matrix adds to the term in the 128th row and 161st column of the system matrix $\underline{\underline{B}}^e$. Applying this procedure to all the element matrices thus constructs the system matrices. In a similar manner, the system vectors can be readily constructed from the element vectors.

As noted earlier, the variational formulation generates symmetric system matrices. This is easily seen by replacing i by j, j by i, d by d′ and d′ by d in Equations (3.5) and (3.7). Consequently in practice, the assemblying procedure is performed only when $q' \geq k'$ in Equation (3.11). In addition, the system matrices are banded since a given node can couple directly only with its nearest neighbors. Thus, storage requirements for numerical calculations are substantially reduced if the system matrices are stored as MD × IBW dimensional rectangular arrays. The half-band width of each matrix, IBW is calculated from

$$IBW = D \max_{\text{all } p} \left| (\underline{\beta}^p)_i - (\underline{\beta}^p)_j + 1 \right|$$

for i = 1, 2, 3; j = 1, 2, 3.

The correspondence between the compacted array locations and original system matrix is obtained from

$$(\underline{\underline{B}}^e)_{k'q'} \text{ compact} = (\underline{\beta}^e)_{kq}$$

where $k' = k$, $q' = q - k + 1$

for $k = 1, \ldots, MD$; $q = 1, \ldots, IBW$.

Application of Boundary Constraints

The essential boundary conditions arising from spectral reflection, i.e., Equation (2.62) for $\underline{\psi}^e$ and Equations (2.56) through (2.58) for $\underline{\psi}^o$, must be imposed on the system equations. A commonly used procedure is to equate the particular discrete fluxes at the appropriate boundary nodes and then eliminate these dependent unknowns by collapsing the system equations.[6,9,12] However, a procedure which maintains the symmetric properties of the system matrices was employed in this work. The purpose of this section is to describe this symmetric modification procedure.

In general, essential boundary conditions constrain unknowns at appropriate boundary nodes. Coupling between unknowns at different nodes does not normally occur because it is a result of higher-order coupling, and in variational formulations higher-order boundary conditions are almost always natural. Thus, the D discrete angle even or odd parity fluxes at each boundary node can be constrained as

$$a_1 \theta_{1i} + a_2 \theta_{2i} + \ldots + a_j \theta_{ji} + \ldots a_D \theta_{Di} = b \qquad (3.14)$$

where i signifies the i^{th} node on the p^{th} element and some of the a's may be zero. Equation (3.14) may be rewritten

$$(\underline{a}_L)^T \underline{\theta}^i = b \tag{3.15}$$

where

$$(\underline{a}_L)^T = [a_1 \; a_2 \; \cdots \; a_D]$$

$$\underline{\theta}^i = [\theta_{1i} \; \theta_{2i} \; \cdots \; \theta_{Di}]^T.$$

Defining the Boolean transformation matrix $\underline{\underline{J}}$ as

$$(\underline{\underline{J}})_{kq} = \sum_{k'=1}^{D} \delta_k^{D(i-1)+k'} \; \delta_q^{D(\alpha-1)+k'}$$

for k = 1, ..., D; q = 1, ..., MxD

and $\alpha = (\underline{\beta}^p)_i$

allows $\underline{\theta}^i$ to be written in terms of the global unknown vector $\underline{X}$, i.e.,

$$\underline{\theta}^i = \underline{\underline{J}} \; \underline{X}. \tag{3.16}$$

Combining Equations (3.15) and (3.16) yields

$$(\underline{a})^T \underline{X} = b \tag{3.17}$$

where the global constraint vector $(\underline{a})^T$ is defined by

$$(\underline{a})^T = (\underline{a}_L)^T \underline{\underline{J}}.$$

The dependent unknown in Equation (3.17) is determined by hunting the term in $(\underline{a})^T$ having the largest absolute value, i.e., let $(\underline{X})_j$ be the dependent unknown subject to the criteria

$$|(\underline{a})_j| \geq |(\underline{a})_q|$$

for $q = 1, \ldots, M \times D$; $q \neq j$.

Thus solving Equation (3.17) for $(\underline{X})_j$ yields

$$(\underline{X})_j = [b - (\bar{\underline{a}})^T \underline{X}]/(\underline{a})_j \tag{3.18}$$

where $(\bar{\underline{a}})^T = (\underline{a})^T$ with $(\underline{a})_j^T$ set equal to zero. Letting

$$S = b/(\underline{a})_j$$

and

$$(\underline{F})^T = (\bar{\underline{a}})^T/(\underline{a})_j$$

yields for Equation (3.18)

$$(\underline{X})_j = S - (\underline{F})^T \underline{X}. \tag{3.19}$$

Substitution of Equation (3.19) into either Equation (2.74) or (2.76), i.e., the system equations with the superscripts removed,

$$\underline{\underline{B}}\ \underline{X} = \underline{C},$$

yields

$$\underline{\underline{B}}'\ \underline{X} = \underline{C}'$$

where the modified system matrix $\underline{\underline{B}}'$ and modified system vector $\underline{C}'$ are defined by

$$(\underline{\underline{B}}')_{kq} = [(\underline{\underline{B}})_{kq} - (\underline{F}^T)_q \, (\underline{\underline{B}})_{kj}] \, (1 - \delta_q^j) \tag{3.20}$$

for all k and q,

$$(\underline{C}')_k = (\underline{C})_k - S(\underline{\underline{B}})_{kj} \tag{3.21}$$

for all k.

Since these modifications to the system matrix destroy its symmetric properties, additional modifications are required to restore symmetry. These additional modifications which can be performed by adding and subtracting equations result in

$$\underline{\underline{B}}^* \, \underline{X} = \underline{C}^* \tag{3.22}$$

where

$$(\underline{\underline{B}}^*)_{kq} = [(\underline{\underline{B}}')_{kq} - (\underline{F}^T)_q \, (\underline{\underline{B}}')_{jk}] \, [1 - \delta_k^j] \tag{3.23}$$

for all k and q,

$$(\underline{C}^*)_j = 0. \tag{3.24}$$

The new system matrix $\underline{\underline{B}}^*$ is singular since its j^{th} row and column have essentially been eliminated. To overcome the singular nature of $\underline{\underline{B}}^*$, a symmetric form of the constraint equation is added to the system equations. The symmetric form is obtained by dividing Equation (3.17) by $(\underline{a})_j$ to give

$$(\underline{a}^*)^T \underline{X} = b^* \tag{3.25}$$

where $(\underline{a}^*)_k = (\underline{a})_k/(\underline{a})_j$ for all k

and $b^* = b/(\underline{a})_j$.

Multiplying Equation (3.25) by $\underline{a}^*$ yields

$$\underline{\underline{A}}^* \underline{X} = \underline{E}^* \tag{3.26}$$

where $\underline{\underline{A}}^* = \underline{a}^*(\underline{a}^*)^T$, and $\underline{E}^* = \underline{a}^* b^*$.

In addition to being symmetric, $\underline{\underline{A}}^*$ is also diagonally dominant due to the choice of $(\underline{a})_j$. Adding Equations (3.22) and (3.26) yields the final form of the system equations, i.e.,

$$\underline{\underline{B}}^N X = C^N \tag{3.27}$$

where

$$(\underline{\underline{B}}^N)_{kq} = (\underline{\underline{B}}^*)_{kq} + (\underline{\underline{A}}^*)_{kq} \tag{3.28}$$

for all k and q, and

$$(C^N)_k = (C^*)_k + (E^*)_k \tag{3.29}$$

for all k.

The new system matrix $\underline{\underline{B}}^N$ is symmetric and banded as was $\underline{\underline{B}}$. Unfortunately, the bandwidth of $\underline{\underline{B}}^N$ is greater than the bandwidth of $\underline{\underline{B}}$ due to the modifications. The increase in bandwidth due to the essential boundary conditions considered in this work is given by

$$IBW^N - IBW = \max_{d,d^*} |d-d^*| . \tag{3.30}$$

The indices d and d* represent a forward discrete angle and its corresponding reflected discrete angle respectively. Thus to minimize Equation (3.30) the discrete angles are ordered differently than in general discrete quadrature sets, i.e.,

$$d^* = d + 1 \text{ for } d \text{ odd.}$$

The ordering used in this work is illustrated in Figure 4 for D = 12. This ordering yields from Equation (3.30)

$$IBW^N = IBW + 1.$$

Modified Cholesky Algorithm

Equation (3.27) represents a set of linear algebraic equations. Assuming that $\underline{\underline{B}}^N$ is nonsingular, the solution to this set of equations may be written

$$\underline{X} = (\underline{\underline{B}}^N)^{-1} \underline{C}^N \tag{3.31}$$

where the superscript -1 is introduced to denote inverse. The purpose of this section is to describe a method which takes advantage of the banded symmetric nature of $\underline{\underline{B}}^N$ to obtain $(\underline{\underline{B}}^N)^{-1}$. The main feature of the method is the decomposition of $\underline{\underline{B}}^N$ into an upper and a unit lower triangular matrix as

$$\underline{\underline{B}}^N = \underline{\underline{L}}\ \underline{\underline{U}}(1) \tag{3.32}$$

where $\underline{\underline{L}}$ is a lower triangular matrix, i.e., $L_{ij} = 0$ for $i > j$, and $\underline{\underline{U}}(1)$ is a unit upper triangular matrix, i.e., $U_{ij} = 0$ for $j > i$, $U_{ii} = 1$.

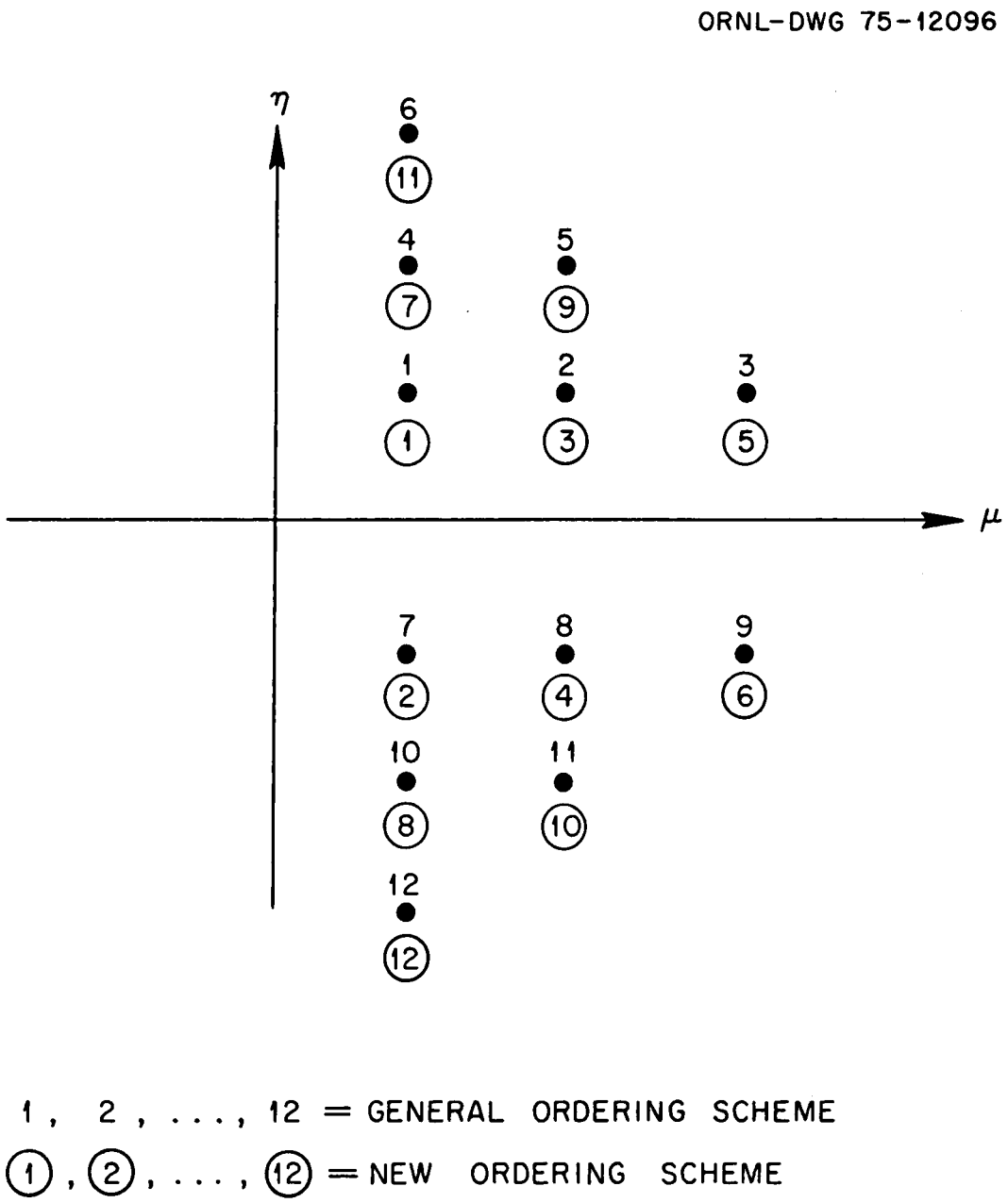


Figure 4. Representation of discrete angle ordering schemes.

The decomposition represented by Equation (3.32) is regarded as the Cholesky-Turing Method.[30]

Since $\underline{\underline{B}}^N$ is symmetric, Equation (3.32) may be written

$$\underline{\underline{B}}^B = \tilde{\underline{\underline{L}}}\,\tilde{\underline{\underline{L}}}^T. \tag{3.33}$$

Equation (3.33) is normally referred to as the standard Cholesky composition.[29] The matrix $\tilde{\underline{\underline{L}}}$ however, is not necessarily real, nor are its elements necessarily unique since the diagonal elements are obtained by performing a square root operation. Thus, the standard Cholesky algorithm is normally avoided by rewriting Equation (3.33) as

$$\underline{\underline{B}}^N + \underline{\underline{L}}(1)\ \underline{\underline{D}}\ [\underline{\underline{L}}(1)]^T \tag{3.34}$$

where $\underline{\underline{D}}$ is a diagonal matrix.

Substituting Equation (3.34) into Equation (3.27) yields

$$\underline{\underline{L}}(1)\ \underline{\underline{D}}[\underline{\underline{L}}(1)]^T\ \underline{X} = \underline{C}^N. \tag{3.35}$$

Once $\underline{\underline{L}}(1)$ and $\underline{\underline{D}}$ have been obtained, Equation (3.35) may be solved in three steps. In the first $\underline{Y}$ is defined by

$$\underline{Y} = \underline{\underline{D}}[\underline{\underline{L}}(1)]^T\ \underline{X}, \tag{3.36}$$

thus from (3.35)

$$\underline{Y} = [\underline{\underline{L}}(1)]^{-1}\ \underline{C}^N \tag{3.37}$$

which simply requires a forward substitution. In the second step $\underline{Z}$ is defined by

$$\underline{Z} = [\underline{\underline{L}}(1)]^T \underline{X}, \tag{3.38}$$

thus from (3.36)

$$\underline{Z} = \underline{\underline{D}}^{-1} \underline{Y} \tag{3.39}$$

which only requires each component of $\underline{Y}$ to be divided by an element of $\underline{\underline{D}}$ since $\underline{\underline{D}}$ is diagonal. Finally from (3.38)

$$\underline{X} = ([\underline{\underline{L}}(1)]^T)^{-1} \underline{Z} \tag{3.40}$$

which is a simple back substitution. Thus, the procedure to solve Equation (3.27) consists of applying sequentially Equations (3.37), (3.39), and (3.40) rather than Equation (3.31).

If Equation (3.27) is to be solved many times, as in the multigroup scheme described in the next section, a numerically more efficient solution algorithm is obtained by decomposing $\underline{\underline{B}}^N$ as[31]

$$\underline{\underline{B}}^N = \underline{\underline{L}}(1)\ \underline{\underline{D}}^{-1}\ [\underline{\underline{L}}(1)]^T. \tag{3.41}$$

This is due to the fact that $\underline{\underline{B}}^N$ only needs to be decomposed once for each even and odd parity flux group whereas Equation (3.39) needs to be applied each time new source vectors are obtained. Using Equation (3.41) allows Equation (3.39) to be written

$$\underline{Z} = \underline{\underline{D}}\ \underline{Y}. \tag{3.42}$$

To obtain the decomposed matrices, each term in $\underline{\underline{B}}^N$ is equated to its corresponding term in $\underline{\underline{L}}(1)\ \underline{\underline{D}}^{-1}\ [\underline{\underline{L}}(1)]^T$. Since $\underline{\underline{B}}^N$ is symmetric, only

the upper triangonal of $\underline{\underline{B}}^N$ is considered. Beginning with the first row gives

$$(\underline{\underline{D}})_{11} = 1/(\underline{\underline{B}}^N)_{11}$$

$$([\underline{\underline{L}}(1)]^T)_{1j} = (\underline{\underline{D}})_{11}\ (\underline{\underline{B}}^N)_{1j}$$

$$\text{for } j = 2, \text{IBW}. \tag{3.43}$$

The remaining rows yield

$$(\underline{\underline{D}})_{ii} = [(\underline{\underline{B}}^N)_{ii} - \sum_{r=1}^{i-1} ([\underline{\underline{L}}(1)]^T)^2_{ri}/(\underline{\underline{D}})_{rr}]^{-1}$$

and

$$([\underline{\underline{L}}(1)]^T)_{ij} = \{(\underline{\underline{B}}^N)_{ij} -$$

$$\sum_{r=1}^{i-1} ([\underline{\underline{L}}(1)]^T)_{ri}\ ([\underline{\underline{L}}(1)]^T)_{rj}/(\underline{\underline{D}})_{rr}\}\ (\underline{\underline{D}})_{ii}$$

$$\text{for } i = 2, \ldots, \text{MD};\ j = i + 1, \ldots, i - 1 + \text{IBW}. \tag{3.44}$$

The modified Cholesky algorithm used in this work thus consists of using Equations (3.43) and (3.44) to obtain the decomposed form of the system matrices followed by the sequential application of Equations (3.37), (3.42), and (3.40). To conserve computer storage, the matrix $\underline{\underline{D}}$ is stored over the diagonal of $\underline{\underline{B}}^N$ and all but the diagonal of $[\underline{\underline{L}}(1)]^T$ is stored in compacted form over the upper triangular compacted form of $\underline{\underline{B}}^N$.

Outer Iteration Scheme

In this section, the finite element formulation developed in Chapter II and the solution techniques described previously in this chapter are unified in the context of a multigroup outer iteration scheme. To begin Equations (2.83) and (2.84) are rewritten using the definition of the element averaged fluxes, i.e., Equation (3.8) for each element as

$$S^{e}_{g,d,p} = DS^{e}_{g,d,p} + F_{g,p} + Q^{e}_{g,d,p} \tag{3.45}$$

and

$$S^{o}_{g,d,p} = DS^{o}_{g,d,p} + Q^{o}_{g,d,p} \tag{3.46}$$

where

$$DS^{e}_{g,d,p} = \sum_{g'=1}^{g-1} \sum_{\ell \text{ even}} (2\ell+1)\, \Sigma_{s\ell,g'\to g} \sum_{m=0}^{\ell} R^{m}_{\ell,D}$$

$$\times \sum_{d'=1}^{D} R^{m}_{\ell,d'}\, \bar{\psi}^{e}_{g',d',p} w_{d'},$$

$$DS^{o}_{g,d,p} = \sum_{g'=1}^{g-1} \sum_{\ell \text{ odd}} (2\ell+1)\, \Sigma_{s\ell,g'\to g} \sum_{m=0}^{\ell} R^{m}_{\ell,d}$$

$$\times \sum_{d'=1}^{D} R^{m}_{\ell,d'}\, \bar{\psi}^{o}_{g',d',p}\, w_{d'}$$

and

$$F_{g,p} = \chi_{g} \sum_{g'=1}^{G} \nu\Sigma_{fg'} \sum_{d'=1}^{D} \bar{\psi}^{e}_{g',d',p}\, w_{d'}.$$

By introducing an element averaged group scalar flux, $\phi_{g,p}$, defined by

$$\phi_{g',p} = \sum_{d'=1}^{D} \bar{\psi}^{e}_{g',d',p} \, w_{d'} \tag{3.47}$$

a total fission source for each element may be written

$$F_{p}^{TOT} = \sum_{g'=1}^{G} \nu\Sigma_{fg'} \, \phi_{g',p}. \tag{3.48}$$

Each group fission source is thus

$$F_{g,p} = \chi_{g} \, F_{p}^{TOT}.$$

The outer iteration scheme employed in this work consists of assuming a total fission source distribution, i.e., the F_{p}^{TOT}'s followed by sequential sweeps of the energy groups beginning with the highest energy group. As each group is encountered both the even and odd parity system equations are constructed. After imposing essential boundary conditions, the modified Cholesky algorithm is employed to perform the matrix decompositions. The group discrete even and odd parity fluxes are then obtained by the forward and back substitution procedure described in the previous section. The following group downscatter sources are computed using the most recently calculated higher group fluxes. One downward sweep through all the groups is termed an outer iteration.

In succeeding outer iterations, only the group system source vectors need be recomputed since the system matrices are iteration

independent. Essential boundary conditions are imposed on the newly computed source vectors and the decomposed first iteration matrices are used to calculate the new fluxes. After each iteration, the total fission source distribution is recomputed to begin the next iteration. Calculations are terminated when the maximum fractional change (over all energy groups and spatial elements) between two successive iterative values of the element averaged group scalar fluxes is sufficiently "small," i.e.,

$$\max_{g,p} \left| (\phi^{t}_{g,p} - \phi^{t-1}_{g,p})/\phi^{t}_{g,p} \right| \leq \varepsilon \tag{3.49}$$

where t represents the iteration number and ε is typically 10^{-2} to 10^{-4}.

The flow diagrams depicted in Figures 5 and 6 present a more detailed description of the outer iteration scheme. The parenthesized numbers appearing in some of the blocks represent the primary equations (as numbered in the text) which are employed during a calculation. The important point to note is that during each group calculation, both the even and odd parity system equations, i.e., Equations (2.74) and (2.76) are solved. An alternate approach is to employ the auxillary equations, i.e., Equations (2.33) and (2.36) in place of the odd and even parity system equations, respectively.

To obtain a working form of these equations, Equation (2.67) is substituted into Equations (2.33) and (2.36). The resulting equations when written out explicitly are

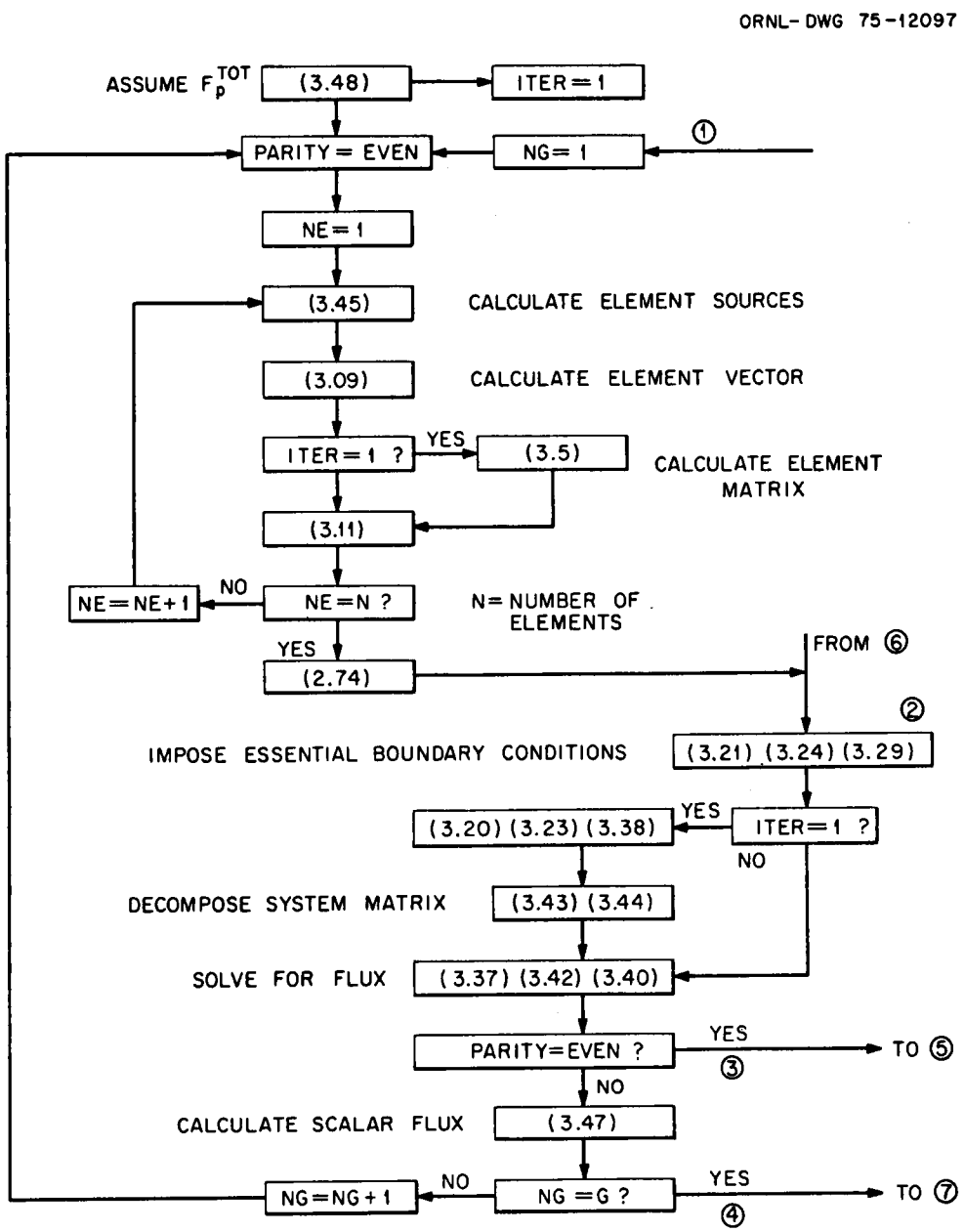


Figure 5. Flow diagram for even parity flux calculation and multigroup scheme.

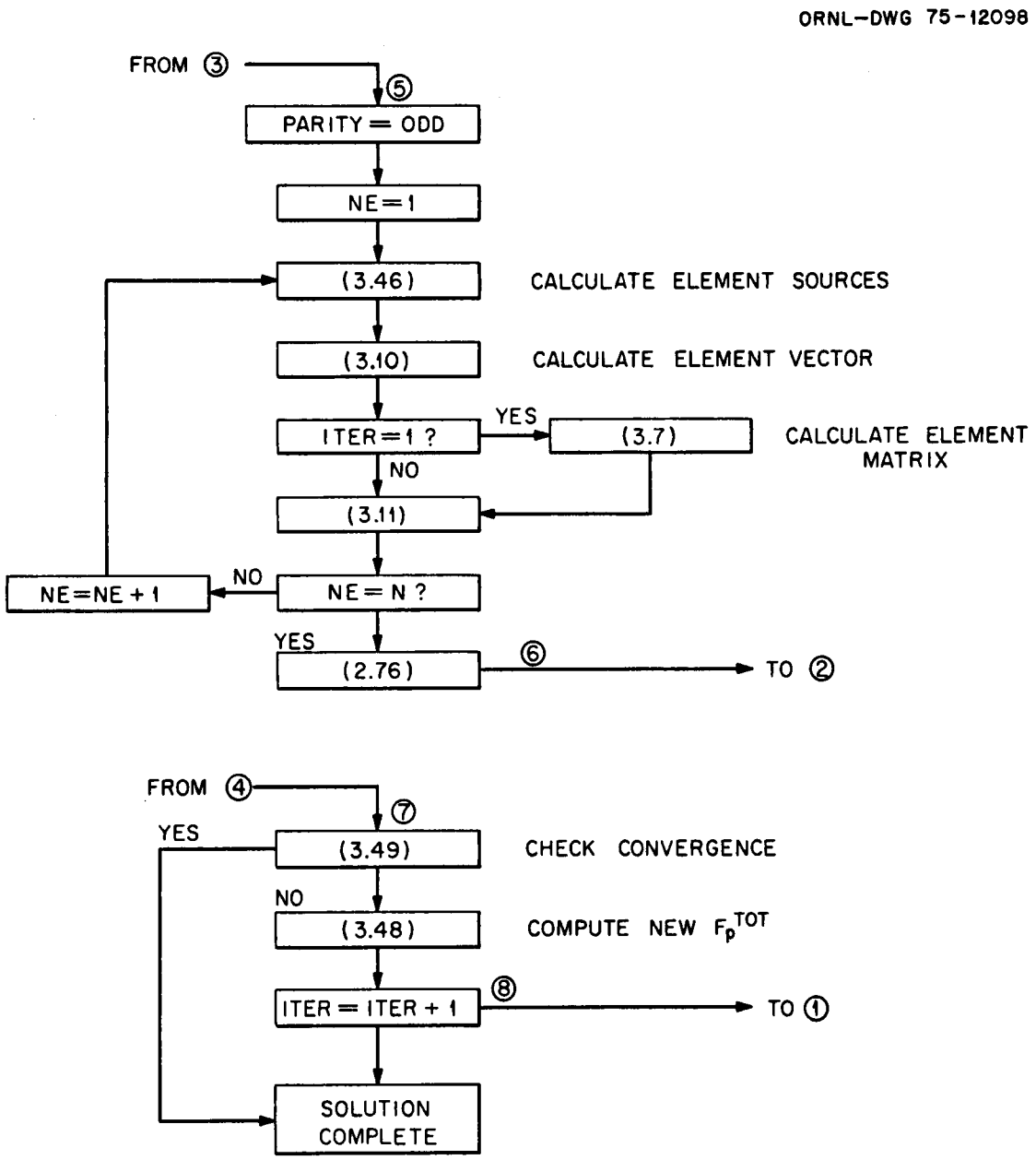


Figure 6. Flow diagram for odd parity flux calculation and outer iteration convergence check.

$$\psi^{o}_{g,d,p} = \{S^{o}_{g,d,p} - \sum_{i=1}^{3} (\mu_d b_i + \eta_d c_i)\ \psi^{e}_{g,d,i}/\Delta$$

$$+ \sum_{d'=1}^{D} (\underline{\underline{G}}^{o}_{p})_{dd'}\ [S^{o}_{g,d',p} -$$

$$\sum_{i=1}^{3} (\mu_{d'} b_i + \eta_{d'} c_i)\ \psi^{e}_{g,d',i}]/[(\underline{\underline{w}})_{dd}\ \Delta]\}/\Sigma_g \qquad (3.50)$$

and

$$\psi^{e}_{g,d,p} = \{[S^{e}_{g,d,p} - \sum_{i=1}^{3} (\mu_d b_i + \eta_d c_i)\ \psi^{o}_{g,d,i}/\Delta$$

$$+ \sum_{d'=1}^{D} (\underline{\underline{G}}^{e}_{p})_{dd'}\ [S^{e}_{g,d',p} -$$

$$\sum_{i=1}^{3} (\mu_{d'} b_i + \eta_{d'} c_i)\ \psi^{o}_{g,d',i}]/[(\underline{\underline{w}})_{dd}\ \Delta]\}/\Sigma_g. \qquad (3.51)$$

Equations (3.50) and (3.51) may be used to approximate the element averaged group odd and even parity fluxes once the even and odd parity system equations have been solved for the nodal even and odd parity fluxes, respectively. Even though this alternate procedure is simpler and numerically more efficient, it is not as accurate in predicting angular fluxes. The loss in accuracy occurs because the auxillary relationships impose a constant gradient condition due to the use of linear interpolating polynomials. However, as demonstrated in the next chapter, the loss of accuracy is in certain calculations not severe

enough to warrant discarding the use of the auxillary relationships as an alternative to solving both the even and odd parity system equations.

Numerical Implementation

To conclude this chapter, the numerical procedures used in eigenvalue and distributed source problems will be briefly described. The eigenvalue problem results in determining the effective multiplication factor K defined as the ratio of system gains to system losses. The iterative procedure for an eigenvalue calculation may be written[32]

$$\underline{\underline{L}}\ \underline{X}^{(n)} = \underline{\underline{P}}\ \underline{X}^{(n-1)}/K^{(n-1)}. \tag{3.52}$$

The matrix operators, $\underline{\underline{L}}$ and $\underline{\underline{P}}$ represent energy, spatial, and angular discretized loss and production operators, respectively. The vector $\underline{X}^{(n)}$ represents the n^{th} iterative estimate of the solution vector. The n^{th} iterative estimate of the multiplication factor is given by

$$K^{(n)} = F_T^{(n)}\ K^{(n-1)}/F_T^{(n-1)}$$

where

$$F_T^{(n)} = 2 \sum_{p=1}^{P} F_p^{TOT(n)}\ \Delta_p.$$

After $K^{(n)}$ is sufficiently converged, i.e.,

$$|K^{(n)} - K^{(n-1)}|/K^{(n)} \leq \varepsilon^* \tag{3.53}$$

where ε^* is some small positive number, normally 10^{-3} to 10^{-5}, Equation (3.59) is employed to monitor the required flux convergence.

A direct power iteration scheme for distributed source problems can be written

$$\underline{\underline{L}}\ \underline{X}^{(n)} = \underline{\underline{P}}\ X^{(n-1)} + \underline{Q} \tag{3.54}$$

where the vector $\underline{Q}$ represents the energy, spatial, and angular discretized distributed source. Unfortunately, unlike Equation (3.52), Equation (3.54) converges very slowly especially when K is close to unity. To overcome this slow convergence, a residual approach[32] was utilized in this work. Although very sophisticated scaling techniques may be used,[33] the residual approach was chosen because of the ease with which it may be numerically implemented. This approach consists of performing an eigenvalue calculation without renormalization, i.e.

$$K^{(n)} = F_T^{(n)}/F_T^{(n-1)}$$

to evaluate the fission source residuals in a distributed source calculation. Thus, when Equation (3.53) is satisfied, the total fission source is approximated by

$$F_T^{(n)} \cong \sum_{t=1}^{n-1} F_T^{(t)} + F_T^{(n)}/[1 - K^{(n)}].$$

To obtain the final solution, the direct power iteration scheme represented by Equation (3.54) is employed until Equation (3.49) is satisfied.

CHAPTER IV

NUMERICAL RESULTS

In order to evaluate the finite element formulation presented in Chapter II, a computer program (DAFE-Discrete Angle-Finite Elements) employing the solution techniques described in Chapter III has been written and used to analyze a series of test problems. Comparative results were obtained using other codes employing more established calculational techniques. Of primary concern in choosing these test problems was they illustrate the advantages as well as establish the limitations of the formulation. However, an additional requirement was that their analysis aid in identifying those areas where continued development would prove most useful. With the preceding in mind, the purpose of this chapter is to present and discuss the results of these comparative calculations.

Ray Effect Problems

The first two test problems were chosen to illustrate angular and scalar flux distortions which occur in certain discrete ordinates calculations. These distortions, called ray effects, are due to the discretization of the angular variable in the divergence term of the transport equation. The use of discrete angles restricts particles to travel or stream in straight lines between collisions. Thus, when isolated sources are present in weak scattering media, anomalities often appear in the angular or scalar fluxes.

A comparison of the right edge scalar fluxes, generated using DAFE and the two-dimensional discrete ordinates code DOT,[34] is presented in Figure 7. A geometrical description, including cross sections and boundary conditions, is also shown. The discrete angle-finite element and the discrete ordinates results are denoted by E_N and S_N, respectively. The S_N results were obtained using 90° rotationally symmetric quadratures.[35] Because of the angular symmetry in the canonical form of the transport equation, only those discrete angles having positive direction cosines with respect to the X-axis, i.e., μ's > 0, were chosen from the above quadratures for use in the E_N calculations. Including the zero weight directions, the S_2, S_4, and S_8 calculations required 6, 16, and 48 discrete angles, respectively, whereas the E_2 and E_4 calculations required only two and six directions. In all the S_N calculations, the x-y mesh consisted of 64 squares 0.25 cm on a side. The E_N results were obtained using 128 triangles which were formed by bisecting these squares from lower left to upper right.

As expected, the E_2 and S_2 curves incorrectly predict the scalar flux due to the use of low order angular quadratures. Increasing the number of discrete angles, as in the E_4 and S_4 calculations, does result in more realistic flux shapes. However, anomalous humps or ray effects appear in the S_4 results while the smoothness of the E_4 curve illustrates the absence of any pronounced distortions. An even further increase in the number of discrete angles used in the discrete ordinates calculations does not eliminate the ray effects since flux distortions continue to be present in the S_8 curve. In view of these results, it

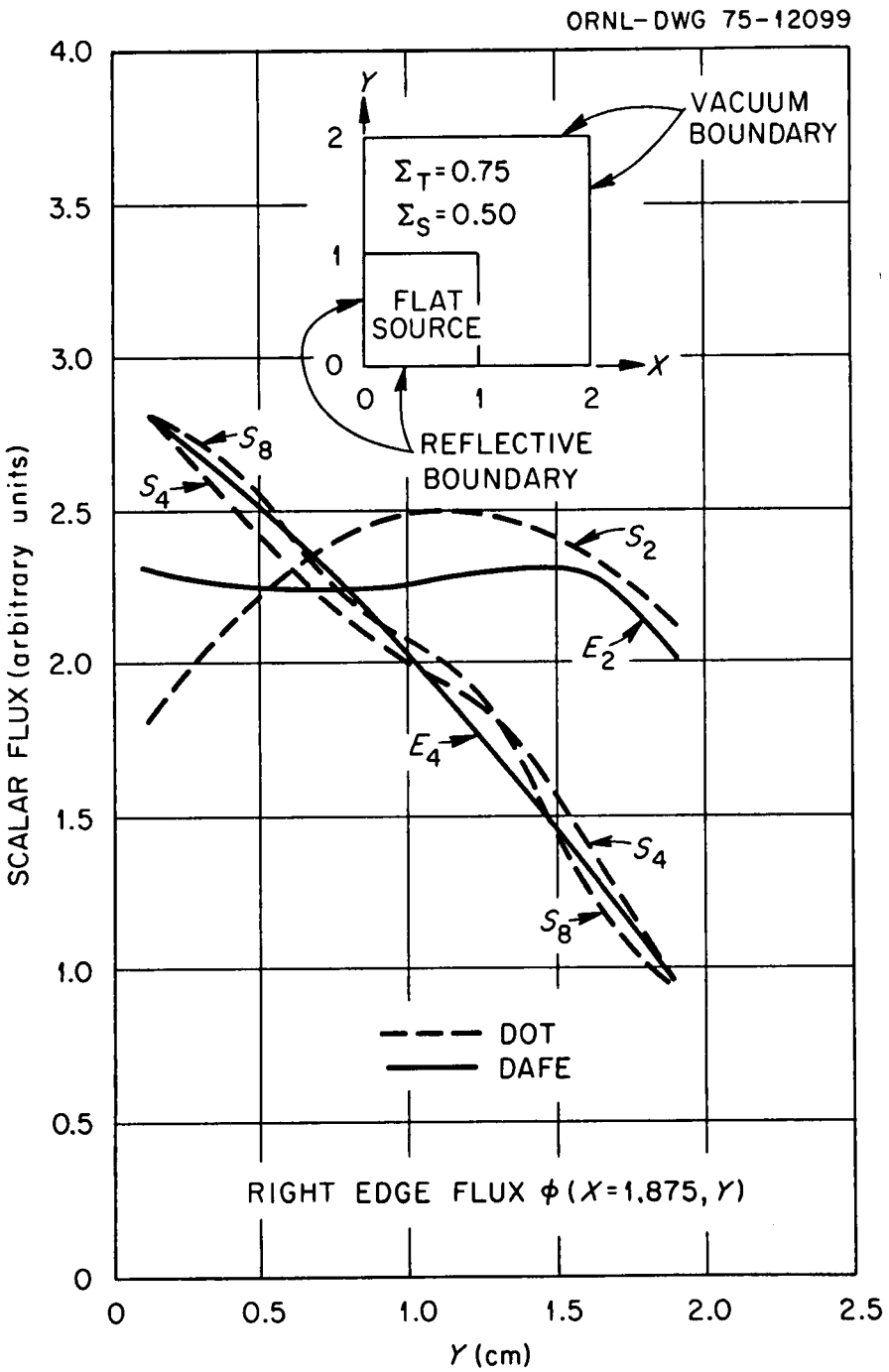


Figure 7. Comparison of right edge (X=1.875) scalar flux in a weak scattering material using DOT and DAFE.

appears that using the discrete angle-finite element formulation is superior to using a greater number of angles in a discrete ordinates calculation in mitigating ray effects.

To substantiate the above conclusion, a second two-region problem was analyzed. The results of this analysis together with a description of the problem are presented in Figure 8. The S_4 and E_4 results were obtained using 144 squares and 288 triangles, respectively. However, unlike the preceding problem, the triangles were not formed by bisecting all the squares from lower left to upper right. The upper left and lower right squares were bisected in the opposite direction. This difference in forming the triangles was required to accommodate the vacuum boundary conditions since only one side of a triangle may lie along a vacuum boundary surface (see Figure 2 on page 44). In addition, the S_{12} calculation which contained 96 discrete directions was performed using 576 squares 0.125 cm. on a side.

In Figure 8, the S_4 flux is badly distorted especially near the vacuum boundaries where the flux gradients predict an inward flow of neutrons. The S_{12} curve is more representative of the physical situation. However, the presence of many small humps is indicative of persisting ray effects in spite of the large number of discrete directions. Unlike the S_4 flux, the E_4 flux does not exhibit the same poor boundary behavior, but it does exhibit the large hump in the high scattering region. The large hump could be indicative of ray effects; however, the smoothness of the E_4 curve contradicts this assumption. Performing another E_N calculation with a greater number of discrete

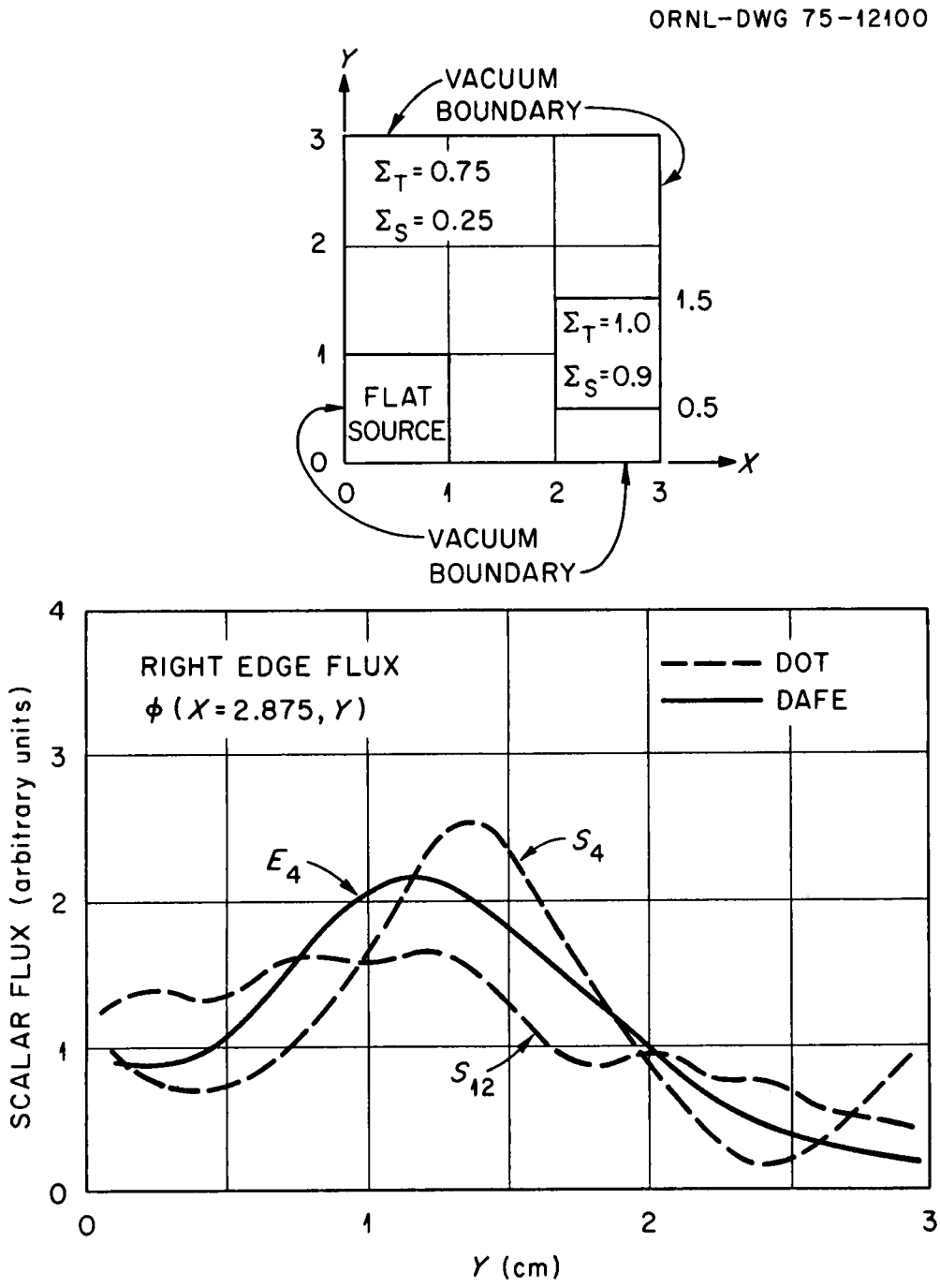


Figure 8. Comparison of right edge (X=2.875) scalar flux in both a weak and strong scattering material using DOT and DAFE.

angles might resolve this contradiction. Unfortunately, the present numerical implementation of the discrete angle-finite element formulation precludes the use of more angles due to the large storage requirements imposed by the direct inversion scheme. In spite of these results, it does appear that the present formulation provides a viable means of reducing if not eliminating ray effects.

Streaming Problem

In the preceding section, the appearance of ray effects in discrete ordinates calculation was attributed to the angular discretization which restricted neutrons to stream in straight lines between collisions. Ray effects are not present when other deterministic calculational methods based on diffusion theory or spherical harmonics are employed because they do not restrict neutrons to stream between collisions since the angular variable is either not considered or it is treated as a continuous variable. However, these methods are not totally adequate in obtaining realistic solutions in most shielding calculations where streaming is of primary concern. This is especially true when voids or gaps are present and the angular flux becomes collimated. Since the discrete angle-finite element formulation reduced ray effects in the preceding calculations, the purpose of this section is to present a very brief investigation of its use on a fairly simple problem where streaming does exist.

The test problem chosen to investigate streaming and the results obtained using symmetric quadratures[35] are shown in Figure 9. As

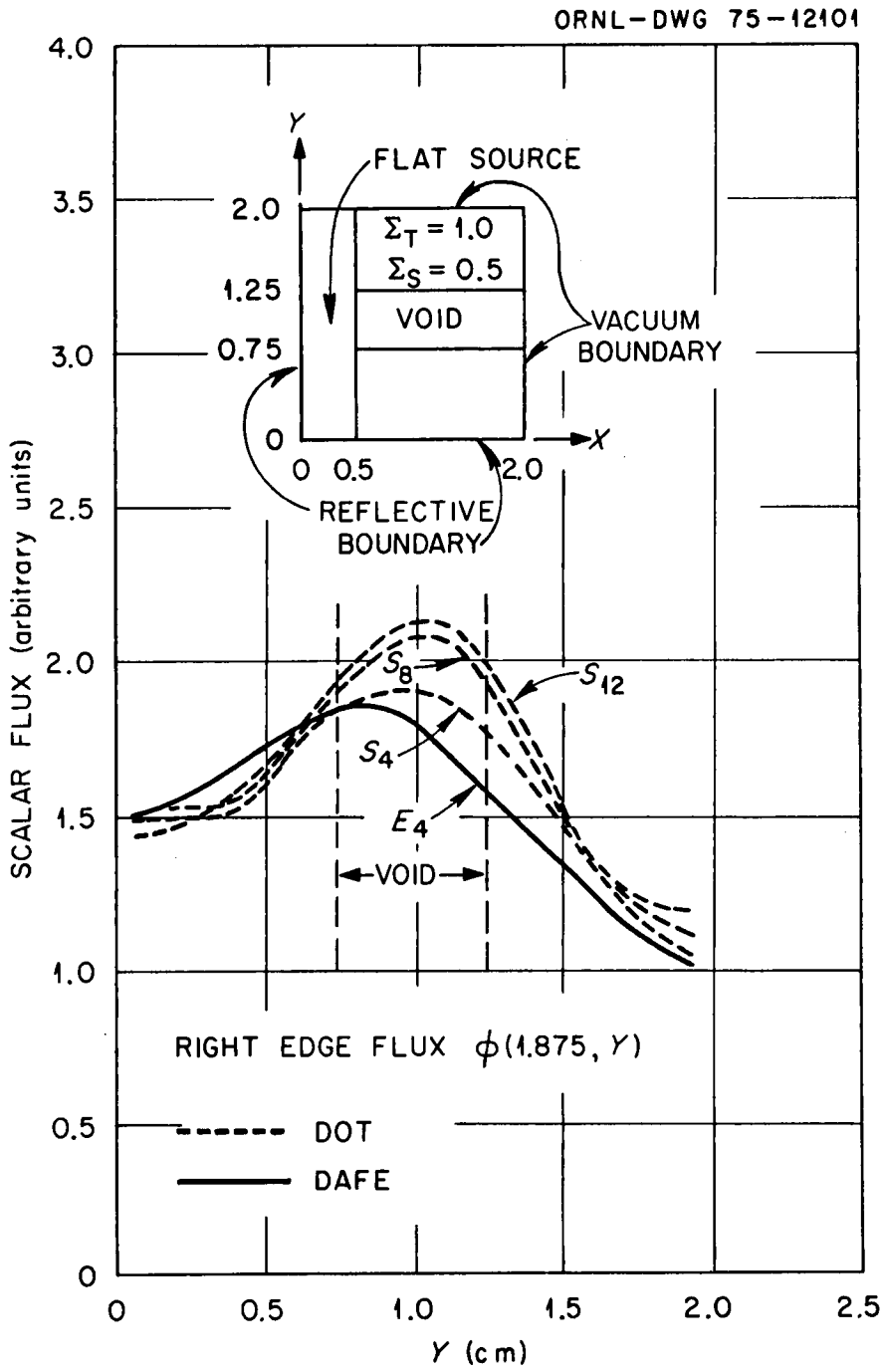


Figure 9. Comparison of right edge (X=1.875) scalar flux in the presence of a void using DOT and DAFE.

illustrated, this problem consisted of a flat source region butting against a weak scattering region which contained a void. Such an arrangement permitted neutrons to stream through the void. The spatial mesh used for these calculations was the same as that used for the first ray effect problem, i.e., 64 squares for the S_N calculations and 128 triangles for the E_4 calculation.

In Figure 9, both the E_4 and S_4 scalar flux shapes along the right edge exhibit peaks in the void where streaming occurs. As expected, since the discrete angle-finite element formulation reduced ray effects and thus streaming, it does not peak as much as the S_4 discrete ordinates calculation. The S_8 and S_{12} calculations, which contained many more directions, indicate however that both the E_4 and S_4 curves underestimate the flux peak.

In many shielding problems where streaming is important, discrete ordinates methods may take advantage of especially tailored quadrature sets. If it is known in advance that most of the angular flux will be contained in a narrow band of directions, most of the available directions may be clustered in this range. In Figure 10, the results for such a modification are presented. For comparative purposes, the S_{12} curve from the previous calculation is also shown. The flux shapes obtained using the modified quadratures, which contained the same number of directions as the S_4 and E_4 quadratures, are denoted by MOD S_4 and MOD E_4 respectively.

The most widely accepted method of tailoring quadrature sets is to add directions of a high order quadrature to a low order quadrature.[2,35] This procedure is easily implemented when many levels

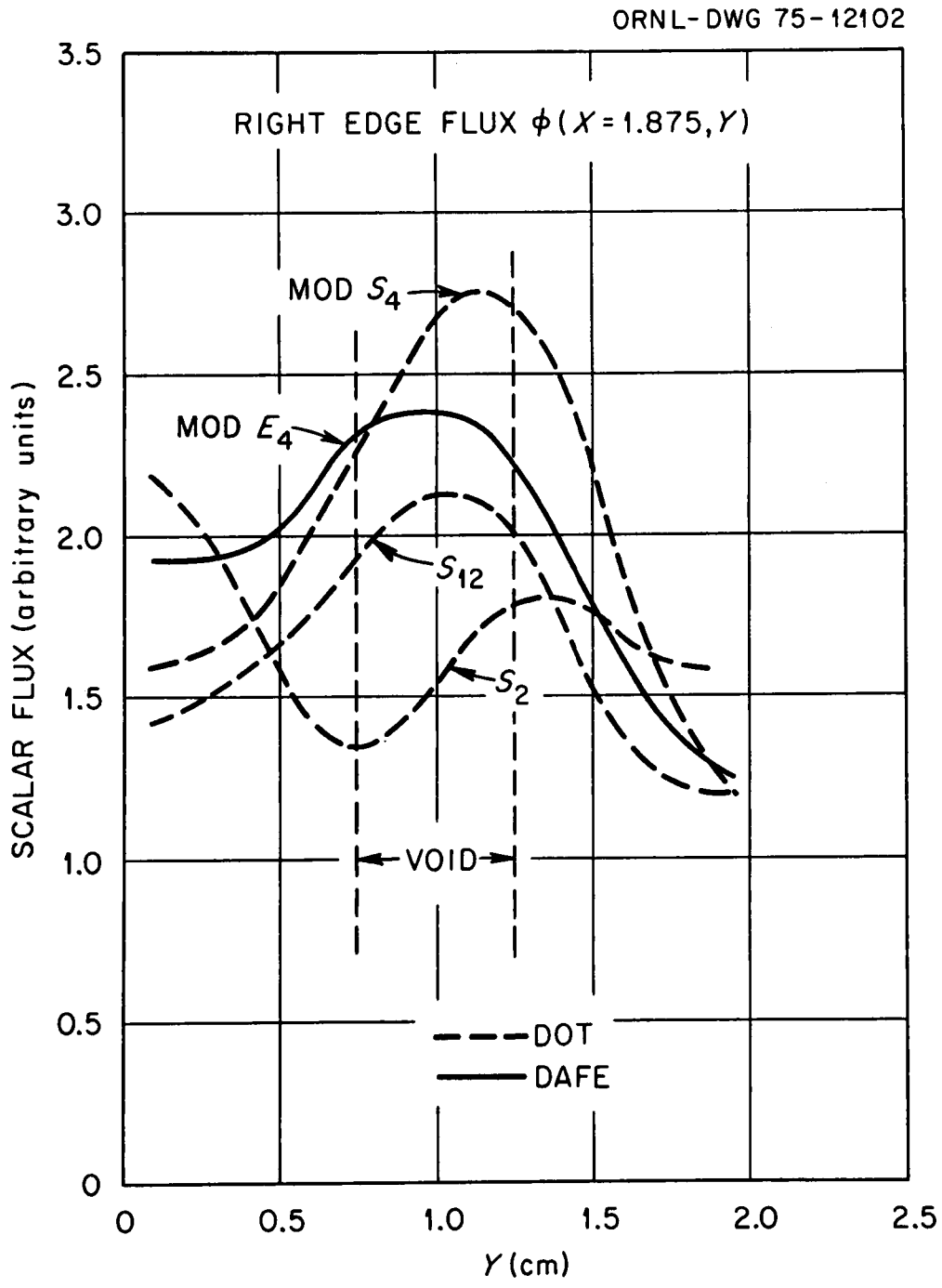


Figure 10. Comparison of right edge (X=1.875) scalar flux in the presence of a void using modified angular quadratures in DOT and DAFE.

in a high order quadrature equal or nearly equal the total solid angle in one level of a low order quadrature. Quadratures formed in this manner usually contain a very large number of directions due to the additional angles. These sets are also often antisymmetric with regard to one direction cosine.

The present version of DAFE will not accept large quadratures due to computer fast core storage limitations nor will it accept antisymmetric quadratures due to the manner it imposes reflected boundary conditions (see Chapter III, page 52). For these reasons, the modified E_4 quadrature was constructed by simply substituting the four S_{12} angles having the greatest X-direction cosines for the four similarly directed angles in the unmodified E_4 quadrature. To ensure symmetry with regard to both direction cosines, a comparable S_4 quadrature was constructed by likewise replacing both these same directions and the four reflected directions. The modified weights were obtained by adjusting, through normalization, the original weights associated with each direction in an effort to conserve total solid angle.

The general flux shape of the modified E_4 calculation agrees very favorably with the S_{12} curve although the magnitude of the E_4 flux is approximately 20% higher. However, the discrepancy can most likely be attributed to the simplistic approach used to construct the modified quadratures. This argument appears substantiated by the large disagreement between the modified S_4 flux and the S_{12} result. Not only is the magnitude of the S_4 flux considerably greater, its peak occurs near the vacuum boundary edge of the void. In view of the material symmetry,

i.e., identical material on either side of the void, the flux peak should occur near the reflective boundary side of the void. Although the S_{12} and modified E_4 curves differ, these results demonstrate that the discrete angle-finite element formulation may also make use of tailored quadratures. In addition, the completely erroneous S_2 flux indicates that the E_N formulation is capable of yielding more realistic solutions to streaming problems than other methods employing low order angular treatments.

One-Dimensional Eigenvalue Problem

The incorporation of anisotropic scattering in discrete ordinates formulations is rather routine due to the replacement of the scattering integral by a discrete sum. Since a primary objective of this work consisted of including anisotropic scattering in a finite element formulation, a discrete rather than continuous approximation was likewise employed to treat the angular variable in the canonical form of the transport equation. Thus, the primary purpose of this section is to verify the treatment of anisotropic scattering in the discrete angle-finite element formulation.

The problem chosen for this verification was a seven region, one-dimensional model of the FTR-3 loading of the ZPR-9 at Argonne National Laboratory[36] as shown in Figure 11. A previously generated[32] five group, P_3 scattering cross section set was utilized to perform a series of eigenvalue calculations using DAFE. Independent calculations were again performed using DOT and compared with the DAFE

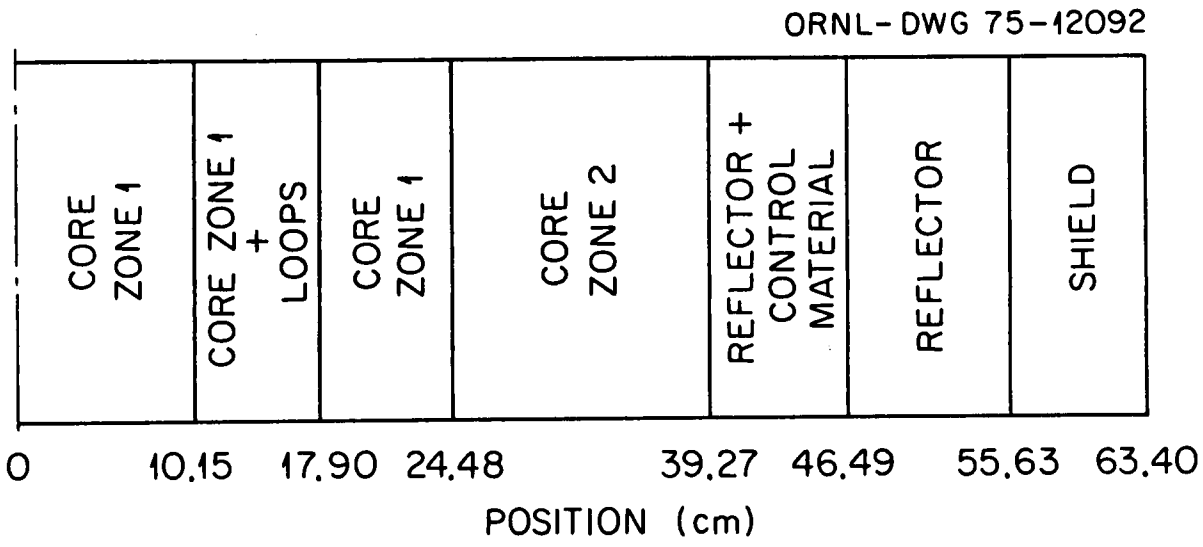


Figure 11. Half core mockup of FTR-3 loading in ZPR-9.

results. Since both DAFE and DOT are two-dimensional codes, a height of one centimeter was assumed and reflective boundary conditions were imposed on the upper and lower boundaries. The left and right boundaries were reflective and vacuum, respectively.

The spatial mesh for the DOT calculations consisted of 72 rectangles, each having a height, i.e., Δy of one cm. The widths of all rectangles, i.e., the Δx's, were equal in each material region but not necessarily in different regions. To perform the DAFE calculations, 144 triangles were constructed. These triangles were obtained by combining the 72 rectangles into pairs, thus forming 36 rectangles. These rectangles were then cross bisected yielding four isosceles triangles per rectangle. This procedure allowed comparable Δx's to be used in both the DOT and DAFE calculations. Maintaining comparable Δy's was not necessary since the problem was one-dimensional.

The results from these calculations are presented in Table I. Two sets of eigenvalues were obtained, i.e., with and without a conventional $D_g B^2$ buckling correction, where D_g is the diffusion coefficient for group g and B^2 is the transverse geometric buckling. Adding $D_g B^2$ to each group's total cross section approximates total leakage loss by increasing the total absorption loss. As a further check, P_0 calculations using the KENO[37] Monte Carlo code were also performed. In both the DOT and DAFE calculations, convergence criteria of 10^{-3} and 10^{-4} were imposed on the pointwise flux and eigenvalue, respectively. The KENO results were generated using 103 batches with each batch containing 30 neutrons. Thus, neglecting the three starting batches, a total of 30,000 histories was followed in each KENO calculation.

TABLE I

COMPARISON OF EIGENVALUES WITH ANISOTROPIC SCATTERING

	DOT			DAFE		
S_NP_L	K	% DIF[a]	E_NP_L	K	% DIF[a]	% DIF[b]
S_2P_0	1.1496	-1.31	E_2P_0	1.1551	-0.84	0.48
S_2P_1	1.1304	---	E_2P_1	1.1355	---	0.46
S_4P_0	1.1515	-1.15	E_4P_0	1.1576	-0.63	0.53
S_4P_1	1.1329	---	E_4P_1	1.1386	---	0.50
S_4P_3	1.1332	---	E_4P_3	1.1389	---	0.50
S_2P_0	0.9918[c]	-0.31	E_2P_0	0.9966[c]	0.15	0.48
S_2P_1	0.9766	---	E_2P_1	0.9810	---	0.45
S_4P_0	0.9939	-0.10	E_4P_0	0.9989	0.40	0.50
S_4P_1	0.9790	---	E_4P_1	0.9838	---	0.49
S_4P_3	0.9794	---	E_4P_3	0.9841	---	0.48

[a]Percent difference using KENO P_0 K = 1.1649 ± 0.0078 and KENO P_0 K = 0.9949 ± 0.0077 with DB^2 correction.

[b]Percent difference assuming DOT values are correct.

[c]Calculated with DB^2 correction.

The DOT and DAFE results are designated $S_N P_L$ and $E_N P_L$, respectively. As explained previously, the symbols S_N and E_N are used to denote the order of the angular quadrature, whereas the symbol P_L denotes a L'th order Legendre expansion was used to represent the scattering cross sections.

In Table I, both the DOT and DAFE eigenvalues are well within the standard deviations of the KENO results for the P_0 cases. Comparison of the DAFE and DOT eigenvalues reveals that DAFE consistently predicts eigenvalues which are 0.5% greater than DOT eigenvalues. Small differences, approximately 2%, were also found when comparing the DAFE and DOT pointwise group scalar fluxes. As in the eigenvalue comparisons, these differences were likewise consistent regardless of the order of scattering anisotropy, i.e., P_0, P_1, or P_3. Based on this consistency, it appears that the discrete angle-finite element formulation is indeed capable of handling anisotropic scattering.

As noted in Chapter III, the auxillary relationships given by Equations (3.50) and (3.51) may be used to calculate ψ^o and ψ^e, respectively. Thus, before concluding this section, a comparison of eigenvalues generated from DAFE using both functionals, even-parity functional with odd auxillary relationship and odd-parity functional with even auxillary relationship is presented in Table II. These calculations were also performed using the ZPR-9 one-dimensional model. From this comparison, it is obvious that the auxillary relationships may be used in place of either functional to obtain integral parameters such as K. A comparison of the group scalar fluxes (now shown) yielded a similar conclusion with regard to pointwise scalar fluxes.

TABLE II

COMPARISON OF EIGENVALUES USING AUXILLARY RELATIONSHIPS

$E_N P_L$	K Obtained Using Both Functionals[a]	Even Functional Odd Auxillary[b]	Odd Functional Even Auxillary[c]
E_2P_0	1.1551	1.1551	1.1553
E_2P_1	1.1355	1.1355	1.1357
E_4P_0	1.1576	1.1576	1.1578
E_4P_1	1.1386	1.1386	1.1387
E_4P_3	1.1389	1.1389	1.1390
E_2P_0	0.9966[d]	0.9966[d]	0.9968[d]
E_2P_1	0.9810	0.9810	0.9816
E_4P_0	0.9989	0.9989	0.9990
E_4P_1	0.9838	0.9838	0.9830
E_4P_3	0.9841	0.9841	0.9842

[a]Even parity functional given by Equation (2.61), odd parity functional given by Equation (2.63).

[b]ψ^o found from Equation (3.50).

[c]ψ^e found from Equation (3.61).

[d]Buckling corrected.

These same conclusions cannot be equally applied with regard to angular fluxes since a spot check revealed differences of up to 50% between the three possible choices of solution. It is interesting to note that in spite of these differences, the eigenvalues in Table II are essentially equal, even for the anisotropic cases where both the even and odd-parity angular fluxes are needed to construct the downscatter sources. The agreement in eigenvalues when use is made of the odd functional and even auxillary relationship is even more noteworthy since only the even-parity angular flux appears directly in calculating scalar fluxes and thus the eigenvalues. In concluding, the important point to be realized from the results presented in this section is that the discrete angle-finite element formulation is capable of predicting eigenvalues and scalar fluxes while only directly considering half the angular phase space associated with discrete ordinates methods. This conclusion is independent of the scattering order.

Two-Dimensional Eigenvalue Problems

In this section, the accuracy, relative to other comparable solution methods, and limitations of the discrete angle-finite element formulation are investigated. Since the objective of the present study was to develop a numerical technique capable of providing approximate solutions to the energy dependent two-dimensional Boltzmann transport equation, results obtained from the analysis of three multigroup two-dimensional eigenvalue problems are presented. The first problem to be analyzed was designed to illustrate application of the discrete angle-finite element formulation to nonorthogonal

geometries. A second rather severe test problem was analyzed to establish the limitations of the formulation. Finally, the third and last problem, which is fairly representative of a realistic reactor model, was analyzed to demonstrate the importance of incorporating anisotropic scattering into the formulation.

Nonorthogonal geometry model. A geometrical description of the model used for the first two-dimensional eigenvalue calculations is shown in Figure 12. Although this model is atypical of hexagonal lattices, it does contain material arrangements common to such lattices. Without modification, it would be difficult to obtain a solution using conventional finite difference methods because of the nonorthogonal material interfaces. For this reason, the triangular mesh discrete ordinates code TRIPLET[21] was employed to generate comparative results.

The cross sections used in the present analysis were obtained from the five group P_3 scattering set discussed in the preceding section. As shown in Figure 12, only the core and reflector materials were considered. Two different sets of boundary conditions were used. The first set, representative of cell calculations, consisted of reflecting all four sides. To obtain a steep flux gradient, the second set differed in that the right side was made a vacuum boundary.

In order to generate comparative results using DOT and KENO, the material arrangement depicted in Figure 12 was modified. This modification, which is illustrated in Figure 13, was accomplished by simply conserving material volumes. To maintain clarity in the presentation of

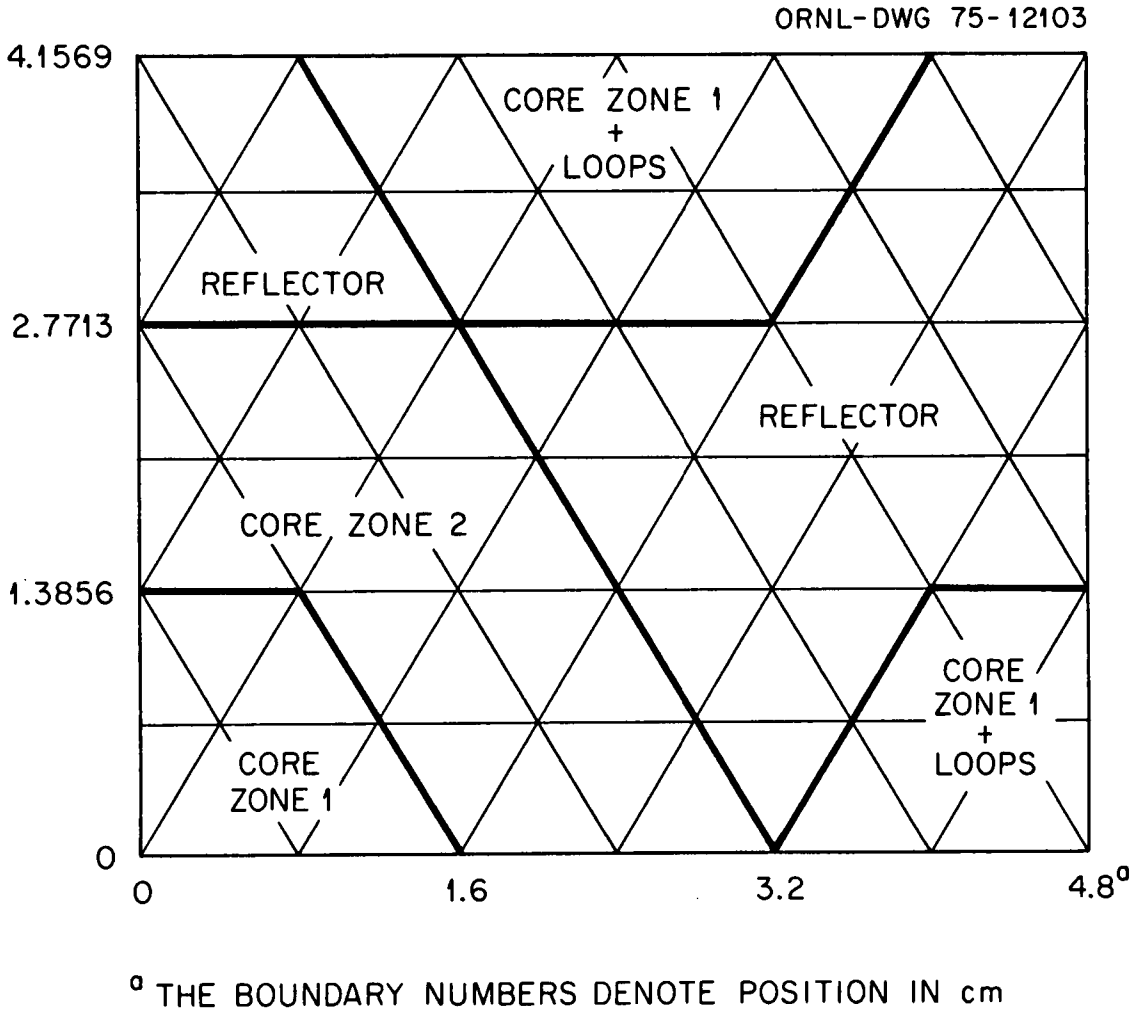


Figure 12. Triangular mesh description for hexagonal model eigenvalue comparison using TRIPLET and DAFE (test case 1).

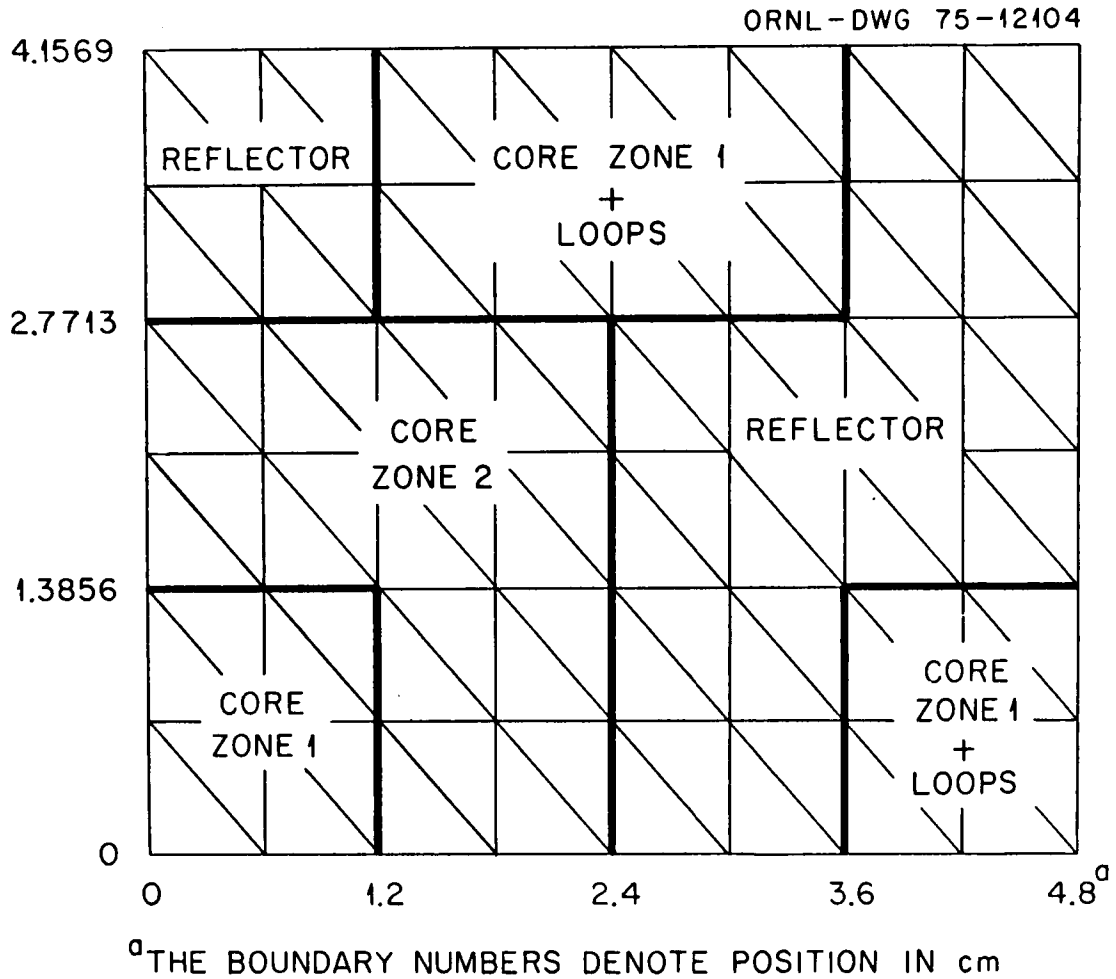


Figure 13. Mesh description for modified hexagonal model eigenvalue comparison. Rectangles denote DOT mesh; triangles denote TRIPLET and DAFE mesh (test case 2).

the results, the hexagonal and modified hexagonal models have been designated test cases 1 and 2, respectively.

A comparison of the two-dimensional eigenvalues using TRIPLET, DAFE, and DOT is presented in Table III. All of these results were obtained using the five group P_3 scattering cross sections and comparable S_4 angular quadratures. In addition, the same convergence criteria, i.e., 10^{-3} on the pointwise scalar fluxes and 10^{-4} on the eigenvalues, was used in all three codes.

For the totally reflected calculations, the differences in Table III are insignificant. However, when the vacuum boundary condition was imposed along the right side, DAFE yielded eigenvalues which were more than 1% lower than those obtained from TRIPLET. Since the vacuum boundary condition causes a step flux gradient to occur near the right edge, it was decided that a refinement of the triangular mesh near this edge might alleviate any breakdown there. The refinement was accomplished by incorporating more triangles into the mesh near the vacuum boundary of the unmodified hexagonal model as shown in Figure 14.

Additional calculations using TRIPLET and DAFE on the refined mesh model did not produce any noticeable change in the eigenvalues. In fact, the results of these calculations, denoted by test case 3 in Table III, were identical to those obtained from the unrefined mesh calculations. Because of these results, further comparisons were made by analyzing the modified hexagonal model using KENO.

The KENO calculations were performed, as in the preceding section, using 30,000 neutron histories. In addition, only P_0 scattering

TABLE III

COMPARISON OF TWO-DIMENSIONAL EIGENVALUES FOR HEXAGONAL MODEL

Test Case No.	Right Boundary Condition	TRIPLET	DAFE		DOT
		K	K	% DIF[a]	K
1	Reflective	1.0956	1.0949	-0.06	---
1	Vacuum	0.0840	0.0828	-1.43	---
2	Reflective	1.0958	1.0949	-0.08	1.0940
2	Vacuum	0.0842	0.0833	-1.07	0.0841
3	Vacuum	0.0840	0.0828	-1.43	---

[a]Percent difference based on TRIPLET values.

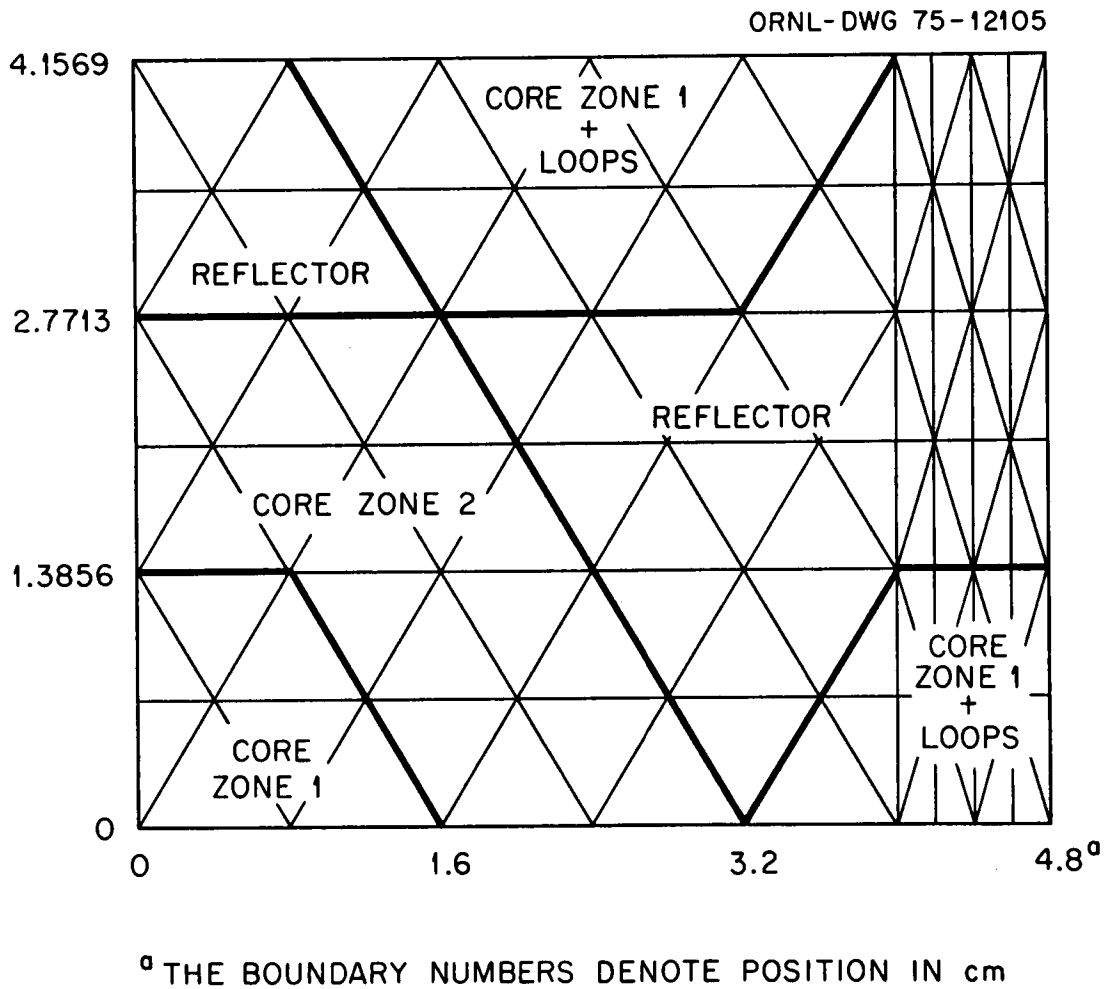


Figure 14. Vacuum boundary refined triangular mesh description for hexagonal model eigenvalue comparison using TRIPLET and DAFE (test case 3).

calculations were performed. The TRIPLET, DOT, and DAFE eigenvalues together with their percent differences from the KENO eigenvalues are given in Table IV for both the reflective and vacuum boundary cases.

Whereas, there is essentially no difference in the eigenvalues for the totally reflected case, all three deterministic codes yield eigenvalues more than 3% lower than the KENO eigenvalue for the vacuum boundary case. Based on these results, the 1% difference between the DAFE and TRIPLET eigenvalues does not appear very significant. However, the 1% differences do exist. Thus, although these results demonstrate the ability of the discrete angle-finite element formulation to obtain approximate solutions for geometrically nonorthogonal problems, its accuracy in obtaining these solutions appears suspect. For this reason, a more detailed analysis was performed on a second rather severe test problem.

High leakage test model. The model for the second two-dimensional test problem is shown in Figure 15. This problem is the same as that used by Kaper et al.[20] in their investigation of finite element approximation procedures. It is termed a severe test problem because all four sides are vacuum boundaries. Thus, it is a high leakage problem, and since the angular flux is highly anisotropic, such problems are difficult to analyze without a great deal of angular resolution.

The primary purpose of the present analysis was to obtain an estimate of the relative performance of the discrete angle-finite element formulation. For this reason, a considerable number of

TABLE IV

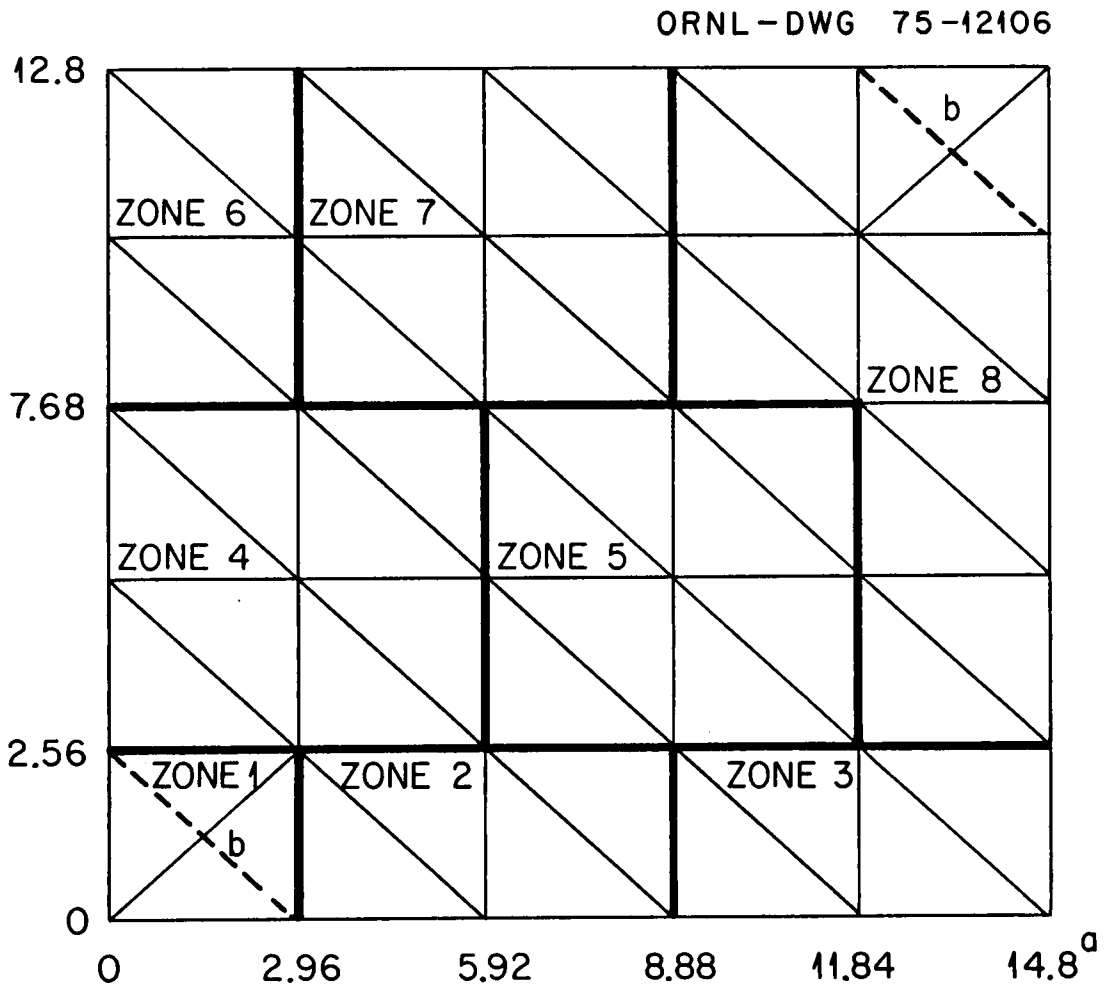
COMPARISON OF TWO-DIMENSIONAL EIGENVALUES FOR MODIFIED HEXAGONAL MODEL

Test Case No.	Right Boundary Condition	DOT		TRIPLET		DAFE	
		K	% DIF[a]	K	% DIF[a]	K	% DIF[a]
2	Reflective	1.0940	-0.25	1.0959	-0.07	1.0952	-0.14
2	Vacuum	0.0882	-3.15	0.0883	-3.02	0.0875	-3.90

[a]Percent difference based on KENO P_0 calculations

K = 1.0967 ± 0.0048 - Reflective Boundary

K = 0.0912 ± 0.0006 - Vacuum Boundary.



[a]THE BOUNDARY NUMBERS REPRESENT POSITION IN cm

[b]THE DOTTED LINES DENOTE THE TRIPLET TRIANGULATION IN THE LOWER LEFT AND UPPER RIGHT RECTANGLES

Figure 15. Typical regular triangle arrangement (50 triangles) for two-dimensional eigenvalue comparison.

eigenvalue calculations, using DOT, TRIPLET and DAFE, have been performed and compared to KENO. In these calculations, the spatial meshes (including type of triangulation) and angular quadratures have been varied. A six-group P_0 cross section set, contained in reference 20, was used in all calculations. Of the eight material zones shown in Figure 15, all contain fissionable material except zone 4.

As in previous calculations, the convergence criteria used in obtaining the DOT, TRIPLET and DAFE results was 10^{-3} on the pointwise scalar fluxes and 10^{-4} on the eigenvalues. Also, the KENO calculation was again performed using 30,000 neutron histories. A typical triangle arrangement for the TRIPLET and DAFE calculations is shown in Figure 15. The lower left and upper right rectangles contain a different triangulation for each code as indicated. Whereas, DAFE requires the use of two triangles at the intersection of two vacuum boundaries as explained earlier, TRIPLET only requires one. However, TRIPLET does require the use of a regular triangular mesh in that each interior mesh point must be common to six triangles. Thus, the difference in triangulation for these two rectangles.

A second type of triangulation was also used in the DAFE calculation. This triangulation, which has been designated the crossed triangle arrangement to distinguish it from the regular triangle arrangement, is shown in Figure 16. The 60 crossed triangles depicted in Figure 16 were formed by simply bisecting the 30 regular triangles. In addition, a 100 crossed triangle arrangement was likewise obtained from the 50 regular triangle arrangement. The spatial meshes used in

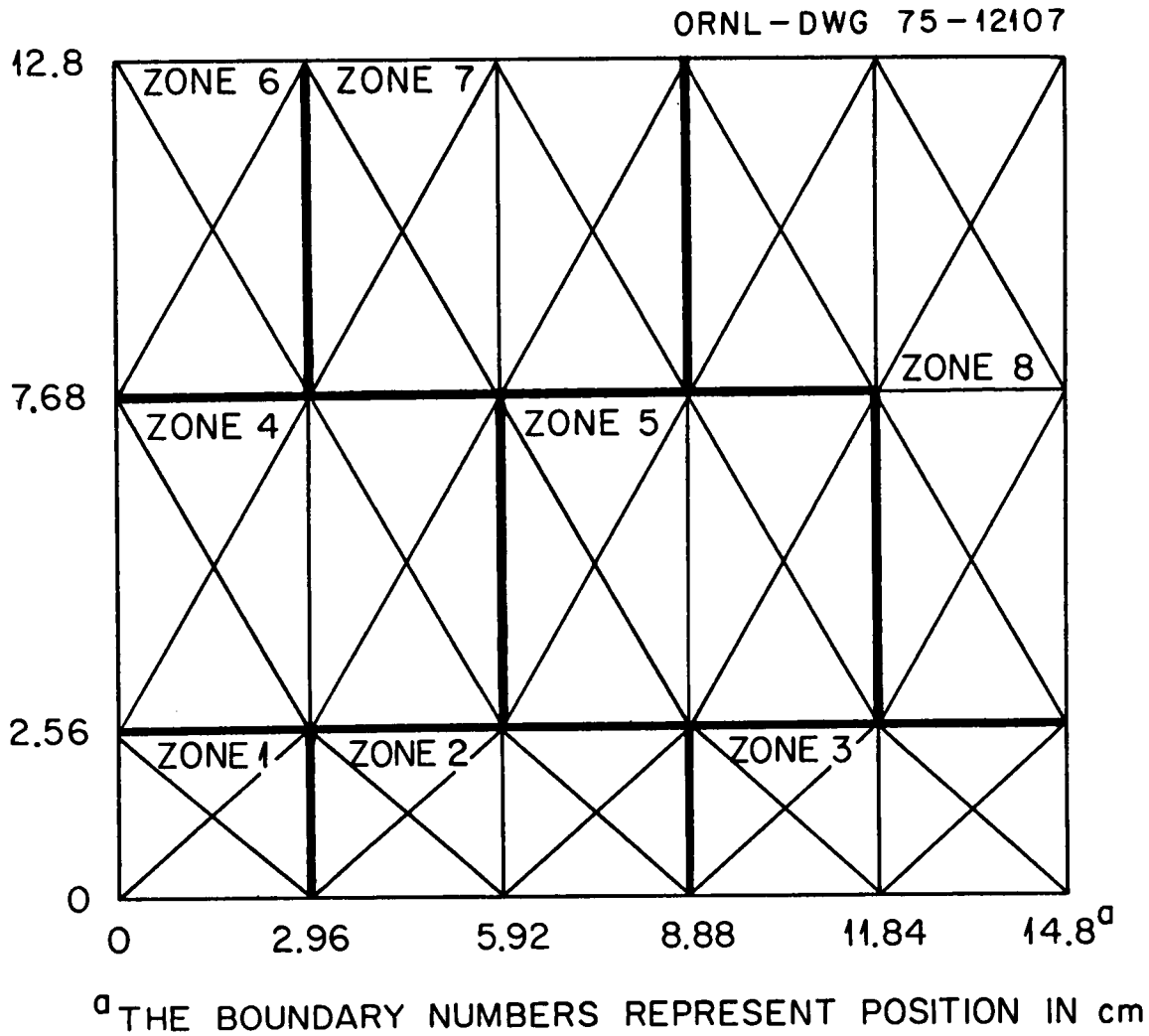


Figure 16. Typical crossed triangle arrangement (60 triangles) for two-dimensional eigenvalue comparison.

the DOT calculations consisted of the rectangles which enclosed the triangles.

The results of these calculations are presented in Table V. The eigenvalues obtained from the DOT, TRIPLET, and DAFE calculations are again compared with the KENO eigenvalue which is taken as the benchmark value. There are no DOT or TRIPLET results presented for the 60 and 100 triangle cases. These triangulations are both crossed type triangle arrangements. TRIPLET cannot handle these arrangements because of the interior node-six triangle restriction. The DOT calculations were not performed since the rectangular mesh would be equivalent to that used in the 30 and 50 triangle cases.

As in the previous two-dimensional comparison, the DOT, TRIPLET, and DAFE eigenvalues are all lower than the KENO value. Of the three deterministic codes, TRIPLET consistently yields better results. However, all three converge toward the benchmark value when the spatial mesh is refined or when the angular quadrature is increased. The only inconsistency in this trend appears when the DAFE 60 crossed triangle eigenvalues are compared to the 50 regular triangle results. Although 60 is greater than 50, this increase does not represent a refinement of the triangular mesh. In fact, many of the triangles in Figure 16 are greater in size than those in Figure 15, page 95. Thus, in view of these remarks, the DAFE results in Table V should not be considered inconsistent.

In Figure 17, a comparison of the group scalar fluxes is presented. These fluxes were obtained using comparable S_4 angular quadratures in

TABLE V

COMPARISON OF TWO-DIMENSIONAL EIGENVALUES WITH ALL VACUUM BOUNDARIES

Angular Quadrature[a]	No. of Triangles[b]	DOT		TRIPLET		DAFE	
		K	% DIF[c]	K	% DIF[c]	K	% DIF[c]
S_2	30	0.1462	-18.15	0.1526	-14.56	0.1440	-19.39
S_2	50	0.1556	-12.93	0.1578	-11.66	0.1540	-13.78
S_2	60	---	---	---	---	0.1484	-16.91
S_2	100	---	---	---	---	0.1581	-11.52
S_2	200	0.1600	-10.51	0.1607	-10.07	0.1590	-10.99
S_4	30	0.1586	-11.09	0.1651	-7.62	0.1560	-13.25
S_4	50	0.1711	-4.24	0.1725	-3.45	0.1662	-6.96
S_4	60	---	---	---	---	0.1560	-10.46
S_4	100	---	---	---	---	0.1710	-4.30
S_4	200	0.1754	-1.82	0.1760	-1.48	0.1734	-2.96

TABLE V (continued)

Angular Quadrature[a]	No. of Triangles[b]	DOT		TRIPLET		DAFE	
		K	% DIF[c]	K	% DIF[c]	K	% DIF[c]
S_6	30	0.1588	-11.13	0.1654	-7.40	0.1549	-13.30
S_6	50	0.1716	-3.93	0.1730	-3.14	0.1664	-6.88

[a] S_2, S_4, and S_6 denote use of 6, 16, and 30 angles in DOT calculations; 4, 12, and 24 in TRIPLET; 2, 6, and 12 in DAFE.

[b] Number of rectangles for DOT calculations was one-half the number of triangles given.

[c] Percent difference based on KENO K = 0.1787 ± 0.0012.

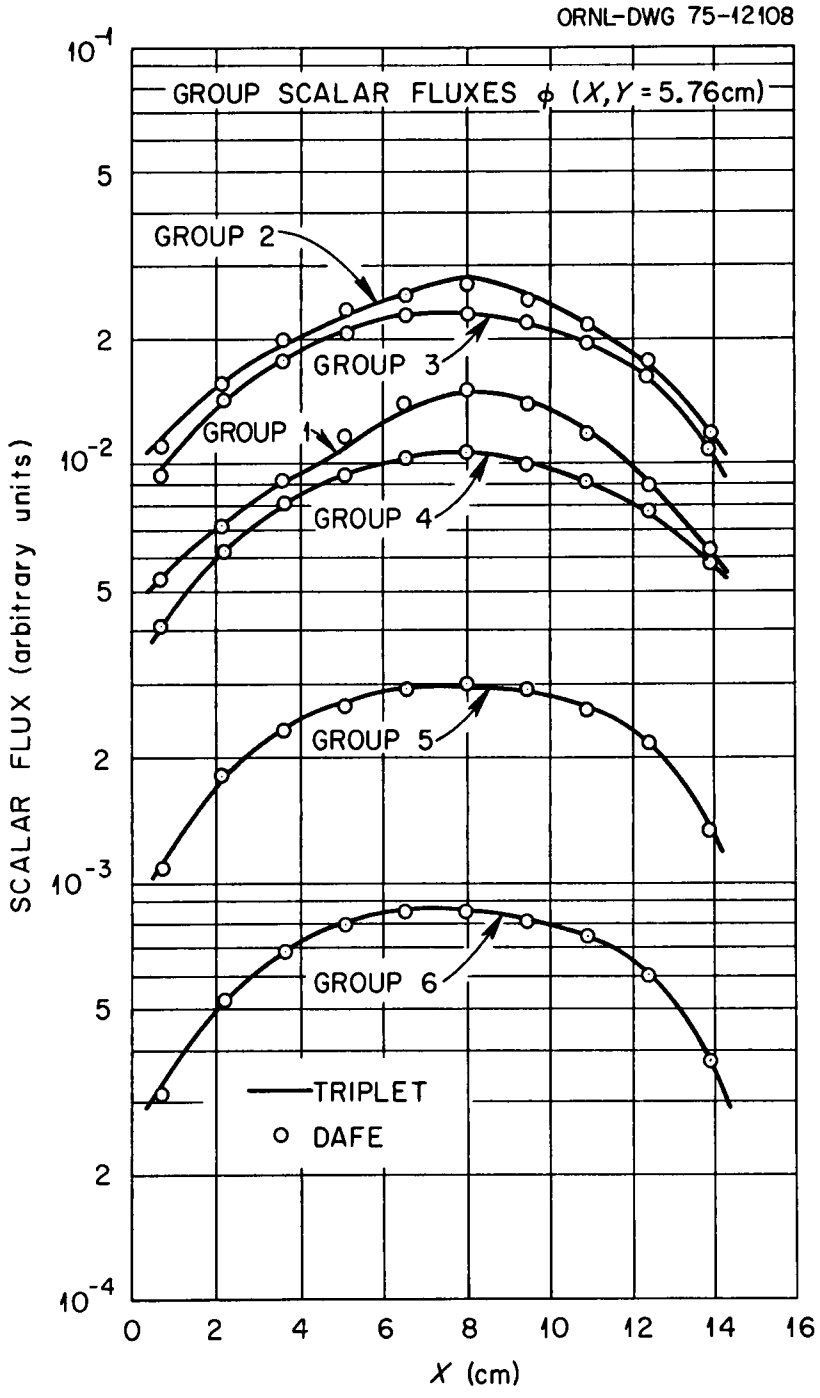


Figure 17. Comparison of group scalar fluxes near center (Y=5.76 cm) of eight zone two-dimensional model using TRIPLET and DAFE with the 200 regular triangle arrangement.

TRIPLET and DAFE. In addition, the 200 regular triangle arrangement was used in both codes. Although these fluxes represent a single traverse near the center of the model, their shapes are fairly representative of the overall two-dimensional flux behavior. As can be seen, the differences between the DAFE and TRIPLET values are relatively insignificant.

To determine the effect of reducing the leakage in the present model, a few of the calculations in Table V were repeated. The reduction in leakage was accomplished by imposing spectral reflection on the left and lower boundaries of the eight zone model. The resulting model thus represents quarter core symmetry. The results of these calculations are given in Table VI. Comparison with the equivalent cases in Table V reveals that all three codes yield smaller differences when compared with KENO. Although the increased agreement between DAFE and KENO is not quite as great as that obtained from DOT and TRIPLET, these results are indicative of DAFE's ability to obtain approximate solutions to realistic reactor problems since a reduction in leakage produces a more representative reactor model.

In addition to the preceding calculations, other calculations were performed using a third type of triangle arrangement. These calculations were performed to demonstrate the differences which may result when equivalent but reoriented triangulations are used to discretize the same spatial mesh. The differences occur because different triangulations can cause significant changes in the coupling between unknowns. Such changes can cause substantial differences in very heterogeneous problems like the present eight zone model.

TABLE VI

COMPARISON OF TWO-DIMENSIONAL EIGENVALUES ASSUMING QUARTER CORE SYMMETRY

Angular Quadrature[a]	No. of Triangles[b]	DOT		TRIPLET		DAFE	
		K	% DIF[c]	K	% DIF[c]	K	% DIF[c]
S_2	50	0.3305	-8.25	0.3317	-7.91	0.3221	-10.57
S_2	200	0.3337	-7.36	0.3342	-7.22	0.3305	-8.25
S_4	50	0.3519	-2.23	0.3532	-1.95	0.3428	-4.83
S_4	200	0.3558	-1.23	0.3565	-1.04	0.3536	-2.12

[a] S_2 and S_4 denote use of 6 and 16 angles in DOT calculations; 4 and 12 in TRIPLET; 2 and 6 in DAFE.

[b] Number of rectangles in DOT calculations was one-half the number of triangles given.

[c] Percent difference based on KENO K = 0.3602 ± 0.0020.

The changes in coupling due to different triangulations are illustrated in Figure 18. Both triangulations are equivalent with regard to the number and size of triangles. The two cases shown represent an extreme example, but they do demonstrate the significant changes which may occur. In the first case, unknown "5" is coupled only to the even numbered unknowns whereas it is coupled to all unknowns in the second case. In addition to the changed coupling, the number of triangles which directly influence unknown "5" is doubled.

The third type of triangulation is shown in Figure 19. This arrangement was obtained by reversing the orientation of the triangles in the regular triangle arrangement and thus has been designated the reversed triangle arrangement. A comparison of the eigenvalues obtained from DAFE using the different types of triangulation is presented in Table VII. As expected, differences in the eigenvalues do appear.

In order to be certain that these differences were not caused by numerical precision problems, these same calculations were repeated using a 90° rotated model. Although such a rotation reorders the unknowns, it does not produce any coupling changes. In all instances, the reordered calculations duplicated the differences exactly. Thus, these differences could not be attributed to numerical precision problems.

In spite of this verification, the differences due to the reoriented triangulations decrease as the spatial mesh is refined for all three quadratures. Thus, an increase in the number of triangles

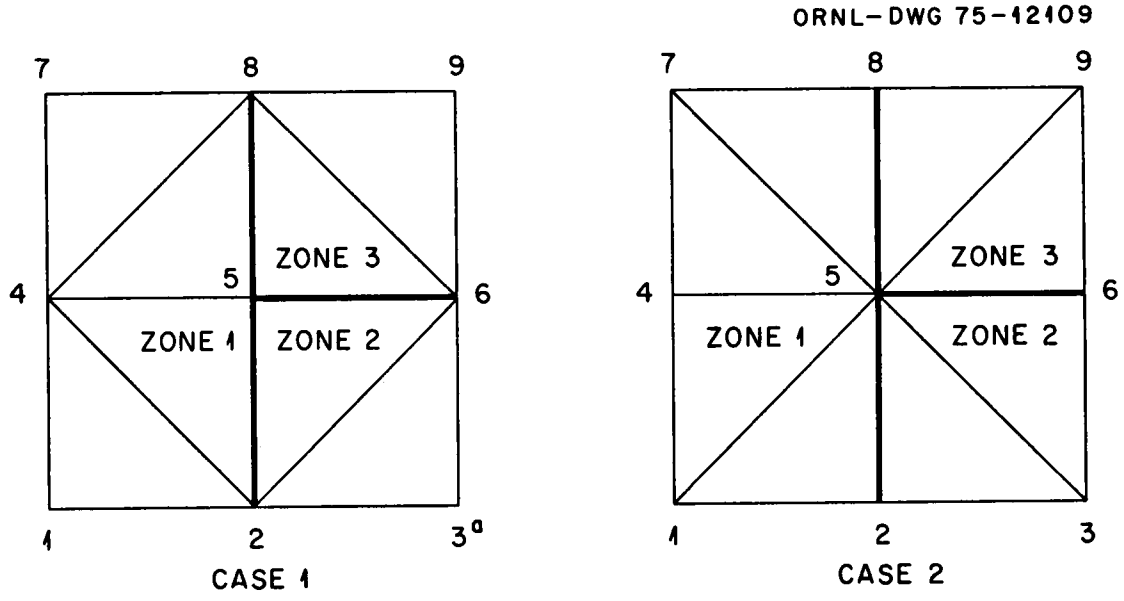


Figure 18. Illustration of changes in unknown coupling due to different triangle orientations.

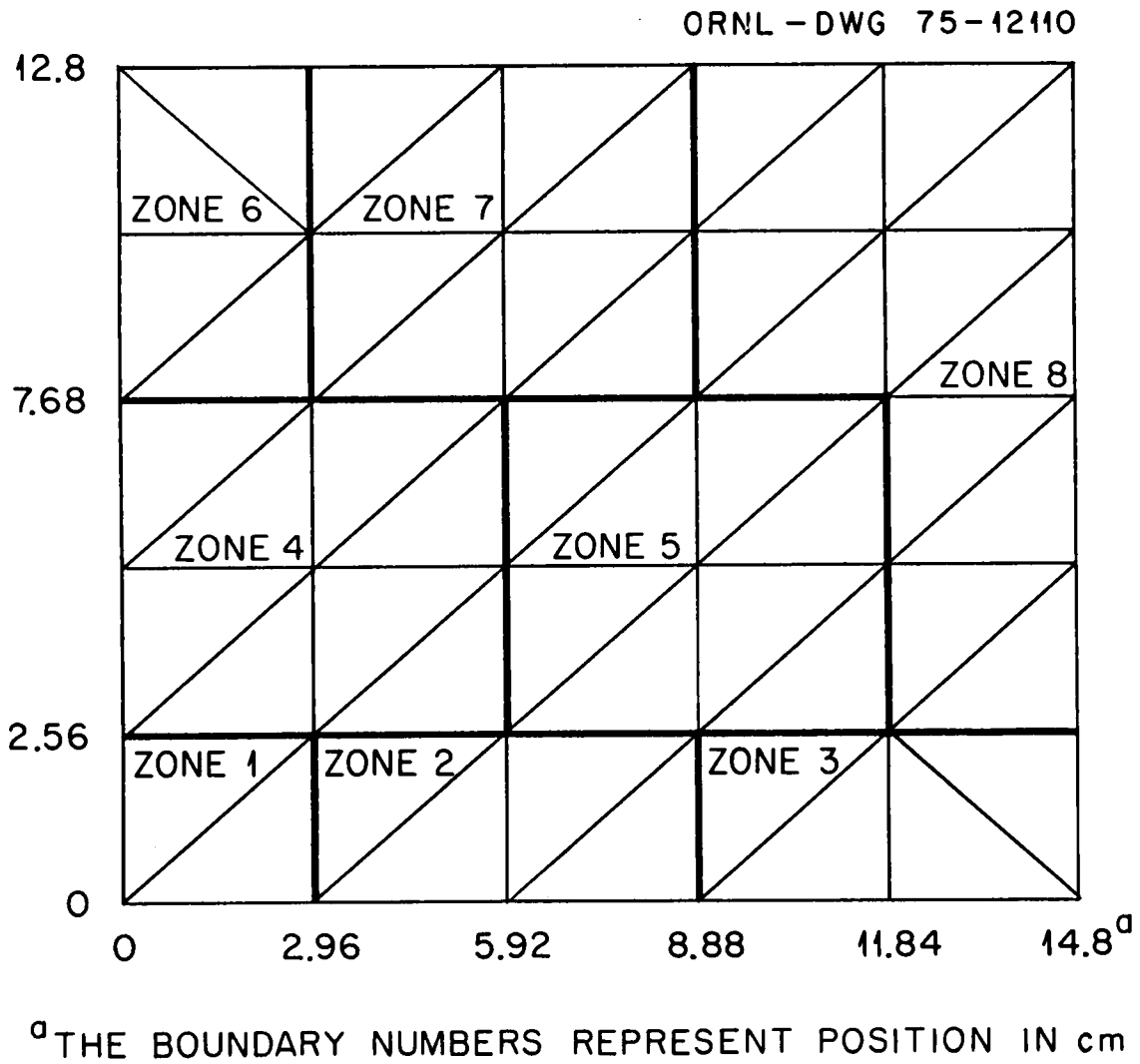


Figure 19. Typical reversed triangle arrangement (50 triangles) for two-dimensional eigenvalue comparison.

TABLE VII

COMPARISON OF TWO-DIMENSIONAL EIGENVALUES USING DIFFERENT TRIANGLE ARRANGEMENTS

E_N	No. of Triangles	K Regular Triangles	Reversed Triangles	% DIF[a]
E_2	30	0.1440	0.1395	-3.13
E_2	50	0.1540	0.1497	-2.81
E_2	200	0.1590	0.1559	-1.95
E_4	30	0.1560	0.1516	-2.82
E_4	50	0.1662	0.1635	-1.62
E_4	200	0.1734	0.1722	-0.69
E_6	30	0.1549	0.1517	-2.07
E_6	50	0.1664	0.1638	-1.81

[a]Percent difference based on values obtained from regular triangle arrangements.

negates the effects of reoriented triangulations. In general, the agreement is also improved when the order of the angular quadrature is increased. Although differences do exist, they do not appear to be significant in the present calculations.

The insignificance attached to the reoriented triangulation results is substantiated by the comparison of the group scalar fluxes which is presented in Figure 20. These fluxes were again obtained from a single traverse near the center of the model using the E_4-200 triangle results. The only noticeable difference appears in the first group comparison. Thus, the overall agreement can be considered excellent.

Representative reactor model. Unlike the small high leakage reactor model just analyzed, most realistic reactors are large low leakage configurations. In these configurations, the fissionable or core regions are near the center of the reactor and are usually surrounded by reflector material. Since most fission neutrons are born many mean free paths from external boundaries, they must undergo a considerably large number of scattering collisions if they are to leak from the reactor. Thus, the order of scattering anistropy usually plays a large role in determining criticality.

The third and final problem analyzed was chosen to illustrate the significance of incorporating anisotropic scattering into the discrete angle-finite element formulation. The model for this problem is shown in Figure 21. It is a quarter core model of a modified two-dimensional X-Y geometry ZPPR-4 mockup.[38] The modifications consisted of reducing the overall dimensions of the original model approximately 20%. In

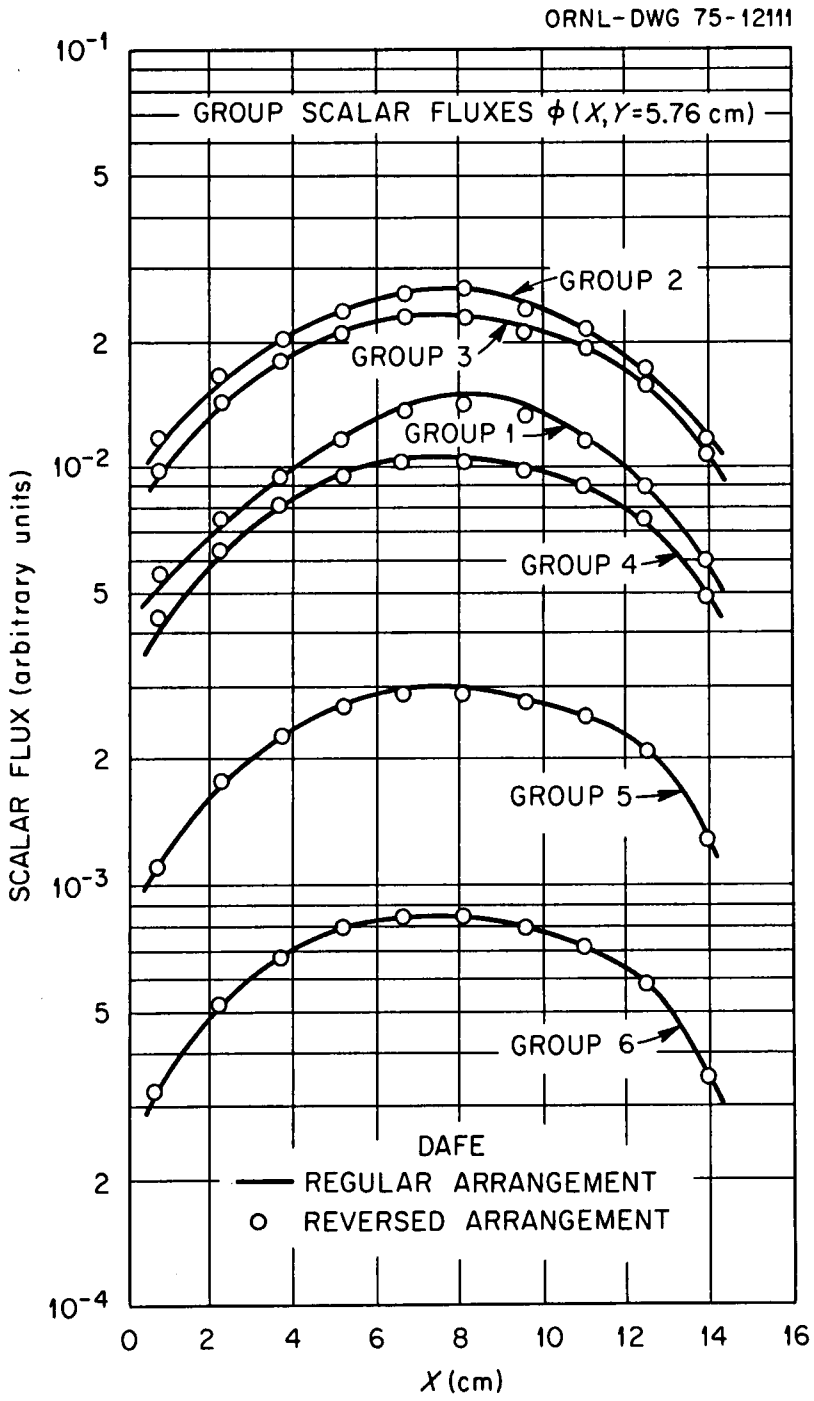
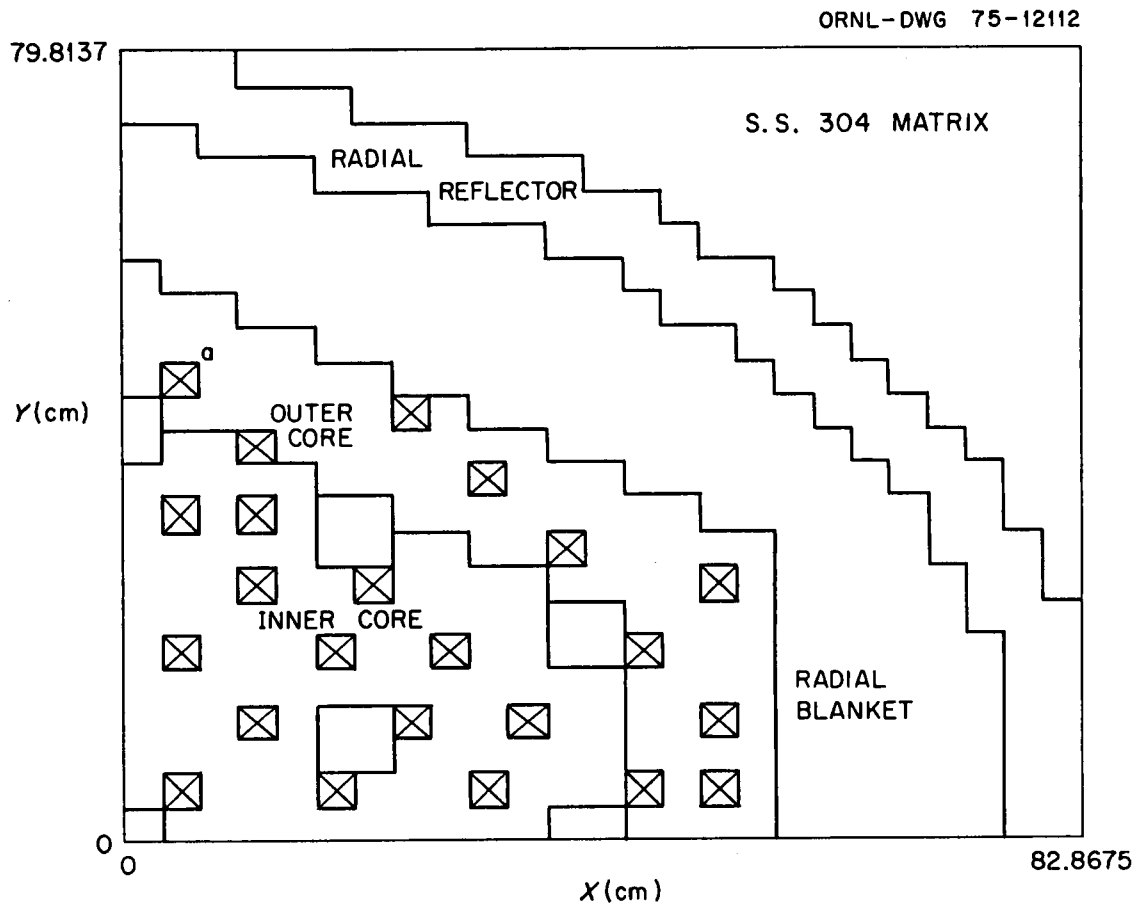


Figure 20. Comparison of group scalar fluxes near center (Y=5.76 cm) of eight zone two-dimensional model generated using DAFE with both the 200 regular and reversed triangle arrangements.



[a] THE CROSS-HATCHED BOXES ARE CONTROL MATERIAL. THE OTHER BOXES ARE SODIUM.

Figure 21. Quarter core model of modified two-dimensional X-Y geometry mockup of ZPPR-9.

addition, control material was moved from the few large sodium channels to the many small cross hatched boxes as indicated in Figure 21. Quarter core symmetry was obtained by imposing spectral reflection on the left and lower boundaries. The upper and right boundaries are vacuum boundaries.

The modified ZPPR-4 model was analyzed using DOT and DAFE. The DOT calculations were performed using 575 equally sized rectangles. This 23 × 25 rectangular mesh yielded a constant ΔX of 3.3147 cm. and a constant ΔY of 3.47016 cm. The DAFE calculations were performed using both regular and reversed triangle arrangements. These triangulations were obtained by bisecting the 575 rectangles, as described earlier, thus producing 1150 equally sized triangles. Convergence criteria of 10^{-3} on the pointwise scalar fluxes and 10^{-4} on the eigenvalues were again used in all calculations.

A six group P_1 scattering cross section set was used for the present analysis. This set was obtained by eliminating the last group of a seven group set which had been obtained by collapsing an existing 50 group set.[39] The last group was eliminated because initial calculations revealed that both DOT and DAFE calculated negative fluxes for the seventh group. In addition, it was noted that the seventh group fluxes were at least five orders of magnitude smaller than the next largest group fluxes. Since the seventh group thus contributed essentially nothing to the total fission source, it was removed from the cross section set.

In Table VIII, the eigenvalues obtained from these calculations are presented. Because of computer storage limitations, there were no DAFE E_4 calculations performed. Two types of comparison are presented in Table VIII. In the first type, all the eigenvalues are compared to the DOT S_4P_1 value. This comparison was included to illustrate the importance of anisotropic scattering. As expected, both of the DOT S_2P_1 and DAFE E_2P_1 calculations produced significantly better agreement than the DOT S_4P_0 calculation. Thus, the effect of using linearly anisotropic scattering was greater than the effect of using a higher order quadrature. However, if the P_0 calculations had been performed with transport corrected cross sections, the effect would not have been as great.

The second comparison is between equivalent DOT and DAFE calculations. For the four cases shown, the differences are all less than 0.5%. Also, since the DOT S_2P_1 calculations yield eigenvalues less than the DOT S_4P_1 eigenvalues, the agreement between the DAFE E_2P_1 eigenvalues and the DOT S_4P_1 values is better than the agreement between the equivalent DOT and DAFE calculations. Based on these results, it is apparent that the discrete angle-finite element formulation is capable of generating acceptable approximate solutions to large reactor problems.

In Figures 22 through 25, a number of two-dimensional reaction rates are plotted.[40] Both U-235 and U-238 reaction rates are presented to indicate the relative magnitudes of the low and high energy fluxes, respectively. These reaction rates, which are presented for both the

TABLE VIII

COMPARISON OF EIGENVALUES FOR TWO-DIMENSIONAL MODIFIED ZPPR-4 MODEL

	DOT			DAFE		
S_NP_L	K	% DIF[a]	E_NP_L	K	% DIF[a]	% DIF[b]
S_2P_0[c]	1.0589	2.75	E_2P_0	1.0630	3.14	0.39
S_2P_1	1.0298	-0.08	E_2P_1	1.0340	0.33	0.41
S_4P_0	1.0598	2.83	---	---	---	---
S_4P_1	1.0306	0.00	---	---	---	---
S_2P_0	0.9104[c]	2.55	E_2P_0	0.9125	2.78	0.23
S_2P_1	0.8875	-0.03	E_2P_1	0.8898	0.23	0.26
S_4P_0	0.9103	2.53	---	---	---	---
S_4P_1	0.8878	0.00	---	---	---	---

[a]Percent difference based on DOT S_4P_1 eigenvalue.

[b]Percent difference based on equivalent DOT calculations.

[c]First set of eigenvalues obtained with control rods out; second set with control rods in.

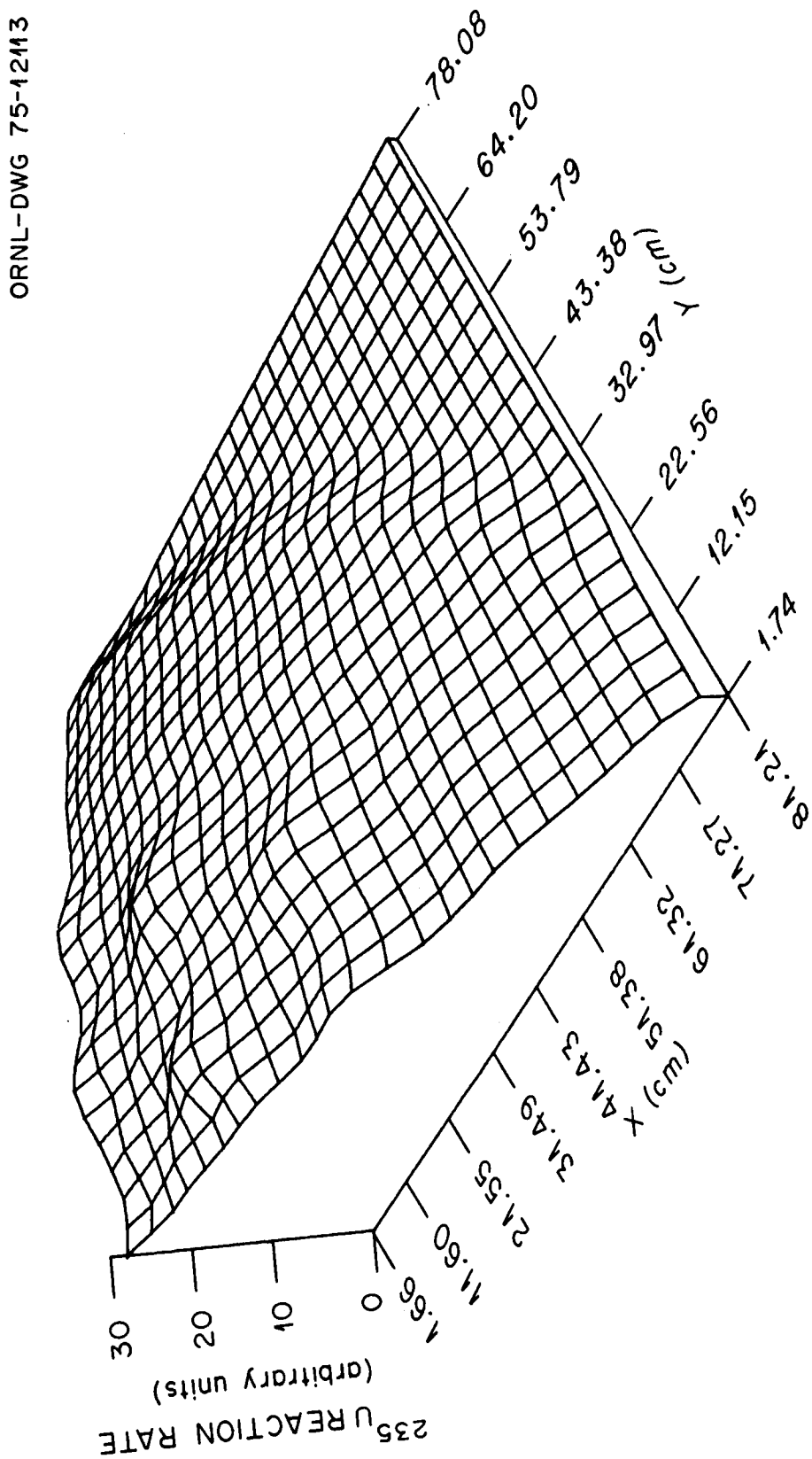


Figure 22. Three-dimensional plot of U-235 reaction rate obtained from DOT S_4P_1 calculation with control rods in.

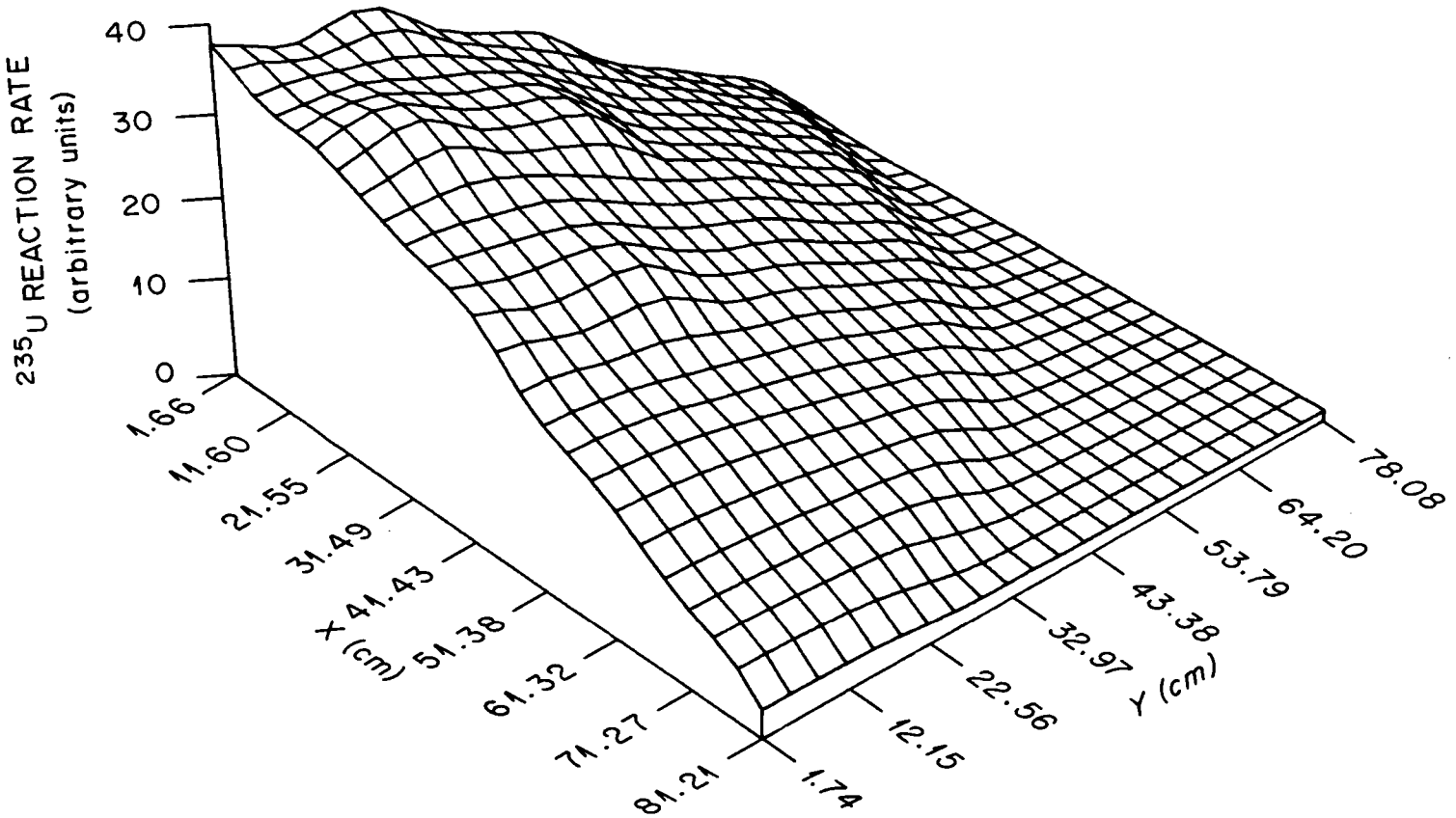


Figure 23. Three-dimensional plot of U-235 reaction rate obtained from DAFE E_2P_1 (reversed triangles) calculation with control rods out.

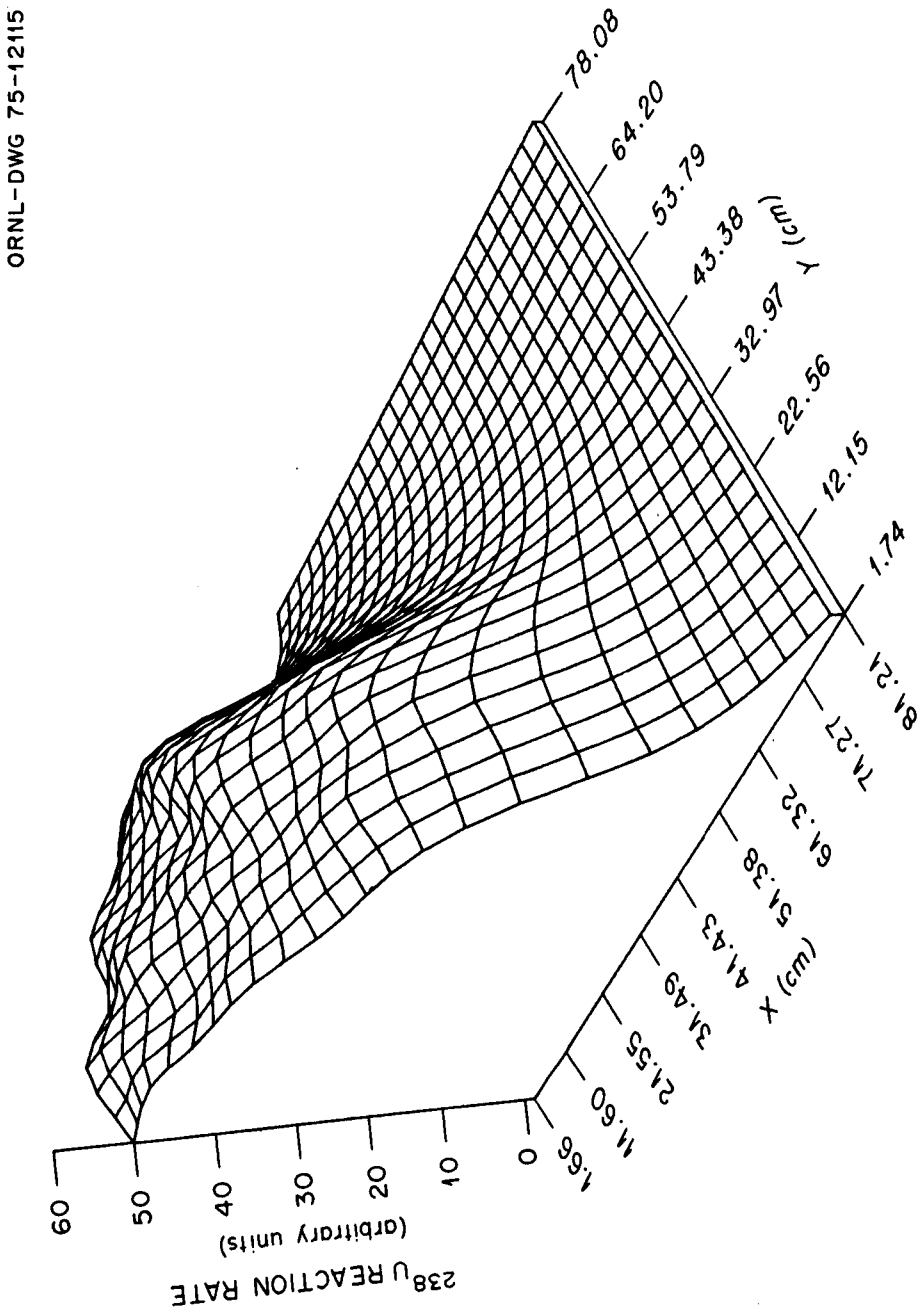


Figure 24. Three-dimensional plot of U-238 reaction rate obtained from DAFE E_2P_1 (regular triangles) calculation with control rods in.

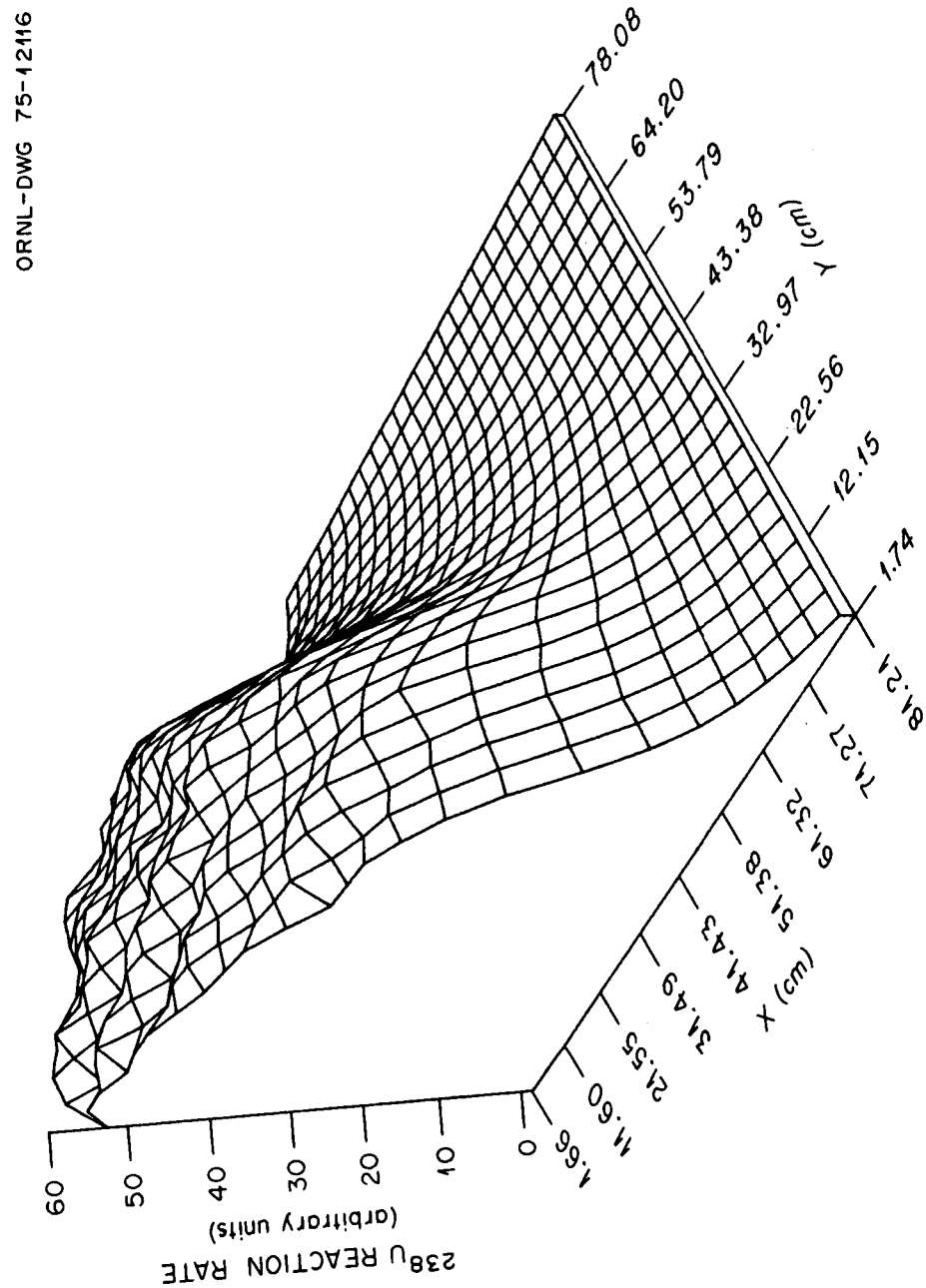


Figure 25. Three-dimensional plot of U-238 reaction rate obtained from DOT S_2P_1 calculation with control rods out.

control rods in and control rods out cases, were obtained using the group scalar fluxes generated in the present calculations. In addition, as noted in the figures, each of the plots utilized the fluxes from a different calculation.

A number of two-dimensional reaction rate comparisons between DOT and DAFE have also been performed. Three of these have been plotted and are presented in Figures 26 through 28. The percent differences in these figures are based on the second calculation in each case, i.e., if the comparison is between DAFE and DOT, the percent difference is based on the DOT calculation. Although the scales on these plots represent absolute percent difference, they were included for qualitative rather than quantitative considerations.

In Figures 26 and 27, the reaction rates obtained from the DAFE E_2P_1 calculations using both the regular and reversed triangle arrangements, respectively, are compared with the reaction rates from the DOT S_2P_1 calculations. The percent differences for both cases are fairly random and small except in the outer steel matrix region where they are approximately ±10%. However, in the outer region, the magnitudes of the fluxes are negligible compared to the magnitudes of the inner region fluxes. Thus, even small relative differences appear as large percent differences in the outer region. In Figure 28, the small ridge which appears in the outer steel matrix region immediately adjacent to the radial reflector is the only area in which any noticeable differences exist. Although these differences are approximately ±10%, the overall arrangement between the DAFE E_2P_1 calculation using the regular triangle arrangement and the DOT S_4P_1 calculation can be considered excellent.

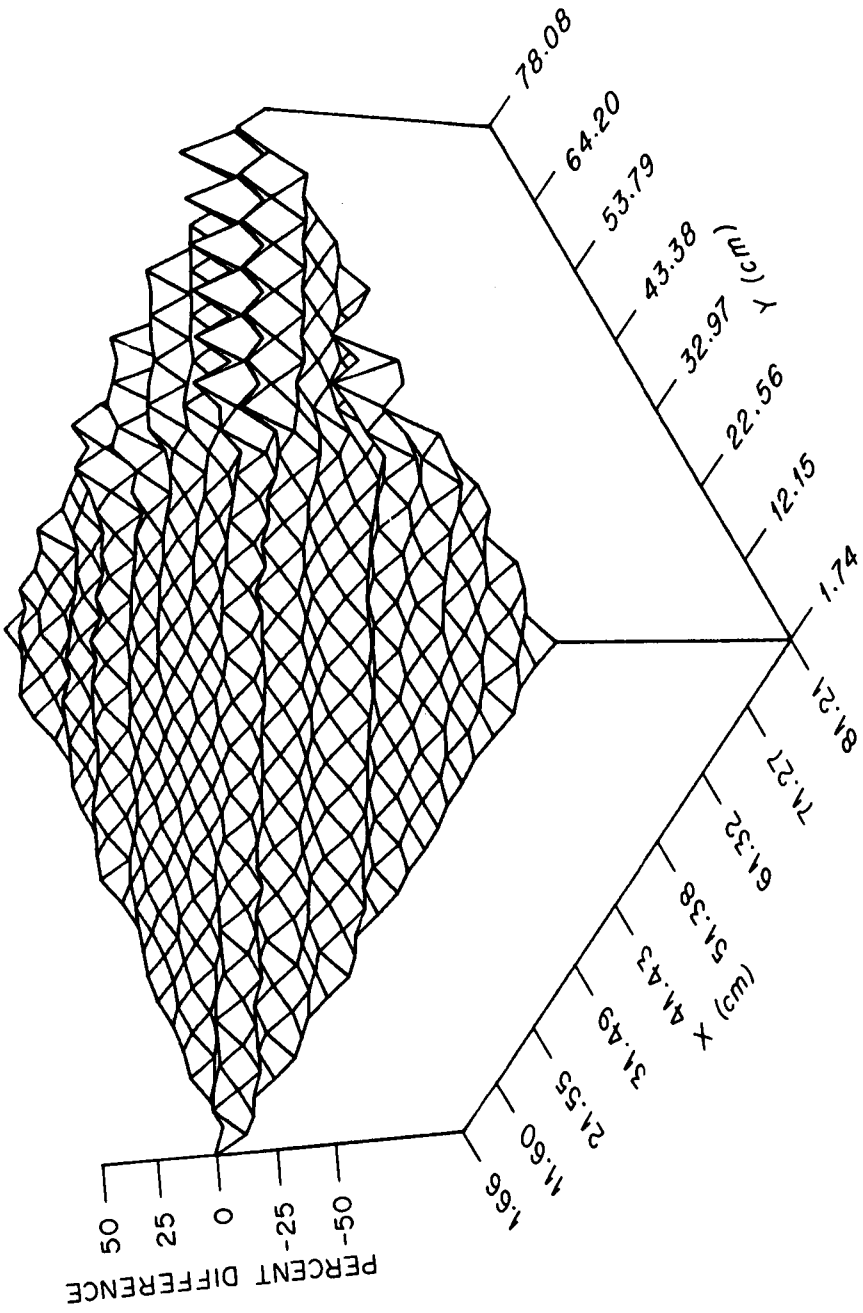


Figure 26. Three-dimensional plot of U-238 reaction rate differences between DAFE E_2P_1 (regular triangles) and DOT S_2P_1 calculations with control rods in.

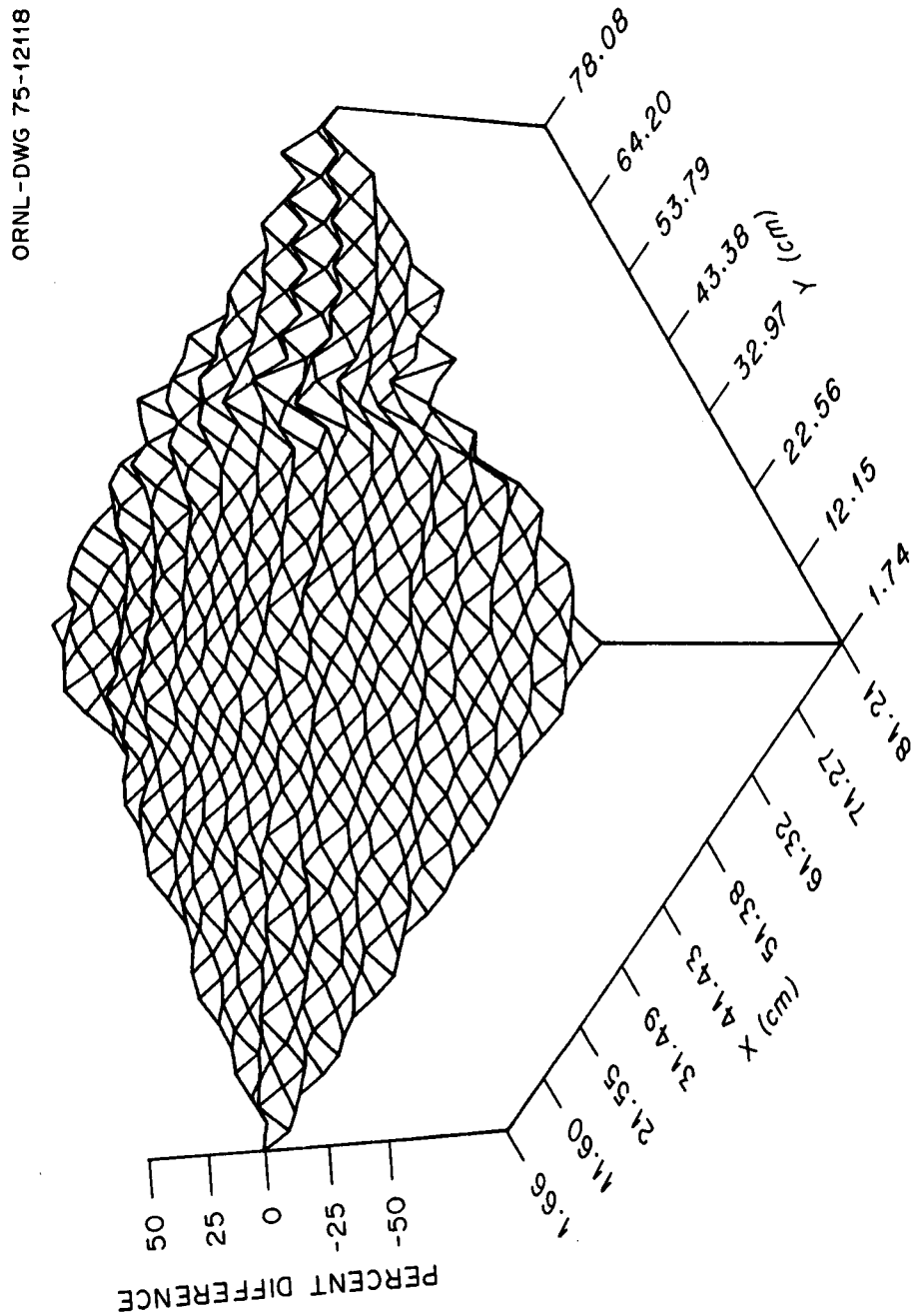


Figure 27. Three-dimensional plot of U-238 reaction rate differences between DAFE E_2P_1 (reversed triangles) and DOT S_2P_1 calculations with control rods in.

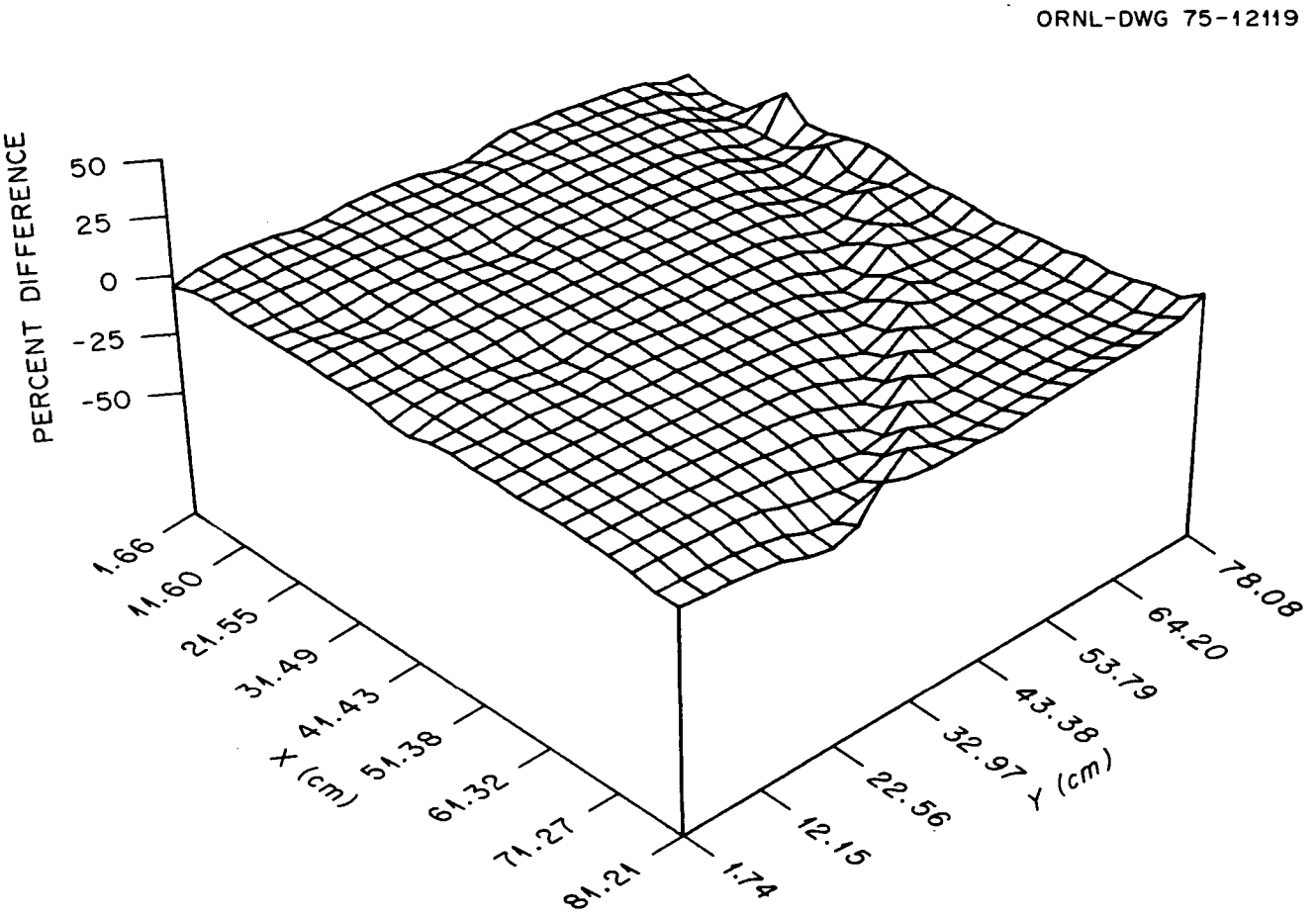


Figure 28. Three-dimensional plot of U-235 reaction rate differences between DAFE E_2P_1 (regular triangles) and DOT S_4P_1 calculations with control rods out.

A comparison of the eigenvalues obtained from DAFE using the different triangle arrangements is given in Table IX. Unlike the similar comparison of the effects of triangle reorientations for the small high leakage model, the percent differences in Table IX are essentially zero for the realistic reactor configuration. Based on the earlier discussion of Figures 26 and 27, the two-dimensional comparison shown in Figure 29 substantiates this conclusion.

In presenting the above results, no mention has been made of computer calculational times. The primary reason for this omission is because the present version of DAFE is not production oriented. Thus, there was essentially no effort directed toward the inclusion of sophisticated programming techniques such as the use of machine language routines. However, before concluding this chapter, it appears worthwhile to note that the DAFE calculational times were comparable to the other deterministic codes, i.e., TRIPLET and DOT, for most of the calculations. The only noticeable exception appeared in the analysis of the representative reactor model. In this final analysis, the DAFE calculational times were approximately twice those of DOT, i.e., 5 minutes versus 2.5 minutes of IBM OS/360 Model 91 central processor time.

TABLE IX

COMPARISON OF MODIFIED ZPPR-4 MODEL EIGENVALUES
USING DIFFERENT TRIANGLE ARRANGEMENTS

$E_N P_L$	K Regular Triangles	Reversed Triangles	% DIF[a]
$E_2 P_0$	1.0630	1.0626	-0.04
$E_2 P_1$	1.0340	1.0338	-0.02
$E_2 P_0$	0.9125[b]	0.9114	-0.12
$E_2 P_1$	0.8898	0.8888	-0.11

[a]Percent difference based on values obtained using regular triangles.

[b]First set of eigenvalues obtained with control rods out; second set with control rods in.

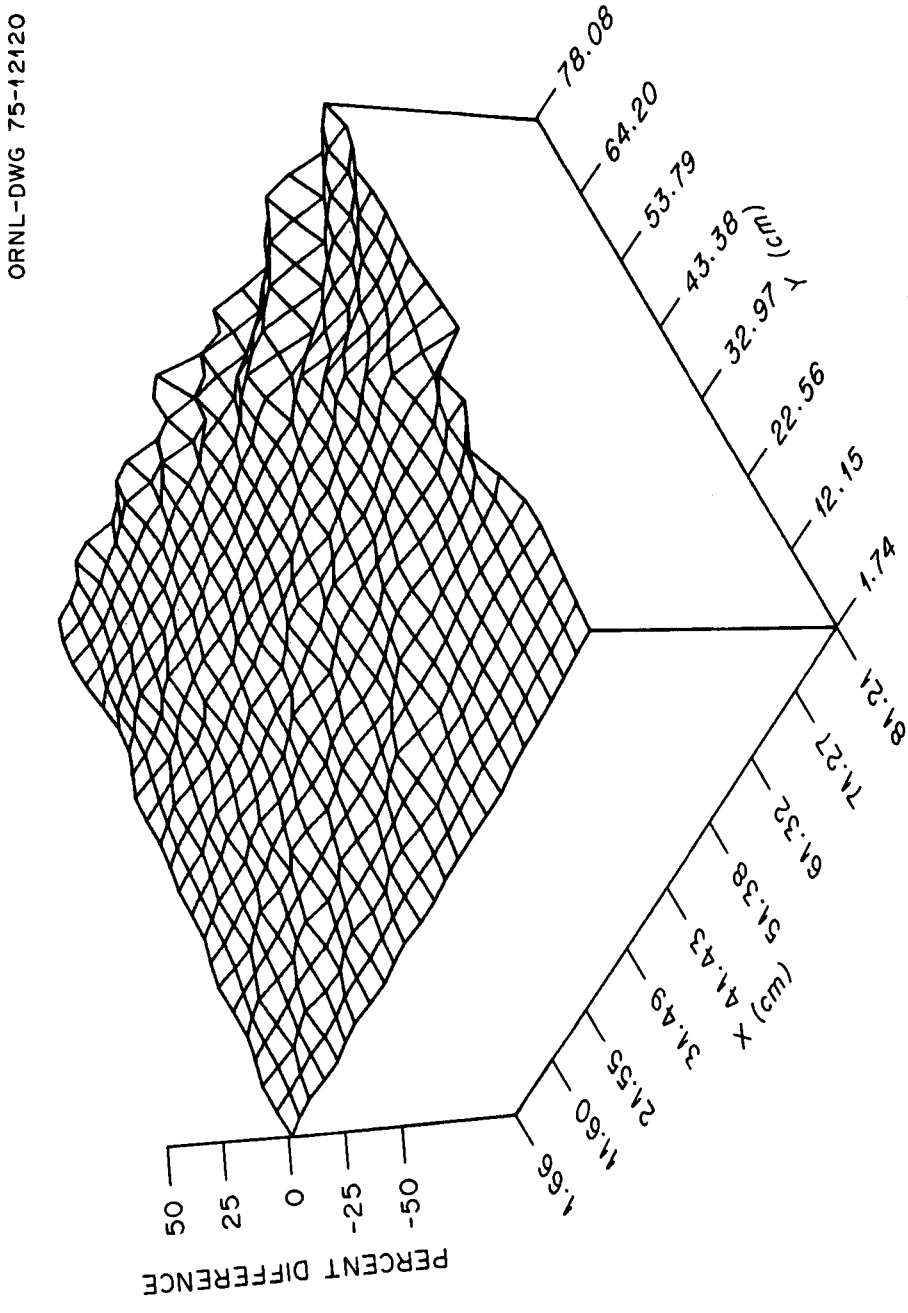


Figure 29. Three-dimensional plot of U-238 reaction rate differences between DAFE E_2P_1 (reversed triangles) and DAFE E_2P_1 (regular triangles) calculations with control rods in.

CHAPTER V

SUMMARY, CONCLUSIONS AND RECOMMENDATIONS

A finite element formulation has been developed and numerically implemented to obtain approximate solutions of the multigroup two-dimensional neutron transport equations. The accuracy, relative to other comparable solution methods, and limitations of the formulation were investigated by analyzing a series of test problems.

The formulation utilized variational functionals which were constructed from the second order forms of the monoenergetic even and odd parity flux equations. Energy coupling between functionals was obtained by employing standard multigroup source outer iteration techniques. A general treatment of anisotropic scattering was included in the development of the formulation through the use of discrete ordinates like approximations. In addition, the formulation was based on triangular spatial discretizations, which employed arbitrary shaped triangles, to allow its application to nonorthogonal planar geometry models.

Linear piecewise continuous Lagrange polynomials were used to approximate the spatial dependence of the even and odd parity discrete angle fluxes within each triangle. Coupled algebraic sets of equations were obtained by requiring the first variation of each group functional with respect to its spatial and angular discretized unknown values to be zero. The ordering of the unknown values was chosen such that the first variation of each functional produced a banded symmetric coupling

matrix. Essential spectral reflection boundary conditions were imposed on each group set of equations through the use of a symmetric modification procedure.

Numerical solutions were obtained by using a modified Cholesky algorithm to decompose each group coupling matrix. To keep computer storage requirements at a minimum, each decomposed matrix was written in compacted form over its corresponding coupling matrix. In addition, a substantial reduction in calculational time was obtained in multigroup problems, requiring many outer iterations, by storing and reusing the first iteration decomposed group coupling matrices.

The finite element formulation was used to analyze two problems which illustrate the appearance of ray effects in discrete ordinates calculations. In both problems, the ability of the finite element formulation to substantially reduce ray effects was demonstrated. Its ability to generate more realistic results than other methods employing low order angular treatments was confirmed by performing streaming calculations. The results of these calculations also demonstrated the ability of the formulation to make use of tailored quadrature sets.

The anisotropic scattering and multigroup treatments used in the development of the formulation were verified by performing a series of one-dimensional eigenvalue calculations. In addition, the relative accuracy of the formulation in predicting integral parameters while only directly considering half the angular phase space associated with discrete ordinates methods was illustrated.

The applicability of the formulation to nonorthogonal planar geometries was demonstrated by analyzing a simple model containing material arrangements similar to those found in hexagonal lattices. The effects of varying the spatial mesh and order of angular quadrature were investigated by comparing solutions obtained from the analysis of a small high leakage reactor model. This comparison revealed that the finite element formulation was more sensitive to the amount of spatial and angular refinement than other comparable calculational methods.

A final analysis was performed using the finite element formulation. This analysis consisted of a series of two-dimensional eigenvalue calculations for a large reactor model. The results of these calculations illustrated the importance of including a treatment of anisotropic scattering in the formulation. In addition, the sensitivity of the formulation to spatial and angular discretizations was shown to be insignificant when it was applied to realistic reactor configurations.

In performing the above calculations, two limitations of the present formulation were evident. The first limitation was the restriction of the formulation to small problems in terms of the number of unknowns. The use of multigroup outer iteration techniques essentially eliminated any restrictions on the number of energy groups. However, the direct inversion scheme did restrict the number of angular and spatial unknowns within each group.

It thus appears worthwhile to implement inner iteration techniques similar to those utilized in discrete ordinates codes. The implementation of self scatter source iterations would allow the use of a

substantially greater number of discrete angles in a given calculation. In addition, such an implementation should considerably reduce the complexity of the variational functionals.

The restriction on the number of spatial unknowns could be essentially eliminated by replacing the direct inversion algorithm with a matrix block inversion algorithm.[41] Schemes employing matrix block inversion techniques are already in existence and thus their implementation should be straightforward. However, due to the symmetric modification procedure which is used in the present formulation to impose spectral reflection boundary conditions, this implementation should not be considered trivial.

The second limitation concerns the application of boundary conditions to nonorthogonal boundaries. Vacuum boundary conditions can be imposed on nonorthogonal boundaries although care must be taken to ensure that none of the discrete angles lie along the boundary. However, symmetry or spectral reflection boundary conditions cannot be imposed on nonorthogonal boundaries in the present formulation. This characteristic of the formulation was caused by the use of discrete angles since spectral reflection requires the angular flux in one direction to be set equal to the angular flux in the reflected direction.

Since one of the objectives of this work was to develop a finite element formulation applicable to nonorthogonal planar geometries, future effort should be directed at removing this boundary condition limitation. One possible approach to accomplish this objective would be to interpolate between the angular directions as is done in discrete ordinates

calculations when nonsymmetric quadrature sets are used. A second approach would be to use an integral rather than discrete method of applying symmetry boundary conditions. Unfortunately, either approach would increase the size of the system matrices due to the increased coupling between angular directions.

Finally, there are a number of improvements and extensions which should be immediately implemented in the existing formulation. The easiest to implement would be the replacement of the existing decomposition routine with a more efficient routine to reduce calculational time. To ease input requirements, an automated mesh generator should be coupled to DAFE. Since mesh generators already exist,[41] this undertaking should be relatively simple. To extend the applicability of the formulation to thermal reactors, modifications should be made to allow upscattering. These modifications will probably require the use of sophisticated scaling techniques[33] to accelerate convergence. The formulation should be extended to R-Z cylindrical geometry. In implementing this final extension, it will probably prove equally advantageous to utilize rectangles as well as triangles to discretize the spatial domain.

LIST OF REFERENCES

LIST OF REFERENCES

1. Lathrop, K. D., "Discrete-Ordinates Methods for the Numerical Solution of the Transport Equation," Reactor Technology, 15: 107-133 (1972).

2. Mynatt, F. R., F. J. Muckenthaler and P. N. Stevens, "Development of Two-Dimensional Discrete Ordinates Transport Theory for Radiation Shielding," CTC-INF-952, Oak Ridge Computing Technology Center (August 1969).

3. Lathrop, K. D., "Elimination of Ray Effects by Converting Discrete Ordinate Equations to Spherical Harmonic-Like Equations," Proceedings of the Conference on New Developments in Reactor Mathematics and Applications, Idaho Falls, Idaho, March 29-31, 1971.

4. Lathrop, K. D., "Remedies for Ray Effects," Nuclear Science and Engineering, 45: 255 (September 1971).

5. Kang, C. M. and K. F. Hansen, "Finite Element Methods for Space-Time Reactor Analysis," MIT-NE-135, Massachusetts Institute of Technology, Cambridge, Massachusetts (November 1971).

6. Semenza, L. A., E. E. Lewis and E. C. Rossow, "The Application of the Finite Element Method to the Multigroup Neutron Diffusion Equation," Nuclear Science and Engineering, 47: 302-310 (March 1972).

7. Kaper, H. G., G. K. Leaf, and A. J. Lindeman, "A Timing Comparison Study for Some High Order Finite Element Approximation Procedures and a Low Order Finite Difference Approximation Procedure for the Numerical Solution of the Multigroup Neutron Diffusion Equation," Nuclear Science and Engineering, 49: 27-48 (September 1972).

8. Reed, W. H., "Triangular Mesh Difference Schemes for the Transport Equations," LA-4769, Los Alamos Scientific Laboratory (1971).

9. Miller, W. F., E. E. Lewis and E. C. Rossow, "The Application of Phase-Space Finite Elements to the Two-Dimensional Neutron Transport Equation in X-Y Geometry," Nuclear Science and Engineering, 52: 12-22 (September 1973).

10. Zienkiewicz, O. D., The Finite Element Method in Engineering Science, London, England: McGraw-Hill, 1971.

11. Ohnishi, T., "Finite Element Solution Techniques for Neutron Transport Equations," Proceedings of the Conference on Numerical Reactor Calculations, IAEA, Vienna (1972).

12. Miller, W. F., E. E. Lewis, and E. C. Rossow, "Two-Dimensional Transport Calculations Using Phase-Space Finite Elements," Transactions of the American Nuclear Society, 15: 780 (November 1972).

13. Aziz, A. K., Ed., The Mathematical Foundations of the Finite Element Method with Applications to Partial Differential Equations, New York, New York: Academic Press, 1972.

14. Deppe, L. O. and K. F. Hansen, "The Finite Element Method Applied to Neutron Diffusion Problems," MIT-NE-145, Massachusetts Institute of Technology, Cambridge, Massachusetts (February 1973).

15. Kaper, H. G., G. K. Leaf, and A. J. Lindemann, "Applications of Finite Element Methods in Reactor Mathematics. Numerical Solution of the Neutron Diffusion Equation," ANL-7925, Argonne National Laboratory (February 1972).

16. Ohnishi, T., "Application of Finite Element Solution Technique to Neutron Diffusion and Transport Equations," Proceedings of the Conference on New Developments in Reactor Mathematics and Applications, Idaho Falls, Idaho, March 29-31, 1971.

17. Kaplan, S. and J. S. Davis, "Canonical and Involutory Transformations of the Variational Problems of Transport Theory," Nuclear Science and Engineering, 28: 166-176 (May 1967).

18. Pitkaianta, J. and P. Silvennoinen, "Finite Element Analysis of Some Critical Fast Assemblies," Nuclear Science and Engineering, 52: 447-453 (December 1973).

19. Miller, W. F., E. E. Lewis, and E. C. Rossow, "The Application of Phase-Space Finite Elements to the One-Dimensional Neutron Transport Equation," Nuclear Science and Engineering, 51: 148-156 (June 1973).

20. Kaper, H. G., G. K. Leaf, and A. K. Lindeman, "Applications of Finite Element Methods in Reactor Mathematics: Numerical Solution of the Neutron Transport Equation," ANL-8126, Argonne National Laboratory (October 1974).

21. Reed, W. H., T. R. Hill, F. W. Brinkley, and K. D. Lathrop, "TRIPLET: A Two-Dimensional, Multigroup Triangular Mesh, Planar Geometry, Explicit Transport Code," LA-5428, Los Alamos Scientific Laboratory (October 1973).

22. Lathrop, K. D. and F. W. Brinkley, "Theory and Use of the General-Geometry TWOTRAN Program," LA-9432, Los Alamos Scientific Laboratory (1970).

23. Pomraning, G. C., "Reduction of Transport Theory to Multigroup Diffusion Theory," Journal of Nuclear Energy Parts A/B, 18: 497-512 (1964).

24. Kaplan, S., J. A. Davis, and M. Natelson, "Angle-Space Synthesis-An Approach to Transport Approximations," Nuclear Science and Engineering, 28: 364-375 (June 1967).

25. Bell, G. I. and S. Glasstone, Nuclear Reactor Theory, New York, New York: Van Nostrand Reinhold Company, 1970.

26. Arfken, G., Mathematical Methods for Physicists, New York, New York: Academic Press, Inc., 1966.

27. Sokolnikoff, I. S. and R. M. Redheffer, Mathematics of Physics and Modern Engineering, New York, New York: McGraw-Hill Book Company, Inc., 1958.

28. Smith, D. R., Variational Methods in Optimization, Englewood Cliffs, New Jersey: Prentice-Hall, Inc., 1974.

29. Akin, J. E. and D. L. Fenton, Finite Element Analysis Programming Concepts, unpublished, private communication.

30. Irving, J. and N. Mullineux, Mathematics in Physics and Engineering, New York, New York: Academic Press, Inc., 1959.

31. Bolstad, J. H., G. K. Leaf, A. J. Lindeman, and H. G. Kaper, "An Empirical Investigation of Reordering and Data Management for Finite Element Systems of Equations," ANL-8056, Argonne National Laboratory (September 1973).

32. Lillie, R. A., "Incorporation of Outer Iteration Techniques into the Task Algorithm," ORNL-TM-3958, Oak Ridge National Laboratory (November 1972).

33. Greenspan, H., C. N. Kelber, and D. Okrent (Eds.), Computing Methods in Reactor Physics, New York, New York: Gordon and Breach Science Publishers, 1968.

34. Rhoades, W. A. and F. R. Mynatt, "The DOT II Two-Dimensional Discrete Ordinates Transport Code," ORNL-TM-4280, Oak Ridge National Laboratory (September 1973).

35. Disney, R. K., R. G. Soltesy, J. Jedruch, and S. L. Zeigler, "Code Description and User's Manual for the MAP Radiation Transport Computer Code," WANL-TME-2706, Westinghouse Astronuclear Laboratory (August 1970).

36. Buhl, A. R., N. J. Ackermann, Jr., and J. C. Robinson, "Application of Transport Theory Kinetics to the Interpretation of Experimental Noise Spectra in Large Fast Breeders," Transactions of the American Nuclear Society, 12: 857-858 (June 1972).

37. Whitesides, G. E. and N. F. Cross, "KENO-A Multigroup Monte Carlo Criticality Program" CTC-5, Oak Ridge Computing Technology Center (September 1969).

38. Lesage, L. G. and P. I. Amundson, "Reactor Development Program Progress Report," ANL-RDP-34, Argonne National Laboratory (November 1974).

39. Selby, D. L. and G. F. Flanagan, "Subcriticality Calculations in Support of the Reactivity Surveillance Procedures Experiments for the FTR Engineering Mockup Facility," ORNL-5061, Oak Ridge National Laboratory (to be published).

40. Emerson, C. J., "PLOT 21-A Fortran Program which Produces Graphical Output Using ANISN or DOT Flux Data Sets," ORNL 74-12-3, Oak Ridge National Laboratory (December 1974).

41. Mondkar, D. P. and G. H. Powell, "Large Capacity Equation Solver for Structural Analysis," Computers and Structures, 4: 699-728 (1974).

APPENDICES

APPENDIX A

THE ADJOINT EVEN-ODD PARITY EQUATIONS

Throughout the text, reference is made to the symmetric and antisymmetric angular properties of the even and odd parity angular fluxes, respectively. In addition, reference is also made to the self-adjointness of the second order forms of the monoenergetic canonical even and odd parity angular flux equations. This statement does not imply equivalency between the forward and adjoint even and odd parity angular fluxes. It does, however, imply self-adjointness of the operators which appear in the second order equations.

The objective of this appendix is to illustrate the similarities between the forward and adjoint canonical equations. In addition, the significance of these similarities in the present discrete angle-finite element formulation is discussed. To accomplish these objectives, the adjoint form of Equation (2.5) is written[2]

$$- \vec{\Omega}\cdot\vec{\nabla}\,\phi^*(\vec{\Omega}) + \Sigma\,\phi^*(\vec{\Omega})$$

$$- \int_{\vec{\Omega}'} \Sigma_s(\vec{\Omega}'\cdot\vec{\Omega})\,\phi^*(\vec{\Omega}')\,d\vec{\Omega}' = S^*(\vec{\Omega}') \qquad (A.1)$$

with its associated adjoint vacuum boundary condition

$$\phi^*(\vec{\Omega})\Big|_{\vec{s}} = 0 \quad \text{for } \vec{\Omega}\cdot\vec{n} > 0. \qquad (A.2)$$

Since Equation (A.1) is equally valid for $-\vec{\Omega}$, it may be rewritten

$$\vec{\Omega}\cdot\vec{\nabla}\ \phi^*(-\vec{\Omega}) + \Sigma\ \phi^*(-\vec{\Omega})$$

$$- \int_{\vec{\Omega}'} \Sigma_s(\vec{\Omega}'\cdot-\vec{\Omega})\ \phi^*(\vec{\Omega}')\ d\vec{\Omega}' = S^*(-\vec{\Omega}). \tag{A.3}$$

Similarly, the adjoint vacuum boundary condition for $-\vec{\Omega}$ is

$$\phi^*(-\vec{\Omega})\Big|_{\vec{s}} = 0 \quad \text{for } \vec{\Omega}\cdot\vec{n} < 0. \tag{A.4}$$

The adjoint symmetry boundary conditions are identical to the forward conditions and thus will not be given. In Equations (A.1), (A.2), (A.3), and (A.4), $\phi^*(\vec{\Omega})$ and $S^*(\vec{\Omega})$ represent the adjoint flux and source, respectively. The remaining symbols have been previously defined in Chapter II, page 11.

The adjoint canonical equations are obtained by decomposing the adjoint angular flux and source into even and odd parity angular fluxes and sources, respectively. However, unlike the decomposition of the forward flux, i.e., Equation (2.7), the decomposition of the adjoint flux consists of a difference given by

$$\phi^*(\vec{\Omega}) = \psi^{e*}(\vec{\Omega}) - \psi^{o*}(\vec{\Omega}) \tag{A.5}$$

where the even parity adjoint angular flux is defined by

$$\psi^{e*}(\vec{\Omega}) = [\phi^*(\vec{\Omega}) + \phi^*(-\vec{\Omega})]/2 \tag{A.6}$$

and the odd parity adjoint angular flux is defined by

$$\psi^{o*}(\vec{\Omega}) = [\phi^*(-\vec{\Omega}) - \phi^*(\vec{\Omega})]/2. \tag{A.7}$$

The even and odd parity adjoint sources are defined by

$$S^{e*}(\vec{\Omega}) = [S^*(\vec{\Omega}) + S^*(-\vec{\Omega})]/2,$$

$$S^{o*}(\vec{\Omega}) = [S^*(-\vec{\Omega}) - S^*(\vec{\Omega})]/2. \tag{A.8}$$

Adding Equation (A.3) to (A.1) yields

$$\vec{\Omega}\cdot\vec{\nabla}\,\psi^{o*}(\vec{\Omega}) + \Sigma\,\psi^{e*}(\vec{\Omega})$$

$$- \int_{\vec{\Omega}'} \Sigma_s^e(\vec{\Omega}'\cdot\vec{\Omega})\,\psi^{e*}(\vec{\Omega}')\,d\vec{\Omega}' = S^{e*}(\vec{\Omega}) \tag{A.9}$$

and subtracting Equation (A.1) from (A.3) yields

$$\vec{\Omega}\cdot\vec{\nabla}\,\psi^{e*}(\vec{\Omega}) + \Sigma\,\psi^{o*}(\vec{\Omega})$$

$$- \int_{\vec{\Omega}'} \Sigma_s^o(\vec{\Omega}'\cdot\vec{\Omega})\,\psi^{o*}(\vec{\Omega}')\,d\vec{\Omega}' = S^{o*}(\vec{\Omega}). \tag{A.10}$$

In obtaining Equations (A.9) and (A.10), use was made of Equation (2.10), Equation (2.12), with $\psi^{e*}(\vec{\Omega})$ replacing $\psi^e(\vec{\Omega})$ and $\psi^{o*}(\vec{\Omega})$ replacing $\psi^o(\vec{\Omega})$, and Equations (A.5) through (A.8). The corresponding even and odd parity adjoint boundary conditions are obtained using Equations (A.2), (A.4), and (A.5) together with the symmetric and antisymmetric angular properties of the even and odd parity adjoint angular fluxes. These conditions are

$$\left[\psi^{e*}(\vec{\Omega}) - \psi^{o*}(\vec{\Omega})\right]\Big|_{\vec{s}} = 0 \quad \text{for } \vec{\Omega}\cdot\vec{n} > 0;$$

$$\left[\psi^{e*}(\vec{\Omega}) + \psi^{o*}(\vec{\Omega})\right]\Big|_{\vec{s}} = 0 \quad \text{for } \vec{\Omega}\cdot\vec{n} < 0. \tag{A.11}$$

A comparison of Equations (A.9) through (A.11) with Equations (2.13) through (2.15) reveals that the adjoint canonical equations may be obtained by directly substituting $\psi^{e*}(\vec{\Omega})$, $\psi^{o*}(\vec{\Omega})$, $S^{e*}(\vec{\Omega})$ and $S^{o*}(\vec{\Omega})$ for $\psi^{e}(\vec{\Omega})$, $\psi^{o}(\vec{\Omega})$, $S^{e}(\vec{\Omega})$ and $S^{o}(\vec{\Omega})$ in the forward equations. Thus the adjoint functionals, $F(\underline{\psi}^{e*})$ and $F(\underline{\psi}^{o*})$ may be obtained by simply making similar substitutions in Equations (2.61) and (2.63). Since the substitutions represent the only changes to the even and odd parity forward functionals, the forward and adjoint system matrices are equal.

The construction and decomposition of the system matrices represent a substantial portion of the calculation time for a given calculation. By saving the decomposed system matrices, a significant savings in calculational time can be obtained when both forward and adjoint calculations are performed using the discrete angle-finite element formulation.

APPENDIX B

VERIFICATION OF REDUCED FUNCTIONAL

In Chapter II, the reduced functional for $\underline{\psi}^e$ was obtained by simply introducing the definition of the first variation of $F(\underline{\psi}^e)$. Thus, the objective of this appendix is to verify that $F(\underline{\psi}^e)$, as given by Equation (2.61), is an acceptable functional for $\underline{\psi}^e$. To accomplish this objective, it will be shown that the first variation of $F(\underline{\psi}^e)$ with respect to $\underline{\psi}^e$ yields expression (2.59).

Applying the definition of the first variation of $F(\underline{\psi}^e)$ with respect to $\underline{\psi}^e$, i.e., Equation (2.60) to Equation (2.61) yields

$$\delta F(\underline{\psi}^e) = \lim_{\varepsilon \to o} \frac{\partial}{\partial \varepsilon} \{\frac{1}{2} \int_{\vec{r}} d\vec{r}\{[\underline{\underline{\vec{\Omega}}} \cdot \vec{\nabla}(\underline{\psi}^e + \varepsilon\delta\underline{\psi})]^T$$

$$\times \underline{\underline{w}}[\underline{\underline{\vec{\Omega}}} \cdot \vec{\nabla}(\underline{\psi}^e + \varepsilon\delta\underline{\psi}^e)]/\Sigma + (\underline{\psi}^e + \varepsilon\delta\underline{\psi}^e)^T \Sigma \underline{\underline{w}}(\underline{\psi}^e + \varepsilon\delta\underline{\psi}^e)$$

$$+ [\underline{\underline{\vec{\Omega}}} \cdot \vec{\nabla}(\underline{\psi}^e + \varepsilon\delta\underline{\psi}^e)]^T \underline{\underline{G}}^o [\underline{\underline{\vec{\Omega}}} \cdot \vec{\nabla}(\underline{\psi}^e + \varepsilon\delta\underline{\psi}^e)]/\Sigma$$

$$- (\underline{\psi}^e + \varepsilon\delta\underline{\psi}^e)^T \underline{\underline{H}}^e (\underline{\psi}^e + \varepsilon\delta\underline{\psi}^e) - 2[\underline{\underline{\vec{\Omega}}} \cdot \vec{\nabla}(\underline{\psi}^e + \varepsilon\delta\underline{\psi}^e)]^T \underline{\underline{G}}^o \underline{S}^o/\Sigma$$

$$- 2[\underline{\underline{\vec{\Omega}}} \cdot \vec{\nabla}(\underline{\psi}^e + \varepsilon\delta\underline{\psi}^e)]^T \underline{\underline{w}}\, \underline{S}^o/\Sigma - 2(\underline{\psi}^e + \varepsilon\delta\underline{\psi}^e)^T \underline{\underline{w}}\, \underline{S}^e$$

$$+ \frac{\Lambda}{2} \int_{\vec{s}} d\vec{s}[(\underline{\psi}^e + \varepsilon\delta\underline{\psi}^e)^T |\vec{n} \cdot \underline{\underline{\vec{\Omega}}}| \underline{\underline{w}}(\underline{\psi}^e + \varepsilon\delta\underline{\psi}^e)]\}. \qquad \text{(B.1)}$$

Expanding Equation (B.1) yields

$$\delta F(\underline{\psi}) = \lim_{\varepsilon \to o} \frac{\partial}{\partial \varepsilon} \{ \frac{1}{2} \int_{\vec{r}} d\vec{r} \{ [\underline{\underline{\vec{\Omega}}} \cdot \vec{\nabla} \, \underline{\psi}^e]^T \, \underline{\underline{w}} [\underline{\underline{\vec{\Omega}}} \cdot \vec{\nabla} \, \underline{\psi}^e] / \Sigma$$

$$\varepsilon [\underline{\underline{\vec{\Omega}}} \cdot \vec{\nabla} \, \underline{\psi}^e]^T \, \underline{\underline{w}} [\underline{\underline{\vec{\Omega}}} \cdot \vec{\nabla} \, \delta \underline{\psi}^e] / \Sigma + \varepsilon [\underline{\underline{\vec{\Omega}}} \cdot \vec{\nabla} \, \delta \underline{\psi}^e]^T \, \underline{\underline{w}} [\underline{\underline{\vec{\Omega}}} \cdot \vec{\nabla} \, \underline{\psi}^e] / \Sigma$$

$$+ \varepsilon^2 [\underline{\underline{\vec{\Omega}}} \cdot \vec{\nabla} \, \delta \underline{\psi}^e] \, \underline{\underline{w}} [\underline{\underline{\vec{\Omega}}} \cdot \vec{\nabla} \, \delta \underline{\psi}^e] / \Sigma + (\underline{\psi}^e)^T \, \Sigma \, \underline{\underline{w}} \, \underline{\psi}^e +$$

$$\varepsilon \, \delta (\underline{\psi}^e)^T \, \Sigma \, \underline{\underline{w}} \, \underline{\psi}^e + \varepsilon (\underline{\psi}^e)^T \, \Sigma \, \underline{\underline{w}} \, \delta \underline{\psi}^e + \varepsilon^2 \delta (\underline{\psi}^e)^T \, \Sigma \, \underline{\underline{w}} \, \delta \underline{\psi}^e +$$

$$[\underline{\underline{\vec{\Omega}}} \cdot \vec{\nabla} \, \underline{\psi}^e]^T \, \underline{\underline{G}}^o [\underline{\underline{\vec{\Omega}}} \cdot \vec{\nabla} \, \underline{\psi}^e] / \Sigma + \varepsilon [\underline{\underline{\vec{\Omega}}} \cdot \vec{\nabla} \, \underline{\psi}^e]^T \, \underline{\underline{G}}^o [\underline{\underline{\vec{\Omega}}} \cdot \vec{\nabla} \, \delta \underline{\psi}^e] / \Sigma +$$

$$\varepsilon [\underline{\underline{\vec{\Omega}}} \cdot \vec{\nabla} \, \delta \underline{\psi}^e]^T \, \underline{\underline{G}}^o [\underline{\underline{\vec{\Omega}}} \cdot \vec{\nabla} \, \underline{\psi}^e] / \Sigma + \varepsilon^2 [\underline{\underline{\vec{\Omega}}} \cdot \vec{\nabla} \, \delta \underline{\psi}^e]^T \, \underline{\underline{G}}^o [\underline{\underline{\vec{\Omega}}} \cdot \vec{\nabla} \, \delta \underline{\psi}^e] / \Sigma$$

$$- (\underline{\psi}^e)^T \, \underline{\underline{H}}^e \underline{\psi}^e - \varepsilon (\underline{\psi}^e)^T \, \underline{\underline{H}}^e \, \delta \underline{\psi}^e - \varepsilon \delta (\underline{\psi}^e)^T \, \underline{\underline{H}}^e \underline{\psi}^e - \varepsilon^2 \delta (\underline{\psi}^e)^T \, \underline{\underline{H}}^e \, \delta \underline{\psi}^e$$

$$- 2 [\underline{\underline{\vec{\Omega}}} \cdot \vec{\nabla} \, \underline{\psi}^e]^T \, \underline{\underline{G}}^o \, \underline{S}^o / \Sigma - 2\varepsilon [\underline{\underline{\Omega}} \cdot \nabla \, \delta \underline{\psi}^e]^T \, \underline{\underline{G}}^o \, \underline{S}^o / \Sigma$$

$$- 2 [\underline{\underline{\vec{\Omega}}} \cdot \vec{\nabla} \, \underline{\psi}^e]^T \, \underline{\underline{w}} \, \underline{S}^o / \Sigma - 2\varepsilon [\underline{\underline{\vec{\Omega}}} \cdot \vec{\nabla} \, \delta \underline{\psi}^e]^T \, \underline{\underline{w}} \, \underline{S}^o / \Sigma$$

$$- 2 (\underline{\psi}^e)^T \, \underline{\underline{w}} \, \underline{S}^e - 2\varepsilon \delta (\underline{\psi}^e)^T \, \underline{\underline{w}} \, \underline{S}^e \} +$$

$$\frac{\Lambda}{2} \int_{\vec{s}} d\vec{s} [(\underline{\psi}^e)^T |\vec{n} \cdot \underline{\underline{\vec{\Omega}}}| \underline{\underline{w}} \, \underline{\psi}^e + \varepsilon (\underline{\psi}^e)^T |\vec{n} \cdot \underline{\underline{\vec{\Omega}}}| \underline{\underline{w}} \, \delta \underline{\psi}^e +$$

$$\varepsilon \delta (\underline{\psi}^e)^T |\vec{n} \cdot \underline{\underline{\vec{\Omega}}}| \underline{\underline{w}} \, \underline{\psi}^e + \varepsilon^2 \delta (\underline{\psi}^e)^T |\vec{n} \cdot \underline{\underline{\vec{\Omega}}}| \underline{\underline{w}} \, \delta \underline{\psi}^e] \}. \qquad \text{(B.2)}$$

Upon taking the derivative with respect to ε, Equation (B.2) reduces to

$$\delta F(\underline{\psi}^e) = \lim_{\varepsilon \to o} \{\frac{1}{2} \int_{\vec{r}} d\vec{r}\{[\underline{\underline{\vec{\Omega}}}\cdot\vec{\nabla}\ \underline{\psi}^e]^T\ \underline{\underline{w}}[\underline{\underline{\vec{\Omega}}}\cdot\vec{\nabla}\ \delta\underline{\psi}^e]/\Sigma$$

$$[\underline{\underline{\vec{\Omega}}}\cdot\vec{\nabla}\ \delta\underline{\psi}^e]^T\ \underline{\underline{w}}[\underline{\underline{\vec{\Omega}}}\cdot\vec{\nabla}\ \underline{\psi}^e]/\Sigma + 2\varepsilon[\underline{\underline{\vec{\Omega}}}\cdot\vec{\nabla}\ \delta\underline{\psi}^e]^T\ \underline{\underline{w}}[\underline{\underline{\vec{\Omega}}}\cdot\vec{\nabla}\ \delta\underline{\psi}^e]/\Sigma$$

$$+ (\underline{\psi}^e)^T\ \Sigma\ \underline{\underline{w}}\ \delta\underline{\psi}^e + \delta(\underline{\psi}^e)^T\ \Sigma\ \underline{\underline{w}}\ \underline{\psi}^e + 2\varepsilon\delta(\underline{\psi}^e)^T\ \Sigma\ \underline{\underline{w}}\ \delta\underline{\psi}^e +$$

$$[\underline{\underline{\vec{\Omega}}}\cdot\vec{\nabla}\ \underline{\psi}^e]^T\ \underline{\underline{G}}^o[\underline{\underline{\vec{\Omega}}}\cdot\vec{\nabla}\ \delta\underline{\psi}^e]/\Sigma + [\underline{\underline{\vec{\Omega}}}\cdot\vec{\nabla}\ \delta\underline{\psi}^e]\ \underline{\underline{G}}^o[\underline{\underline{\vec{\Omega}}}\cdot\vec{\nabla}\ \underline{\psi}^e]/\Sigma +$$

$$2\varepsilon[\underline{\underline{\vec{\Omega}}}\cdot\vec{\nabla}\ \delta\underline{\psi}^e]^T\ \underline{\underline{G}}^o[\underline{\underline{\vec{\Omega}}}\cdot\vec{\nabla}\ \delta\underline{\psi}^e]/\Sigma - (\psi^e)^T\ \underline{\underline{H}}^e\ \delta\underline{\psi}^e -$$

$$\delta(\underline{\psi}^e)^T\ \underline{\underline{H}}^e\underline{\psi}^e - 2\varepsilon\delta(\underline{\psi}^e)^T\ \underline{\underline{H}}^e\delta\underline{\psi}^e - 2[\underline{\underline{\vec{\Omega}}}\cdot\vec{\nabla}\ \delta\underline{\psi}^e]^T\ \underline{\underline{G}}^o\ \underline{S}^o/\Sigma$$

$$- 2[\underline{\underline{\vec{\Omega}}}\cdot\vec{\nabla}\ \delta\underline{\psi}^e]^T\ \underline{\underline{w}}\ \underline{S}^o/\Sigma - 2\delta(\underline{\psi}^e)^T\ \underline{\underline{w}}\ \underline{S}^e\} +$$

$$\frac{\Lambda}{2} \int_{\vec{s}} d\vec{s}[(\underline{\psi}^e)^T|\vec{n}\cdot\underline{\underline{\vec{\Omega}}}|\underline{\underline{w}}\ \delta\underline{\psi}^e + \delta(\underline{\psi}^e)^T|\vec{n}\cdot\underline{\underline{\vec{\Omega}}}|\underline{\underline{w}}\ \underline{\psi}^e$$

$$+ 2\varepsilon\delta(\underline{\psi}^e)^T|\vec{n}\cdot\underline{\underline{\vec{\Omega}}}|\underline{\underline{w}}\ \delta\underline{\psi}^e]\}. \qquad \text{(B.3)}$$

Upon taking the limit as ε goes to zero, Equation (B.3) reduces to

$$\delta F(\psi^e) = \frac{1}{2} \int_{\vec{r}} d\vec{r}\{[\underline{\underline{\vec{\Omega}}}\cdot\vec{\nabla}\ \underline{\psi}^e]^T\ \underline{\underline{w}}[\underline{\underline{\vec{\Omega}}}\cdot\vec{\nabla}\ \delta\underline{\psi}^e]/\Sigma$$

$$[\underline{\underline{\vec{\Omega}}}\cdot\vec{\nabla}\ \delta\underline{\psi}^e]^T\ \underline{\underline{w}}[\underline{\underline{\vec{\Omega}}}\cdot\vec{\nabla}\ \underline{\psi}^e]/\Sigma + (\underline{\psi}^e)^T\ \Sigma\ \underline{\underline{w}}\ \delta\underline{\psi}^e +$$

$$\delta(\underline{\psi}^e)^T\ \Sigma\ \underline{\underline{w}}\ \psi^e + [\underline{\underline{\vec{\Omega}}}\cdot\vec{\nabla}\ \underline{\psi}^e]^T\ \underline{\underline{G}}^o[\underline{\underline{\vec{\Omega}}}\cdot\vec{\nabla}\ \delta\underline{\psi}^e]/\Sigma +$$

$$[\underline{\underline{\vec{\Omega}}}\cdot\vec{\nabla}\ \delta\underline{\psi}^e]^T\ \underline{\underline{G}}^o[\underline{\underline{\vec{\Omega}}}\cdot\vec{\nabla}\ \underline{\psi}^e]/\Sigma - (\underline{\psi}^e)^T\ \underline{\underline{H}}^e\ \delta\underline{\psi}^e -$$

$$\delta(\underline{\psi}^e)^T \underline{\underline{H}}^e \underline{\psi}^e - 2[\vec{\underline{\underline{\Omega}}}\cdot\vec{\nabla}\ \delta\underline{\psi}^e]^T \underline{\underline{G}}^o\ \underline{S}^o/\Sigma - 2[\vec{\underline{\underline{\Omega}}}\cdot\vec{\nabla}\ \delta\underline{\psi}^e]^T \underline{\underline{w}}\ \underline{S}^o/\Sigma$$

$$- \delta(\underline{\psi}^e)^T \underline{\underline{w}}\ \underline{S}^e\} + \frac{\Lambda}{2}\int_{\vec{S}} d\vec{s}[(\underline{\psi}^e)^T|\vec{n}\cdot\vec{\underline{\underline{\Omega}}}|\underline{\underline{w}}\ \delta\underline{\psi}^e$$

$$+ \delta(\underline{\psi}^e)^T|\vec{n}\cdot\vec{\underline{\underline{\Omega}}}|\underline{\underline{w}}\ \underline{\psi}^e]. \qquad (B.4)$$

Since all the terms in Equation (B.4) are scalars, their transposes are equal. Thus letting the matrix $\underline{\underline{A}}$ represent the symmetric matrices $\underline{\underline{w}}$, $\underline{\underline{G}}^o$, $\underline{\underline{H}}^e$ and $\vec{\underline{\underline{\Omega}}}$, terms of the form $\delta(\underline{X})^T\ \underline{\underline{A}}\ \underline{X}$ obey

$$\delta(\underline{X})^T\ \underline{\underline{A}}\ \underline{X} = \underline{X}^T\ \underline{\underline{A}}\ \delta\underline{X}. \qquad (B.5)$$

Using Equation (B.5) allows Equation (B.4) to be rewritten

$$\delta F(\underline{\psi}^e) = \int_{\vec{r}} d\vec{r}\{[\vec{\underline{\underline{\Omega}}}\cdot\vec{\nabla}\ \delta\underline{\psi}^e]^T\ \underline{\underline{w}}[\vec{\underline{\underline{\Omega}}}\cdot\vec{\nabla}\ \underline{\psi}^e]/\Sigma +$$

$$\delta(\underline{\psi}^e)^T\ \Sigma\ \underline{\underline{w}}\ \underline{\psi}^e + [\vec{\underline{\underline{\Omega}}}\cdot\vec{\nabla}\ \delta\underline{\psi}^e]^T\ \underline{\underline{G}}^o[\vec{\underline{\underline{\Omega}}}\cdot\vec{\nabla}\ \underline{\psi}^e]/\Sigma$$

$$- \delta(\underline{\psi}^e)^T\ \underline{\underline{H}}^e\underline{\psi}^e - [\vec{\underline{\underline{\Omega}}}\cdot\vec{\nabla}\ \delta\underline{\psi}^e]^T\ \underline{\underline{G}}^o\ \underline{S}^o/\Sigma$$

$$- [\vec{\underline{\underline{\Omega}}}\cdot\vec{\nabla}\ \delta\underline{\psi}^e]^T\ \underline{\underline{w}}\ \underline{S}^o/\Sigma - \delta(\underline{\psi}^e)^T\ \underline{\underline{w}}\ \underline{S}^e\}$$

$$+ \Lambda\int_{\vec{S}} d\vec{s}\ \delta(\underline{\psi}^e)^T|\vec{n}\cdot\vec{\underline{\underline{\Omega}}}|\underline{\underline{w}}\ \underline{\psi}^e. \qquad (B.6)$$

A comparison of the right hand size of Equation (B.6) and expression (2.59) reveals that they are identical. Thus, the functional $F(\underline{\psi}^e)$ as given by Equation (2.61) is an acceptable functional for $\underline{\psi}^e$.

VITA

Richard Andrew Lillie was born in Rochester, New York, on March 21, 1944. He attended elementary school in Rochester until June 1954, at which time he moved to Saint Petersburg, Florida, where he was graduated from Dixie Hollins High School in 1962. He entered The University of Tennessee in September 1962 and received the Bachelor of Science degree in Nuclear Engineering in June 1967. During his undergraduate years, he was employed by ARO, Inc. in Tullahoma, Tennessee. He was employed by Oak Ridge National Laboratory during the summer of 1967.

He entered graduate school at The University of Tennessee in September 1967 on an AEC Traineeship in Nuclear Engineering. Beginning in July 1969, he spent two years in the U. S. Army working in the Engineers Reactor Group at Fort Belvoir, Virginia. In September 1971, he returned to graduate school and received the Master of Science degree in December 1972. He continued graduate school under the same AEC Traineeship until August 1974, at which time he accepted a research position with the Neutron Physics Division of Oak Ridge National Laboratory. He received the Doctor of Philosophy degree in December 1975. He is a member of Tau Beta Pi and the American Nuclear Society.

He is married to the former Elizabeth Herr of Rockville Centre, New York.